INDIUM, TIN, AND GALLIUM DOPED CDSE QUANTUM DOTS

by

CHRISTOPHER J TUINENGA

B.A., Augustana College, 2004

AN ABSTRACT OF A DISSERTATION

submitted in partial fulfillment of the requirements for the degree

DOCTOR OF PHILOSOPHY

Department of Chemistry
College of Arts and Sciences

KANSAS STATE UNIVERSITY
Manhattan, Kansas

2011

Abstract

Doping quantum dots to increase conductivity is a crucial step towards being able to fabricate a new generation of electronic devices built on the "bottom-up" platform that are smaller and more efficient than currently available. Indium, tin, and gallium have been used to dope CdSe in both the bulk and thin film regimes and introduce n-type electron donation to the conduction band. CdSe quantum dots have been successfully doped with indium, tin, and gallium using the $Li_4[Cd_{10}Se_4(SPh_{16})]$ single source precursor combined with metal chloride compounds. Doping CdSe quantum dots is shown to effect particle growth dynamics in the "heterogeneous growth regime." Doping with indium, tin, and gallium introduce donor levels 280, 100, and 50 meV below the conduction band minimum, respectively. Thin films of indium and tin doped quantum dots show improved conductivity over films of undoped quantum dots. Transient Absorption spectroscopy indicates that indium doping introduces a new electron energy level in the conduction band that results in a 70 meV blue shift in the $1S_e$ absorption bleach position. Novel characterization methods such as *in-situ* fluorescence growth monitoring, single quantum dot EDS acquisition, static and time-resolved temperature dependant fluorescence spectroscopy were developed in the course of this work as well. These results show that doping CdSe quantum dots with indium, tin, and gallium has not only been successful but has introduced new electronic properties to the quantum dots that make them superior to traditional CdSe quantum dots.

INDIUM, TIN, AND GALLIUM DOPED CDSE QUANTUM DOTS

by

CHRISTOPHER J TUINENGA

B.A., Augustana College, 2004

A DISSERTATION

submitted in partial fulfillment of the requirements for the degree

DOCTOR OF PHILOSOPHY

Department of Chemistry
College of Arts and Sciences

KANSAS STATE UNIVERSITY
Manhattan, Kansas

2011

Approved by:

Major Professor
Viktor Chikan

Copyright

.

Abstract

Doping quantum dots to increase conductivity is a crucial step towards being able to fabricate a new generation of electronic devices built on the "bottom-up" platform that are smaller and more efficient than currently available. Indium, tin, and gallium have been used to dope CdSe in both the bulk and thin film regimes and introduce n-type electron donation to the conduction band. CdSe quantum dots have been successfully doped with indium, tin, and gallium using the $Li_4[Cd_{10}Se_4(SPh_{16})]$ single source precursor combined with metal chloride compounds. Doping CdSe quantum dots is shown to effect particle growth dynamics in the "heterogeneous growth regime." Doping with indium, tin, and gallium introduce donor levels 280, 100, and 50 meV below the conduction band minimum, respectively. Thin films of indium and tin doped quantum dots show improved conductivity over films of undoped quantum dots. Transient Absorption spectroscopy indicates that indium doping introduces a new electron energy level in the conduction band that results in a 70 meV blue shift in the $1S_e$ absorption bleach position. Novel characterization methods such as *in-situ* fluorescence growth monitoring, single quantum dot EDS acquisition, static and time-resolved temperature dependant fluorescence spectroscopy were developed in the course of this work as well. These results show that doping CdSe quantum dots with indium, tin, and gallium has not only been successful but has introduced new electronic properties to the quantum dots that make them superior to traditional CdSe quantum dots.

Table of Contents

List of Figures

List of Tables

Acknowledgements

I would first like to thank my major Professor Viktor Chikan; without his knowledge, guidance, and enthusiasm this project would not have been as successful or as much fun. I must also thank him for the encouragement to keep pushing forward when things got difficult. Last, I would like to express my gratitude to him for allowing me to spend the Fall of 2008 in Germany on an internship with Robert Bosch GmbH.

Next I would like to thank Jim Hodgson, Tobe Eders, Ron Jackson and Richard Bacham. Jim's expertise in creating the special optical windows for my glassware, as well as many of the other pieces needed to carry out this work, was invaluble. I owe Tobe a great deal of thanks for helping to build a dip-coater as well as for fixing the sonicators. Ron also deserves a great deal of thanks for his expertise on the dip-coater project as well as helping me design the low temperature conductivity apparatus. Although Richard retired during my time as a student, he was very helpful in the early days getting all of the gas flow systems set up.

My lab mates Dr. Naween Dahal, Dr. Pinar Dagtepe, Santanu Roy, Raj Dani, and Dr. Pankaj Mandal have my thanks as well. I would like to thank Pinar and Santanu specifically for their help with the time resolved spectroscopy and for finishing up the indium and tin doping project while I was away at Bosch.

I would like to thank several of our collaborators as well. Dr. Jacek Jasinski at the University of Louisville for his time and effort getting good TEM and EDS results for the indium and tin doping project. David Moore and Heather Shinoggle from the University of Kansas's MAI Lab for their experise in developing and obtaining the single particle EDS and 2 Dimensional EDS imageing.

Last I would like to thank Proffesor Klabunde of Kansas State University, Proffesors Dell Jensen and Richard Narske of Augustana College for finally convinceing me that law school could wait but graduate school couldn't.

Dedication

For my parents, James and Janet Tuinenga

Chapter 1 - Introduction

Over the course of human history the development of new materials have often led to advances in civilization, such as the transition from bronze to iron metallurgy. Iron in turn gave way to steel, which made possible the breathtaking skylines of our cities. The discovery of petroleum in the 19th century opened the door for a revolution in materials chemistry in the form of polymers, which are used in everything from clothing, food containers, furniture, and for chemists perhaps nothing is more important than our safety goggles.

However, if one class of materials must be lauded for revolutionizing the last 75 years of human history, it must be the semiconductor. Without early semiconductors such as silicon and germanium, we would not have the solid-state transistors that all of our electronic technology is based on. Prior to the development of the solid-state transistor, transistors constructed with vacuum tubes regulated current in circuits; which carried several drawbacks, the most notable being the size limitations of the vacuum tube. With semiconductors and their solid-state circuitry we are able to pattern millions of transistors on a semiconductor surface the size of our pinky fingernail.

Without these microscopic components our modern electronics are impossible. The notion of a computer small enough to be carried in a backpack is laughable without the solid-state components made possible by semiconductors. Flat-screen televisions are only possible by microscopic transistors and diodes. Cellular phones that fit in our pockets are out of the question. Compact disks cannot be read without a laser generated from a solid-state diode.

Current technology for fabricating semiconductor device components is not without limitations. Current methods that employ photoresist patterning and etching face a feature size limitation based on the following relationship[1]:

$$\text{Feature size (nm)} = 23 * \{\text{throughput } (\mu m^2/hr)\}^{1/5}$$

establishing a bottle neck in the resolution of microstructures based on fabrication speed. Indeed it is possible to create single nanometer sized structures given a slow enough throughput, but this will inevitably clash with the need to meet production demand. Therefore, an alternative to "top-down" fabrication methods currently in place is needed.

By using a "bottom-up" method of device construction, whereby individual components are created separately on the nanoscale and assembled into devices in a secondary step, it may be possible to overcome the throughput bottle-neck described above. Furthermore, by producing individual components on the nano-scale (nanomaterials) prior to assembly will allow more precise control of material properties. The term "nanomaterial" is broadly used to describe a collection of particles between 1 and 999 nm ($1x10^{-9}$ m). In this size regime many properties of the material begin to diverge from those of the "bulk" material. The four most common properties to change upon entering the nano-regime are:

- Surface area
- Melting point
- Magnetic moment
- Electronic properties

of these, the electronic properties of a material are the most crucial when discussing the transition to using nanoparticles, specifically nanomaterials known as quantum dots, to develop a new generation of electronic devices that are more powerful that those currently available.

Semiconductor Basics

The term "quantum dot" applies to any nanoparticle of a semiconductor material such as silicon (Si) or cadmium selenide (CdSe) that displays "quantum confined" or "quantized" behavior. Quantum confined or quantized behavior arises when the electron-hole pair, or exciton, of a semiconductor in the excited state is physically confined by the size of the particle.[2] In order to understand the advantages quantum dots posses over bulk semiconductors a brief overview of bulk semiconductor principles is followed by the effects of physical confinement of the electron-hole pair.

Bulk Semiconductors

The three most important properties of a pure semiconductor: the band gap, the intra-band energy states within the valence and conduction bands, and the carrier concentrations are fixed in the cases of the band gap and carrier concentration and continuous (separated by energies less than the thermal energy k_BT) for the intra-band energy states.

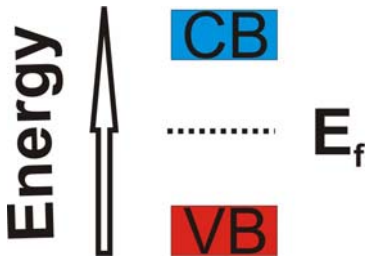

Figure 1-1 Simple Semiconductor Band Structure

The band structure of a semiconductor is shown in Figure 1-1 above. Semiconductors are distinguished from metals and insulators by their incomplete band structure, where the highest energy electron known as the Fermi Energy or Fermi Level (E_f in Figure 1.1) is located at an energy value above the highest quantum mechanically allowed energy level and below the next lowest allowed energy state.[3] The highest allowed state is known as the valence band edge (top of the red box labeled "VB" in Figure 1.1) while the next lowest allowed energy state is known as the conduction band minimum (bottom of blue box labeled "CB" in Figure 1.1).The resulting gap of forbidden energy states is referred to as the bandgap.

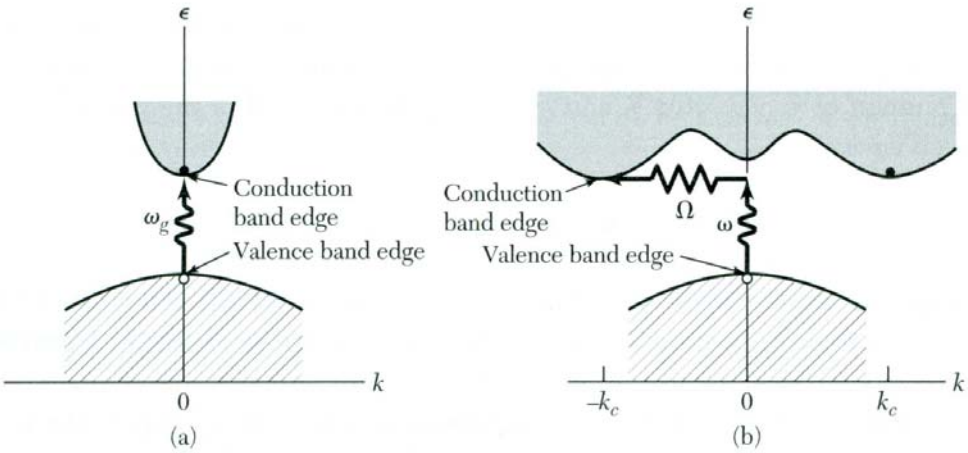

Figure 1-2 Direct and Indirect Semiconductor Band Strucure[3]

Semiconductors are generally either "direct" or "indirect" bandgap materials as shown in Figure 1.2.[3] In a direct bandgap semiconductor (Figure 1.2a) the valence band maximum and conduction band minimum have the same **k** vector and when the semiconductor is excited either through optical absorption of a photon or the application of an electric potential greater than or equal to E_g, the electron is promoted into the conduction band and has an energy $E=h\omega_g$.

The valence band maximum and conduction band minimum have different **k** vectors for indirect bandgap semiconductors as shown in Figure 1.2b. In order for excitation to occur in an

indirect bandgap material, the excited electron must change its **k** vector (in Figure 1.2b from $\mathbf{k}_0$ to +/- $\mathbf{k}_c$) in order to be promoted into the conduction band. In this case a phonon, a lattice vibrational mode, labeled **Ω** in Figure 1.2b is needed. This process is also known as phonon-assisted excitation, and results in a conduction band electron with energy less that Eg due to the exciton-phonon interaction. This electron-phonon interaction makes indirect bandgap semiconductors such as Si less energy efficient than direct bandgap materials such as Ge or CdSe.

Effects of Quantum Confinement

Reducing the physical size of the semiconductor crystal lattice into the "quantum confined" or "quantized" size regime introduces several novel effects on the electronic properties of a semiconductor. The degree to which these properties change depends on the degree of confinement: confining the electron-hole pair in one direction results in a "quantum well," two dimensional confinement results in a "quantum wire," and lastly physical confinement in all three dimensions creates a "quantum dot."[2] The two main manifestations of quantum confinement in semiconductors are an increase in band gap and a restructuring of the density of states in the valence and conduction bands.

Band gap expansion

The most common exploitation of quantum confinement in semiconductors is the expansion of the materials band gap. All three categories of nanostructures display an energy shift in both their valence bands and conduction bands relative to their bulk positions. "Band gap engineering"[2] refers to the practice of tailoring the valence band maximum and conduction band minimum by controlling the physical dimensions of the material through careful control of the semiconductor's growth.

When the exciton is confined by the dimensions of the material, the electron and hole can no longer reach their desired, "natural" distance from one another. The Brus Equation given below describes the increase in bandgap energy with respect to the radius or thickness of a semiconductor:[4]

$$E_R = E_g + (h^2\pi^2/2R^2)(1/m_e + 1/m_h) - (1.8e^2/\varepsilon R) \qquad (3)$$

where E_g is the material's bulk bandgap, h is Planck's constant, m_e and m_h are the effective masses of the electron and hole respectively, e is the elementary charge of an electron and ε is

the material's dielectric constant. The major factor in the bandgap increase according to the Brus Equation is the $1/R^2$ term, expressing the radius or thickness of the material in meters quickly leads to a very large increase. The final term in the expression, often called the "Coulombic factor" makes significant contributions to the bandgap increase at very small (generally less than 1nm) particle size/thickness. Table 1.1 below list the bandgap energies and exciton radii of several common semiconductors:[2]

Table 1-1.1 Bandgaps and Exciton Radii of Common Semiconductors

Material	Classification	Bandgap (eV)	Exciton Radius (nm)
Si	IV	1.1	4.3
Ge	IV	0.66	25
GaAs	III-V	1.42	12.5
CdS	II-VI	2.583	2.8
CdSe	II-VI	1.89	4.9 (6.0)[5]

Density of States

In "Bulk Semiconductors" above it was pointed out that the density of states in the valence and conduction bands are continuous due to the "particle-in-a-box" nature of the exciton and the "infinite" nature of the crystal lattice. When the exciton is spatially confined by the size of the material to dimensions smaller than those listed in Table 1.1 for example, the box begins to shrink and the energies of the intraband states begins to become separated by more than the thermal energy k_BT. Depending on the degree of quantum confinement (one, two, or three degrees) the density of states in the conduction band and valence band begins to take on a different "shape" seen in Figure 1-3 below:[2]

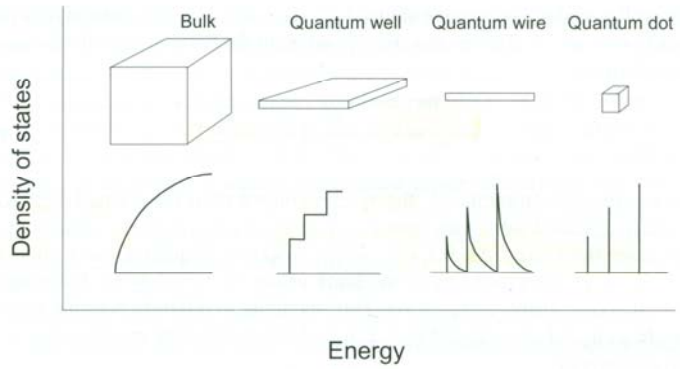

Figure 1-3 Density of States for Quantum Confined Structures[2]

The smooth curve under "bulk" reflects the continuous nature of the density of states previously attributed to the "infinite" nature of the crystal lattice. The single degree of quantum confinement present in a quantum well introduces the step-wise increase in states as the energy level increases and can be mathematically expressed by:

$$D(E) = m_e/\pi^2$$

Where E is determined by:

$$E_{n,\mathbf{k}x,\mathbf{k}y} = E_c + (n^2h^2/8m_el^2) + (h^2(\mathbf{k}_x{}^2+\mathbf{k}_y{}^2))/2m_e)$$

Where E_c is the conduction band edge, n is the princaple quantum number of the electron in the quantum well, h is Planck's Constant, m_e is the effective mass of the electron, and $\mathbf{k}_x$ and $\mathbf{k}_y$ are the free particle vectors in the unconfined dimensions. To find the density of states in the valence band the effective mass of the hole (m_h) can be substituted for m_e and the valence band maximum energy E_v for E_c. In the case of quantum wells, only one dimension (z in the above equation) is quantized and represented by l while the "bulk" dimensions remain in the xy plane where the electron is free to move. So all values of n for a given $\mathbf{k}_x$ and $\mathbf{k}_y$ have the same value and D(E) only increases step-wise when $\mathbf{k}_x$ and $\mathbf{k}_y$ increase.

Similarly for quantum wires the density of states is expressed as the derivative of:

$$E_{nx,nz,\mathbf{k}y} = Ec + (n_x{}^2h^2/8m_el_x{}^2) + (n_z{}^2h^2/8m_el_z{}^2) + (h^2\mathbf{k}_y{}^2/2m_e)$$

With respect to E yields:

$$D(E) \alpha (E-E_{nx,nz})^{1/2}$$

which gives rise to the sharp increases (near $\mathbf{k}_y$ =0) followed by the exponential decays shown under "quantum wire" in Figure 1.4 as $\mathbf{k}_y$ increases.

Finally the sharp singular, discrete, values for D(E) in quantum dots arise from taking the derivative with respect to E of:

$$E_{nx,ny,nz} = (h^2/8m_e)[(n_x/l_x)^2 + (n_y/l_y)^2 + (n_z/l_z)^2]$$

This gives:

$$D(E) \alpha \Sigma n \, \delta(E-En)$$

giving D(E) nonzero values only at energies associated with the n numbers from the above equation. These discrete values give rise to the strong optical properties of quantum wires and quantum dots by increasing the so called "oscillator strength," giving the material very sharp, well defined absorption and emission properties[2].

The "Big" Picture

Combining bandgap engineering and the reduction in the density of states for a material upon quantum confinement allows for quantum confined structures to be very versatile and for scientists to design the structure to fit a wide range of applications. The combined effects of bandgap expansion and the quantization of the density of states for a quantum dot are illustrated in Figure 1.4 below.

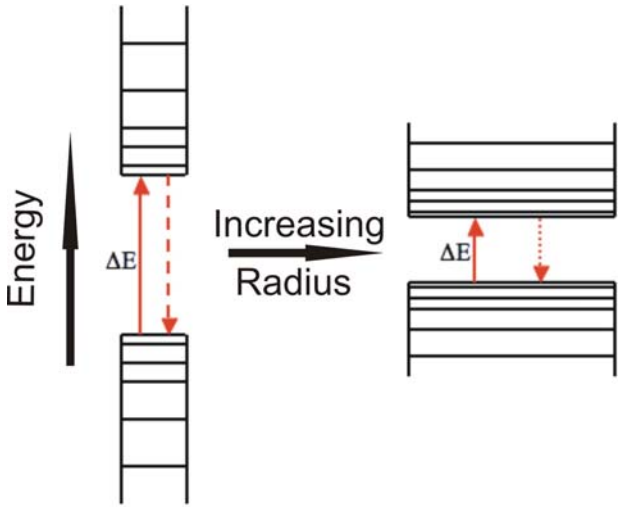

Figure 1-4 Changes in Quantum Dot Electronic Structure with Respect to Radius

When a quantum dot is "small," the bandgap increase from the bulk is very large as depicted on the left in Figure 1-4. The small radius of the material also leads to intra-band energy states that are separated by "large" amounts of energy due to the reduction of the particle in a box dimension. As the material's radius or thickness is increased the bandgap shrinks to energy closer to the bulk E_g and the energy levels within the valence band and conduction band get closer together as seen with the energy diagram on the right in Figure 1-4. The ability to

control both of these properties has allowed quantum dots to become one of the most widely applicable nanostructures in the past 20 years.

Quantum Dot Growth

The basic electronic properties of a quantum dot illustrated above, namely the size-dependant bandgap and the discrete intra-band states, have generated considerable interest in studying these materials, in particular cadmium selenide (CdSe)[6-9]. Thorough study of the electronic properties and applications of CdSe quantum dots has only been made possible through the ready supply of high-quality particles. In the following section, several methods of bench top quantum dot synthesis will be discussed followed by a discussion on the basics of quantum dot growth kinetics.

Inverse Micelle Synthesis

The inverse micelle synthesis of CdSe quantum dots became popular in the 1980's most notably in the Brus group at AT&T's Bell Laboratory to synthesize quantum dots of CdSe[4], CdS,[4] (CdSe)ZnS and (CdSe)ZnSe heterostructures,[10, 11] as well as (ZnS)CdSe core-shell heterotructures.[12]

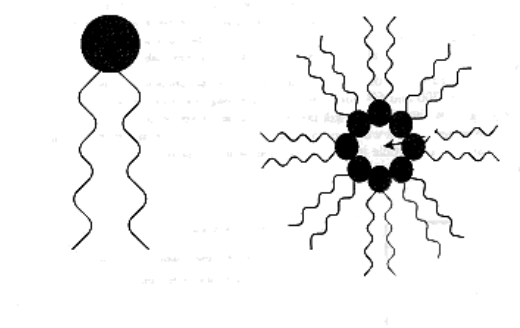

Figure 1-5 Surfactant Molecules for Inverse Micelle Reactors[13]

The basic concept of an inverse micelle synthesis is that a surfactant molecule such as bis((2-ethylhexyl)sulfosuccinate) commonly known as AOT can be added to an emulsion of water and a hydrophobic solvent such as hexane or heptane to form pools of hydrophilic growth centers as pictured in Figure 1-5 above.[13] AOT has been reported in several publications as the surfactant of choice for II-VI semiconductor quantum dot synthesis.[4, 10-12] AOT possesses a hydrophilic head group (sulfosuccinate) with a hydrophobic tail (the 2ethylhexyl carbon chains). In a hydrophobic medium such as heptane the hydrophilic head groups will orient themselves

towards the nano-droplets of water and stabilize them, allowing precursor to diffuse through the hydrophobic region into the water pool.

The major factor for controlling the size of the quantum dots produced in an inverse micelle reactor is the ratio of water to the surfactant molecule, referred to as W:[12]

$$W = [H_2O]/[AOT]$$

Varying this ratio will allow for the expansion or reduction in the volume of the water pool and therefore the volume and radius of the quantum dot formed within.

Standard inverse micelle synthesis generally involve the formation of the inverse micelle reactors by first mixing the surfactant molecule and degassed water into a degassed organic solvent[10]. Once the microemulsion is homogeneous, cadmium salts such as $Cd(ClO_4)_2 \cdot 6H_2O$ or $Cd(CH_3)_2$ and selenium precursors such as Na_2Se or $(TMS)_2Se$ are added.[12] The surfactant coated particles are recovered by evaporating the heptane to leave a colored powder.

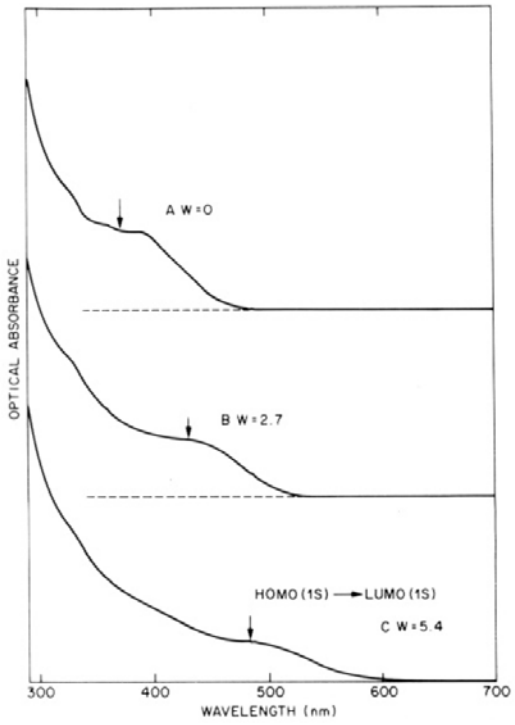

Figure 1-6 Quantum Dot Size with Respect to W[10]

The effects of W on the size of CdSe quantum dots is shown in Figure 1-6 above.[10] Quantum dots synthesized in an inverse micelle reactor with a W=0 are shown in the top pane (A), and display band-edge absorption of ~400 nm, while a W=2.7 yields quantum dots whose absorption feature is located at ~450 nm (B), and finally a batch of quantum dots synthesized

under W=5.4 display an absorption peak at ~475 nm. The authors determined that the W=0 quantum dots have a mean diameter of ~1.8 nm. The absorbance peaks displayed by these batches of quantum dots are not well defined, they appear broad and lack any peak-to-valley structure indicating they are of poor quality.

Inverse micelle synthesis is not without its limitations. Formation of the quantum dots occurs quickly and at room temperature, and it is generally agreed that slow growth at elevated temperature produces the best quality, defect free, quantum dots.[14]

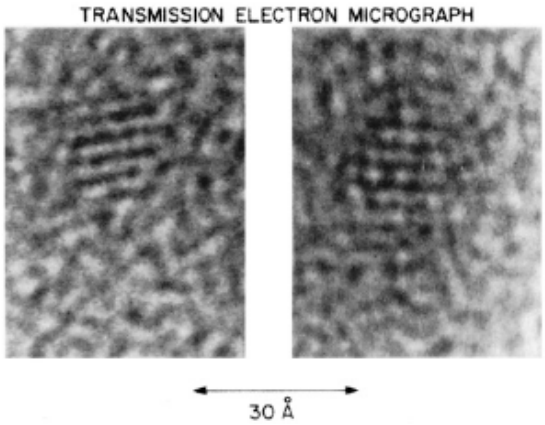

Figure 1-7 TEM Image of Inverse Micelle Prepared CdSe Quantum Dots[10]

Transmission Electron Microscopy (TEM) has long been considered one of the defacto methods for determining the crystal quality of nanoparticles. Atomic resolution makes it possible to see crystal defects such as twinning planes and lattice vacancies.[15] As Figure 1-7 shows, CdSe quantum dots prepared in an inverse micelle media are poor in quality. The lattice fringes are barely distinguishable from the background. Very small quantum dots are sometimes hard to distinguish from the background grid due to their more molecular nature, but as the scale arrow shows, these quantum dots are nearly 3 nm in diameter and should have much better defined crystal structure.

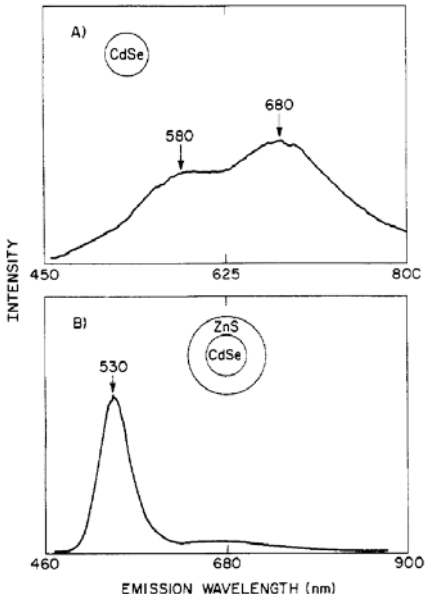

Figure 1-8 Photoluminescence of CdSe and (CdSe)ZnS Quantum Dots[10]

Further evidence of the mediocre quality of quantum dots produced in micelle synthesis can be obtained from the photoluminescence spectra of the quantum dots displayed in Figure 1-8 above[10]. In 1-8A the fluorescence of the CdSe quantum dots is broad and is actually a combination of two peaks. This sample of quantum dots have an absorbance feature of ~525 nm (not shown) while the photoluminescence spectrum has two peaks: one at 580 nm and another at 680 nm.[12] When a ZnS shell is added the band edge emission reappears at 530 nm indicating passivation of the CdSe surface and the removal of surface traps, atoms with electron orbitals not fully coordinated to surface ligands. However low intensity broad trap emission is still detected centered at 680 nm indicating that deep traps, such as lattice vacancies, located in the particle core are still present.[16, 17]

Inverse micelle synthesis of CdSe quantum dots is quick and achievable at room temperature, providing an easy method for producing large batches of quantum dots. However the persistent trap emission after a wide bandgap material was grown epitaxialy on the CdSe core is indicative of poor quality crystals. The need for readily available, high quality crystals drove research efforts to find another synthetic method for stable colloidal CdSe quantum dots.

Hot Injection Method

Quantum dot research exploded after Murray, Norris and Bawendi published their paper "Synthesis and Characterization of Nearly Monodisperse CdE (E = S, Se, Te) Semiconductor

Nanocrystals" in the Journal of the American Chemical Society in 1993.[18] The paper described the novel synthesis of cadmium chalcogenide quantum dots in a coordinating solvent at elevated temperatures that became the framework for many quantum dots synthesis strategies to come, some of which will be discussed shortly.

The hot injection method of quantum dot synthesis is able to separate nucleation and growth by a rapid temperature drop in the reaction vessel by the injection of room temperature precursors. In this case tri-n-octylphosphine oxide (TOPO) is degassed and heated to 300 °C and a mixture of $Cd(CH_3)_2$ and tri-n-octylphosphine (TOP) coordinated Se at room temperature are injected into the vessel. The heat is then restored to the vessel and quantum dot growth was achieved at 280 °C for various amounts of time. After cooling to ~60 °C the TOPO capped CdSe quantum dots were precipitated from solution by the addition of methanol and after decantation of the supernatant liquid, re-dispersed in n-butanol for further study.

Controlled growth of the quantum dots is possible through the coordinating surface ligands, in this case TOPO and TOP. The lone pairs of electrons on the alkylphosphine oxide functional group are electrostaticaly attracted to the positive charge of cadmium atoms on the surface of the particles while the lone pair of electrons on the alkylphosphine coordinates to the selenium sites on the quantum dots surface.

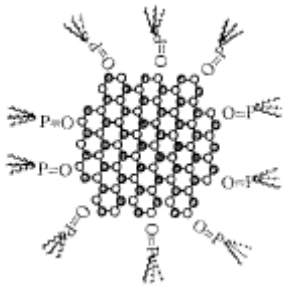

Figure 1-9 Tri-n-octylphosphine Oxide Capped CdSe Quantum Dot[19]

The alkyl chain tails of the coordinating ligands create a hydrophobic diffusion layer that the cadmium and selenium monomers must pass through in order to join the particle surface and aid in growth, as shown in Figure 1-9 above.[19] This slows down growth considerably and allows for controlled growth of the particle surface that produces a uniform ensemble of particles (the authors reported less than 5% standard deviation in size).[18] The role of the alkyl chain is critical to the temperature at which controlled growth is lost; the authors briefly mention that

uncontrolled growth of particles occurs at lower temperatures for shorter alkyl chains (butylphosphine oxide loses control at 200 °C and ethylphosphine at 100 °C are two examples given)

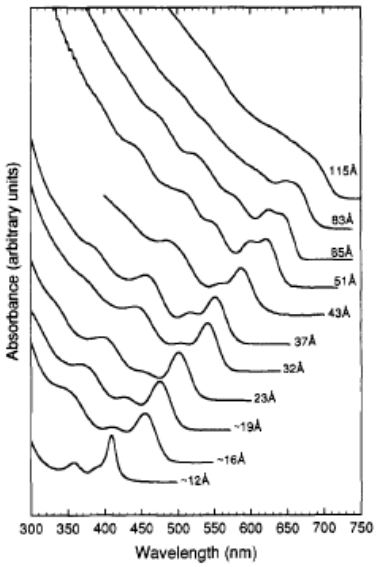

Figure 1-10 Size Dependant Absorption Features of CdSe Quantum Dots[18]

Perhaps the most frequently cited figures from the Murray publication is the series of absorption spectra with the diameter of the particles shown here in Figure 1-10.[18] This series of spectra clearly shows the absorption peak shifting the red regions of the visible spectrum as the diameter of the particles increases from ~1.2 nm to ~11.5 nm. The absorption features are very sharp for the smaller particles, with large peak-to-valley ratios indicating both narrow size dispersion and strong quantum confinement of the exciton.[5] Between ~4.3 nm and 5.1 nm the absorbance peak broadens out as a result of the quantum dots moving into the "weakly" confined size regime, where the particles radius begins to approach the exciton Bohr Radius and the electronic states begin to broaden out.[5]

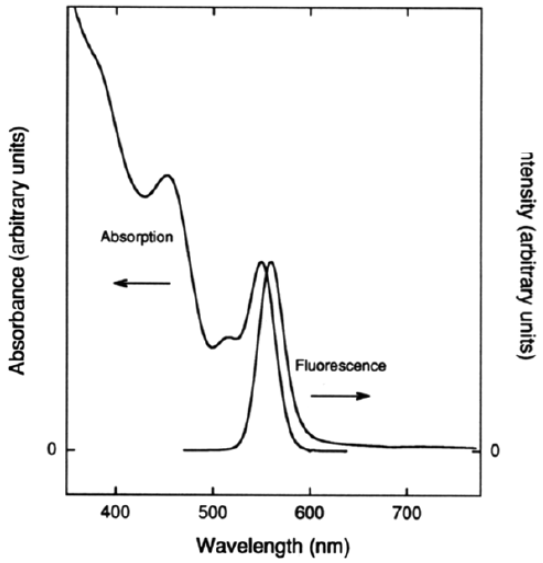

Figure 1-11 Absorbance and Photoluminescence of TOPO-capped CdSe Quantum Dots[18]

Another major difference between the quantum dots produced by Murray's hot injection synthesis and the reverse micelle synthesized particles is their emission profiles, shown in Figure 1-11[18]. The fluorescence peak depicted here is narrow, very close to the absorption peak, and displays no trap emission in the red portion of the spectrum; contrasted with the heavily red-shifted, broad trap dominated emission shown in Figure 1-8a. This indicates that quantum dots synthesized through the hot injection are of a higher quality than those produced through inverse micelle synthesis.

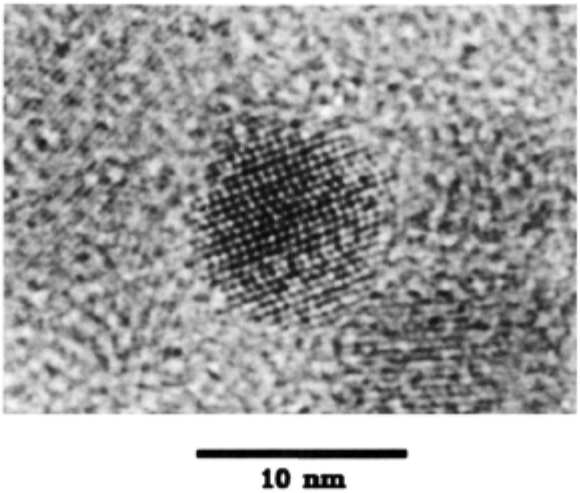

Figure 1-12 An ~8nm CdSe Quantum Dot Showing Stacking Faults in the (002) Plane[18]

The quantum dots produced through Murray's method do posses several faults. First, they possess crystal defects as seen in Figure 1-12 that reduces the fluorescence quantum yield.[18]

Most notably is a stacking fault present in nearly all the quantum dots that arises from the transition from cubic Zinc-Blende crystal structure at sub-nanometer diameters to the more stable hexagonal wurtzite crystal structure. Despite the presence of this stacking fault, the particles generated through this method are much higher in crystal quality than those made by inverse micelle synthesis shown in Figure 1-7. The crystal structure is much more defined in Figure 1-12 than in Figure 1-7. The quantum yield of particles generated through the Murray procedure was quickly improved by the addition of a CdS shell reported by Peng et. al,[19] a ZnS shell by Daboussi,[17] Hines,[16] and Talapin[20]

Adaptations of the Hot Injection Synthesis

The Murray paper has been so influential in the synthesis of CdSe, CdS, and CdTe quantum dots that in the years following its publication the synthesis was adapted and changed to suit many different requirements as described in Park's review.[21] Several of the major adjustments to the Murray procedure will now be discussed.

As mentioned in the previous section, the first major modification of Murray's procedure was to grow an epitaxial shell of a wider bandgap material on the CdSe quantum dots to passivate the surface traps and increase the fluorescence quantum yield. In all four of the papers cited above (Peng[19], Dabousi[17], Hines,[16] and Talapin[20]) the method of shell growth was simply to add $Cd(CH_3)_2$ or $Zn(CH_2CH_3)_2$ along with $(TMS)_2S$ dropwise into the reaction solution. Dropwise addition of the shell monomers was required to prevent their concentrations from rising too rapidly and causing a separate nucleation event, effectively nucleating particles of the shell material that would grow into quantum dots.

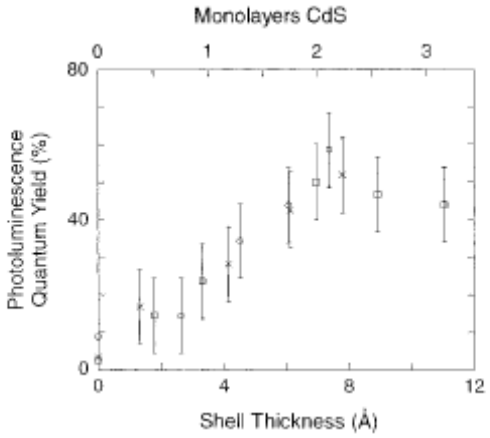

Figure 1-13 Effects of CdS Shell Thickness on CdSe Quantum Dots Quantum Yield[19]

Peng's method involved the refluxing of CdSe cores in pyridine overnight to remove the TOPO capping ligands followed by the addition of dimethyl cadmium and $(TMS)_2S$. Remarkable improvement of the quantum yield was observed shown in Figure 1-13.[19] At ~0.7 nm of CdS shell thickness the quantum yield for a 2.3 nm CdSe quantum dot approaches 55% (~7 Å).

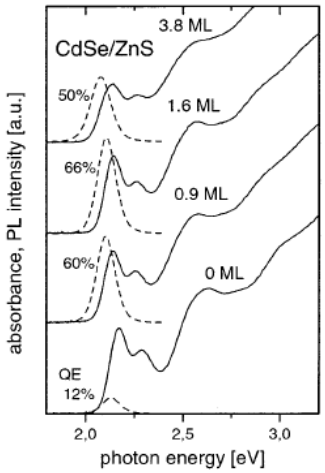

Figure 1-14 Effects of ZnS Shell Grown on CdSe Quantum Dots[20]

Talapin's results for growing a ZnS shell on CdSe quantum yield are presented in Figure 1-14 above.[20] Similar to Peng's results for CdS shell growth, there is a target shell thickness that exhibits a peak quantum yield after which increasing the thickness lowers the yield. In Figure 1-14 this target is 0.9 monolayers with a quantum yield of ~66% for a ZnS shell while Peng's report on CdS places this target thickness at ~2 monolayers of material.

The next major improvement to the hot injection growth method came when Peng began using a cadmium phosphonic acid complex[22, 23] instead of dimethyl cadmium. Dimethyl cadmium is extremely air-sensitive, pyrophoric, and environmentally unfriendly. Additionally, it was found that a phosphonic acid moiety was present in technical grade TOPO that is removed upon purification. Quite simply, the phosphonic acid and cadmium oxide were reacted in TOPO at ~300 °C, cooled and aged overnight and on the following day heated back up for injection of the traditional TOP:Se precursor. The phosphonic acid-cadmium complex was shown to be less reactive that dimethyl cadmium and provided a slower consumption of monomer and thus a slower growth rate. However, alkylphosphonic acids are costly and soon new reports of other cadmium-acid adducts began to appear in the literature: oleic acid, steric acid, and acetate being the most common.

The last major adaptation of the hot injection method published by Murray comes in the form of changing the coordinating solvent. Talapin et al. introduced a mixture of TOPO and hexadecylamine (HDA) and showed that varying the ratio of HDA to TOPO effected the quantum yield.[20] Foos et al. preformed extensive studies on the effects of primary, secondary, and tertiary amines when combined with TOPO and found that tertiary amines provide the most control over particle growth.[24] The Mullvaney group pioneered a hot injection method in a non-coordinating environment using octadecene as the major solvent.[25, 26]

Heating Up Method

The Murray's hot injection method and the adaptations of it discussed above are by far the most prevalent synthetic methods described in chemical literature. However, as the saying goes, there is more than one way to skin a cat and there are two alternatives to the hot injection method that involve nothing more than heating up the precursors together. Each of these methods offers their own distinct advantages.

Synthesis of Zinc Blende CdSe Quantum Dots

As mentioned previously, the hot injection method produces almost exclusively CdSe quantum dots with the wurtzite crystal structure. Yang et al. found that by heating cadmium myristate in the presence of selenium or tellurium powder and octadecene, it was possible to obtain exclusively zinc blende CdSe and CdTe quantum dots.[27]

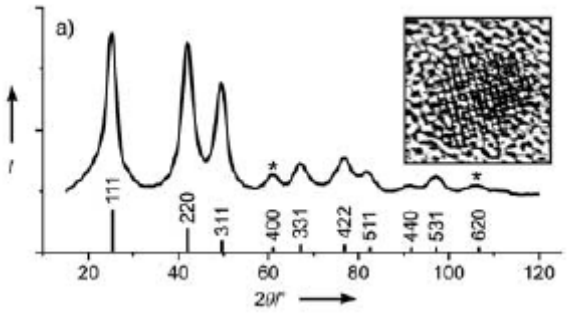

Figure 1-15 TEM and Powder XRD of a Zinc Blende CdSe Quantum Dot[27]

The zinc blende crystal structure in CdSe quantum dots can be distinguished from their wurtzite analogues in two ways: through their powder x-ray diffraction pattern and by observable lattice spacing seen on a high resolution transmission electron microscope image, both of which are presented in Figure 1-5 (taken in partiality from Figure 3 in Reference 25). First, the authors point out that the deep valley between the (220) and (311) peaks is present in bulk zinc blende CdSe but not in the wurtzite structure; and that the peaks representing the (400) and (620) peaks at $2\theta = 61.0°$ and $106.2°$ are absent in wurtzite diffraction patterns. Secondly, the lattice spacing of 0.22 nm measured from the TEM is in agreement with bulk lattice spacing for CdSe in the cubic crystal phase.

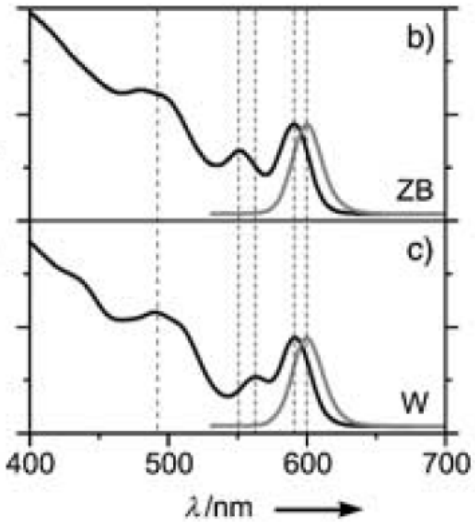

Figure 1-16 Absorbance and Fluorescence Spectra of Zinc Blende CdSe Quantum Dots[27]

Yang and co-workers also present subtle differences in the absorption and fluorescence spectra of zinc blende (ZB) produced through their procedure and of wurtzite (W) particles. Figure 1-16 (taken in partiality from Figure 3 of Reference 25) shows that while the 1st excitonic peak representing the bandgap absorption is nearly identical for ZB and W quantum dots, the two

crystal structures have different higher-order structure. Most notably the absorption peak representing the ($1S_{3/2}1Se$) and the ($2S_{3/2}1Se$) transitions are separated by a wider gap in the ZB quantum dots then in the W particles.

Single Source Precursor for CdSe Quantum Dots

In a radically different approach to synthesizing CdSe quantum dots, Cumberland et al. chose a single source precursor molecule that contains both cadmium and selenium and decomposes when heated in hexadecylamine (HDA).[28] This strategy would play an important role in the synthesis of doped CdSe quantum dots several years down the road, and will be discussed in detail later. The single source precursor (SSP) is a large phenylthiolate cage structure containing 10 cadmium atoms and 4 selenium atoms, the synthesis and structure of which was originally reported by Dance, Choy, and Scudder.[29]

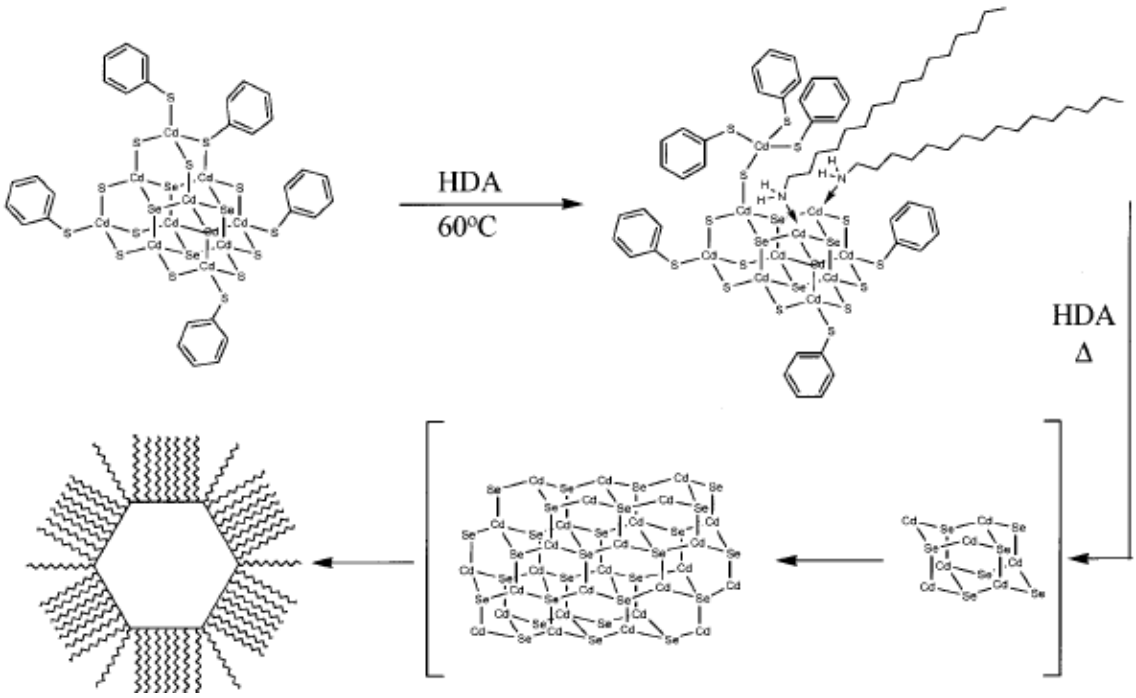

Figure 1-17 $Li_4[Cd_{10}Se_4(SPh)_{16}]$ Single Source Precursor Growth Mechanism[28]

When the SSP is heated in the presence of a coordinating amine such as HDA the lone pair of electrons on the amine co-ordinate to the cadmium atoms that compose the outer cage structure and break it open allowing the inner "seeds" of cadmium and selenium to grow into quantum dots a elevated temperature as depicted in Figure 1-17.

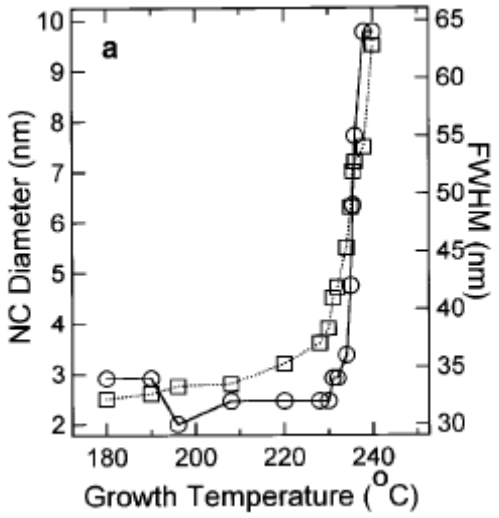

Figure 1-18 Effect of Growth Temperature on Quantum Dot Size and Fluorescence FWHM[28]

Cumberland et al.'s work showed that the growth temperature strongly effects the growth of CdSe quantum dots. As seen in Figure 1-18 at ~220-230 °C the diameter of the quantum dots begins to increase drastically (squares), while remaining relatively constant for temperatures below 220 °C. The open circles in Figure 1-18 track the FWHM of the fluorescence peak, and follow the same trend as the quantum dot diameter, due to rapid growth above 220 °C the ensemble becomes more polydisperse.

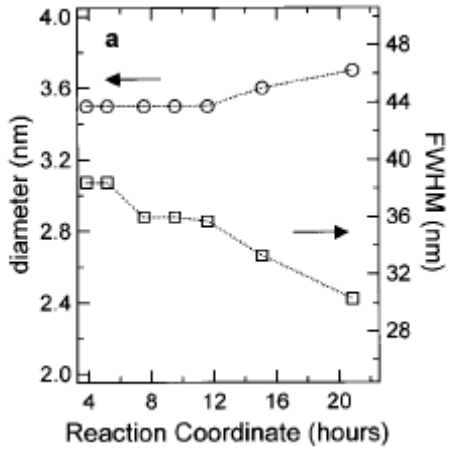

Figure 1-19 Effects of Annealing on Quantum Dot Diameter and Emission FWHM[28]

In order to obtain high quality quantum dots via this method, the authors found it necessary to anneal the quantum dots at a temperature 20 °C below their growth temperature. As seen in Figure 1-19 the quantum dots maintain a uniform diameter through up to 12 hours of

annealing, after which there is a gradual increase in size. The particles represented in Figure 1-19 have a mean diameter of ~3.5 nm through 12 hours and a final mean diameter of ~3.7 nm after 20 hours of annealing. Continued growth on this time scale could be the result of Ostwald ripening, however the squares in Figure 1-19 racking the FWHM of the fluorescence peak show a decrease over time. Ostwald ripening occurs when the growth system becomes depleted of monomers and small particles dissolve to provide monomers for larger particles to continue growing, and leads to increased size distribution of the quantum dots and a broadening of their emission properties.[30] However the data presented in Figure 1-19 shows the FWHM of the emission decreasing, indicating that Ostwald ripening is not occurring in this system.

Analysis of Growth Kinetics

Thanks in large part to the breakthroughs in quantum dot synthesis discussed above, a tremendous amount of work has been done to understand the manner in which quantum dots grow. Crystal growth in both the bulk and quantum confined regime can be broken down into three phases, also knows as the Le Mer model: nucleation, size focusing growth, and Ostwald Ripening.[2] In order to produce high quality quantum dots, careful attention must be paid to ensure that nucleation and growth are separate events and that Ostwald ripening does not occur. In the following section the thermodynamics and kinetics of each of these processes with respect to the Gibbs-Thompson equation:

$$S_r = S_b \exp(2\gamma V_m / rRT)$$

where S_r is the solubility of a crystal of radius r, S_b is the bulk solubility, V_m is the molar volume, R is the ideal gas constant and T is temperature and γ is the surface tension.[31]

Nucleation

It is generally agreed that the nucleation of crystals occurs when the solution they are being grown in becomes supersaturated with monomer. In the case of quantum dot synthesis, this occurs immediately upon injection of the precursors into the hot solvent.[32] These monomers begin to form molecular clusters that are not soluble in the solvent, and raise the Gibbs free energy (ΔG) of the system according to:

$$\Delta G_n = (4/3)\pi r^3 \Delta G_v + 4\pi\gamma r^2$$

By simple inspection of both the Gibbs-Thompson equation and the equation directly above, it is clear that certain values of r will give rise to maxima and minima in the energy diagram, which can be illustrated graphically as:[32]

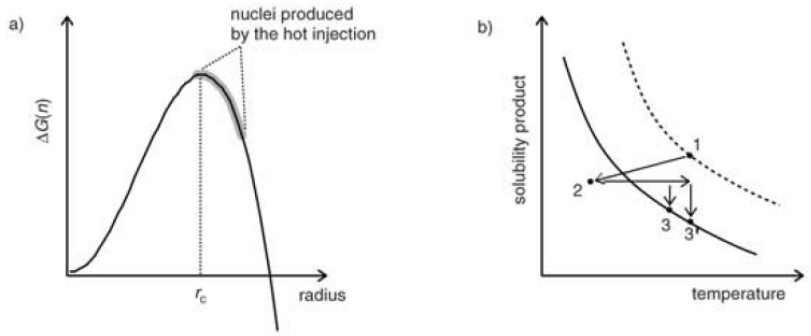

Figure 1-20 Nucleation of Quantum Dots[30]

In Figure 1-20a as the radius of the crystallites increases the ΔG(n) where n is the number of monomers in the crystallite of the solution increases until a critical radius (r^*) is reached, at which point the rapid nucleation of particles reduces the monomer concentration below the supersaturation level effectively lowering the ΔG(n). In Figure 1-20b the dark line is the thermodynamic equilibrium between Cd-TOPO and Se-TOP monomers while the dotted line is the theoretical solubility product of the monomers. At (1) the solution is supersaturated and cooling the solution leads to nucleation at (2) where the free energy of the system is reduced. (3) and (3') represent growth of the particles as the solution returns to the thermodynamic equilibrium.

The critical radius for a nucleus or "embryo" of a crystal to continue growing is described as the radius at which the nuclei will no longer dissolve based on the Gibbs-Thompson equation and will therefore continue to grow into a quantum dots and can mathematically be defined as:

$$r^* = 2\gamma abs(\Delta G_v)$$

where r^* is the critical radius for growth, γ is the surface tension, and $abs(\Delta G_v)$ is the absolute value of the Gibbs free energy. van Ebden and Mulvaney propose a kinetic model based on activation energy to explain why r^* seems to remain so uniform and leads to a uniform final product. The Le Mer model of crystal growth has several limitations, one being the fact that nucleation is not "instant" and the nucleation event from a hot injection can last up to 30 seconds after injection.[33] They define the rate of nucleation as:

$$k_{nuc} = aTexp(-\Delta G_{max}/RT)$$

where $\Delta G_{max} = 16\pi\gamma^3/3\Delta G_v^2$, γ is the surface free energy, R and T are the ideal gas constant and temperature respectively, $\Delta G_v = -(RT/V_m)\ln(S)$ is the free energy per unit volume with V_m being the molar volume of the material. Using the above equation for r^* van Ebden's equation can be rewritten as:

$$k_{nuc} = aT \exp(-4\pi r^{*2}\gamma/3RT)$$

the net effect of which is that as the reaction cools following injection the activation energy for nucleation increases and the rate slows down. Reduced nucleation rates ensure that only those nuclei formed at the moment of injection posseses the required critical radius to survive and grow into an ensemble of quantum dots with narrow size dispersion.

There are, of course, limitations on the accuracy of these models. Donegá points out that both ΔG_v and γ are not constant values for very small crystallites and can change values dramatically with both size and shape.[32] Both van Ebden and Donegá also agree that due to the rapid temperature decrease after injection it is possible that the radius of the nuclei at reduced temperature may be greater than the critical radius for growth. In other words, the critical radius at injection temperature can be larger that the critical radius at growth temperature and nuclei that "survive" at injection conditions are well beyond the critical radius under growth conditions.

Further work by the Mulvaney group on CdSe quantum dot nucleation in octadecene yielded two additional pieces of information regarding nucleation.[25] The use of a non-co-ordinating solvent removes any influences TOPO-Cd or TOP:Se surface structures might have on the surface tension terms in the above equations, i.e. that surface ligands change the particle's surface potential.

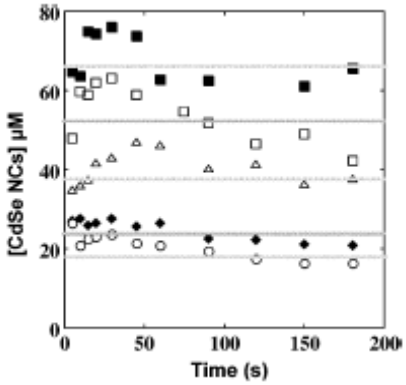

Figure 1-21 Concentration of CdSe Nuclei Over Time[25]

The results of this study showed, within the range of experimental error, uniform numbers of nuclei for a given amount of oleic acid (varying shapes) in Figure 1-21 throughout growth. They were also able to calculate that the number of monomer pairs in the critical nuclei was 75 pairs resulting in nuclei ~1 nm in diameter.

Quantum Dot Growth and Ripening

Growth and Ostwald ripening are generally studied in tandem since quantum dot growth occurs below the monomer supersaturation limit and Ostwald ripening occurs at low monomer concentration (near depletion). Since the highest quality quantum dots are achieved over a slow growth minimizing lattice defects, and Ostwald ripening results in a polydisperse ensemble of particles, the effects of radius and monomer concentration on growth rate and Ostwald ripening received a good deal of attention. A good deal of this work was carried out by the Weller group resulted in determining the zero-growth radius for a CdSe quantum dot.[30, 31] The following equation was derived based of the Gibbs-Thompson equation:

$$\frac{dr^*}{d\tau} = \frac{S - \exp[1/r^*]}{r^* + K\exp[\alpha/r^*]}$$

Where $r^* = (RT/V_m\gamma)r$ is the critical radius, $\tau = (R^2T^2DS_b/4\gamma 2V_m)t$ is time, D is the diffusion coefficient of monomer and $K = (RT/2\gamma V_m)(D/k_g^{bulk})$ with k_g^{bulk} being a first order rate constant and $S = [Monomer]_{bulk}/S_b$. Setting $dr^*/d\tau = 0$ yielded the following:

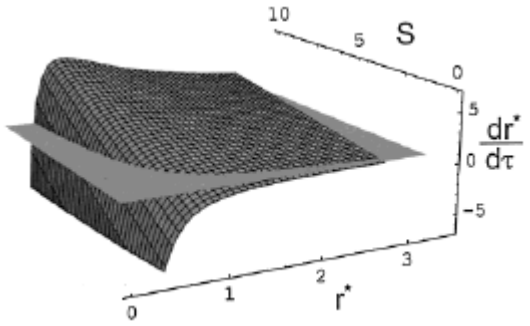

Figure 1-22 Growth Rate of Quantum Dots[30]

the grey plane at $dr^*/dt = 0$ is the zero-growth radius in Figure 1-22.[30] The growth rate of a quantum dot can also be estimated based on the critical radius and the S ratio. In area where the surface drops below the zero-growth radius plane, the quantum dot will dissolve and Ostwald ripening will occur. It can also be inferred that for high S ratios the growth rate is almost always positive with the exception being for r^* values below ~1 nm. By determining the zero-growth

radius for a given set of experimental conditions, it is possible to alter the concentrations of monomers in solution to narrow the size distribution of the particles without increasing the average size of the collective particle population.

Quantum Rods, Tetrapods and Magic Sized Nanoclusters

One of the by-products of the study of both quantum dot growth methods and in-depth investigation of the growth kinetics was the discovery of secondary nanostructures. The Alivisatos group at the University of California at Berkeley published a series of papers detailing the synthesis of quantum rods[23, 34], quantum rice[23], tetrapods[23, 34-36], and higher branched structures[37]. Along with being able to form new structures in the quantize size regime, the phenomenon of magic sized nanoclusters (MSNCs) recived considerable attention.[36, 38]

Peng and Peng adapted the Gibbs-Thompson equation and the chemical potential of a nanocrystal defined as:

$$\mu_r = \mu_b + 2\sigma V_m/rRT$$

and the surface to core atom ratio:

$$\delta = (k_1 4\pi r^2)/ (k_2 4\pi r^3/3) = k_3/r$$

to show that:

$$\mu_r \alpha \delta$$

meaning that the chemical potential of a nanocrystal is proportional to the surface atoms which contain uncoordinated electron orbitals or "dangling bonds." Therefore, they reason, the chemical potential can be a driving force for generating different shape of nanocrystals, and therefore monomer concentration will drive shape evolution.

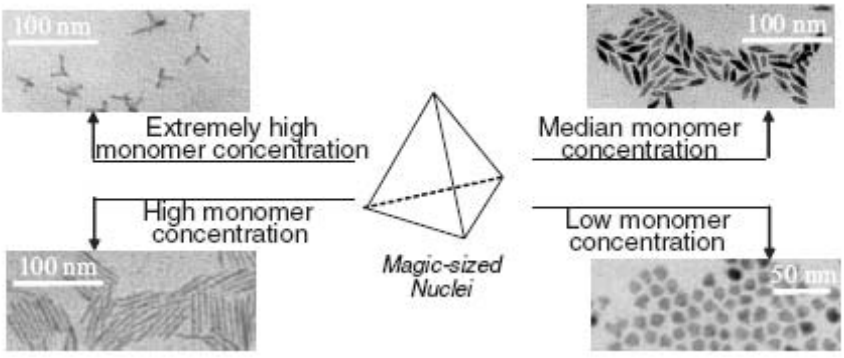

Figure 1-23 Nanocrystal Shapes Determined by Monomer Concentration[39]

Figure 1-23 summarizes the effects of monomer concentration on nanocrystal shape evolution.[39] Peng argues that all nanocrystals begin with a magic sized nanocluster that grows into a spherical dot at low monomer levels (lower right) or into rice shaped particles (upper right). Higher concentrations of monomer (0.06-0.27 mol/kg) lead to quantum wires (lower left) and branched tetrapods at monomer concentrations above 0.4 mol/kg.

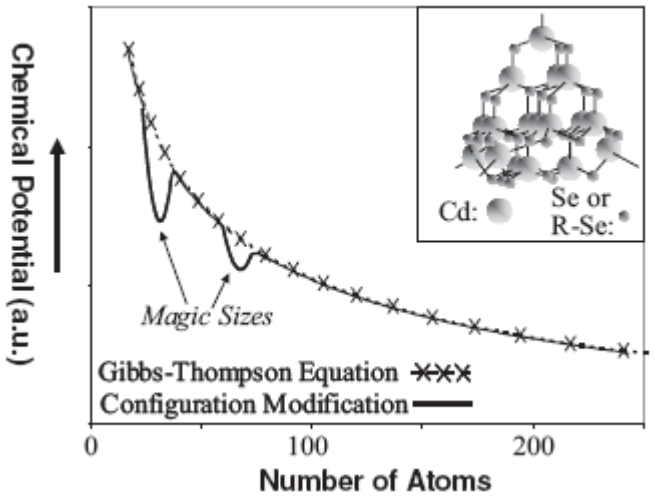

Figure 1-24 Magic-sized Nanoclusters as a Result of Localized Chemical Potentials[34]

The magic-sized seed at the center of Figure 1-23 itself has attracted attention due to it's ultra-stable nature in solution.[36] Research on magic-size phenomenon generally agree that magic-sized nanoclusters posses "closed shell" surface morphologies created by very specific numbers of CdSe pairs that result in perfect tetrahedral bonding schemes with no dangling bonds on their surface. In Figure -24 two local minimums that deviate from the Gibbs-Thompson profile denote two monomer pair numbers that cause a closed-shell surface configuration.[39] At these two local potential minimum, nanoclusters can form that are ultra-stable and resistant to further growth due to the energy penalty associated with adding a new monomer pair and driving the cluster out of its potential well. The magic-sized nanocluster pictured in the inset is the $(CdSe)_{17}$ reported by Soloviev et al.[40]

Optical Properties of Quantum Dots

The discrete energy levels that comprise the conduction and valence band density of states (DoS) discussed at the beginning of this chapter make optical absorption and fluorescence spectroscopy powerful tools for characterizing quantum dots. This section will discuss the general results of

several spectroscopic techniques that have given researchers a better understanding of how the electron-hole pair behaves inside a quantum dot.

Absorption and Photoluminescence

Standard absorption and fluorescence spectroscopy are the most common method for initial characterization of quantum dots. As mentioned in previous sections, quantum dots display size dependant bandgaps and therefore strong band-edge absorption features. For this reason, traditional absorbance and fluorescence spectroscopy is predominantly used to determine the size of quantum dots. Due to the hydrogen-like model that the electron-hole pair is based on, these optical transitions are referred to in "hydrogen like" terms. For instance, the dominant band edge absorption peak is commonly called the $1S_e$-$1S_h$ transition; and can be thought of as the n=1 orbital of a hydrogen atom.

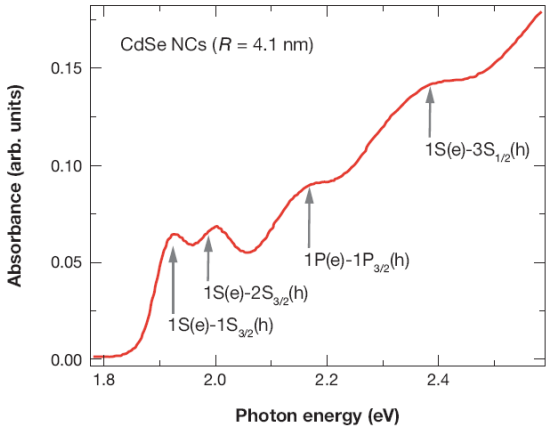

Figure 1-25 Absorbance Spectrum of CdSe Quantum Dots Showing Higher Order Transitions[41]

In Figure 1-25 above, the absorbance spectrum of a very monodisperse sample of CdSe quantum dots is shown with various peaks labeled according to the electron and hole energy levels associated with the absorbance transition.[41] In this case it is possible to see several higher order excitonic transitions such as the $1S_e$-$2S_{(3/2)h}$ and $1P_e$-$1P_{(3/2)h}$ absorbance peaks. Smaller quantum dots often do not display the $1S_e$-$2S_{(3/2)h}$ transition where strong confinement of the electron-hole pair does not allow efficient coupling of the 1S conduction band energy level to the 2S hole state and generally only the $1P_e$-$1P_{(3/2)h}$ transition is observable above the $1S_e$-$1S_{(3/2)h}$ band-edge feature.

It is also important to make note that the angular momentum of the hole's wave-function plays an important role in the absorbance spectrum. From Figure 1-25 it is clear that not all values of l translate into allowed optical transitions. For instance the $1S_e$-$1S_{(1/2)h}$ couple is missing, indicating that the 1S(1/2)h energy level is a "dark" state.[42]

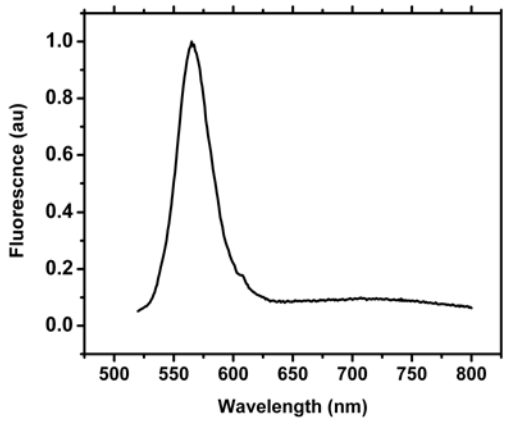

Figure 1-26 Band-edge Fluorescence of CdSe Quantum Dots

The fluorescence spectrum of CdSe quantum dots produced via the TOP/TOPO hot injection method in the course of this work is shown without complimentary absorbance data in Figure 1-26 above. In this case, the quantum dots displayed a $1S_e$-$1S_{(3/2)h}$ absorption peak at ~540 nm so excitation occurred at 520 nm. The dominant fluorescence peak associated with the bad-edge excitation is located at ~560 nm, which arises from electro-hole recombination. This spectrum also displayed a broad (~625-800 nm) weak peak that is indicative of surface trap emission. In this case, the electron-hole pair encounters a "trap" on the particle surface such as a dangling bond and the ensuing collision causes a moderate amount of energy to be transferred to the defect and the resulting emitted photon from electron-hole recombination has less energy than band-edge carrier recombination. As discussed in the section on adaptations of the Murray synthesis, the addition of a CdS or ZnS shell will eliminate trap emission by filling unoccupied electron orbitals of surface atoms (dangling bonds).

Fluorescence spectroscopy can also provide information on the size distribution of a quantum dot sample. Not all quantum dots in a sample are uniform in size, rather the absorbance and fluorescence spectrum are composites of a "family" of quantum dots centered around an average size. Fluorescence spectroscopy is more sensitive to this distribution, as the composite emission peak will broaden as the size distribution of the particles increases. Gaussian curve

fitting can be used to determine the full-width-half-maximum (FWHM) value of the fluorescence peak, i.e. the width of the peak at half the maximum intensity. The larger the FWHM of the fluorescence peak, the more polydisperse the quantum dots are.

Absorption and fluorescence spectroscopy are commonly combined to determine the quantum yield of a sample of quantum dots. The quantum yield of a sample is the ratio of photons emitted to the number of photons absorbed compared to the same ratio for a standard dye molecule such as Rhodamine-6G:

$$[PL_{QD}/Abs_{QD}]/[PL_{R6G}/Abs_{R6G}]$$

In this example Rhodamine 6G is selected because it has an absorption peak at 480 nm which is generally above the $1S_e$-$1S_{(3/2)h}$ band-edge absorption peak for CdSe quantum dots and the Rhodamine 6G dye in ethanol has a 95% quantum yield. Quantum yield studies are used to quantify the quality of the quantum dots produced, particles containing very few defects or dangling bonds will have higher quantum yields than particles with poorly passivated surfaces or deep core crystal structure defects that act as sites for non-radiative exciton recombination. Bare CdSe quantum dots passivated by ligands such as TOPO and HDA often display quantum yields no higher than a few percent compared to R6G. However the addition of a ZnS or CdS shell causes the quantum yield to increase substantially, often reaching values higher than 50%.

Transient Absorption

Traditional absorption and fluorescence spectroscopy can tell a good deal about the simple optical properties of quantum dots. Information such as size, size distribution, surface traps and crystal defects can quickly be determined through these techniques. Looking back at Figure 1-25 it is clear that there are multiple electron and hole states available for occupation given photons of sufficient energy, i.e. it is possible to create an electron-hole pair that initially occupies the $1P_e$-$1P_{(3/2)h}$ energy level which is higher in energy than the band-edge transition.

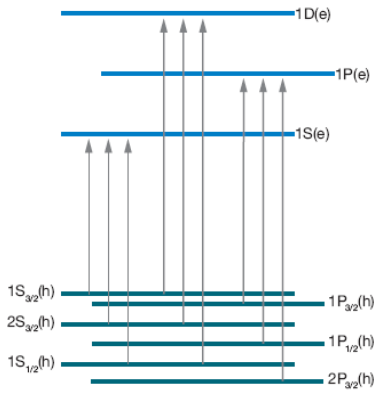

Figure 1-27 Electron-Hole Pair Transition in Quantum Dots[41]

As discussed in the previous section on absorbance and fluorescence spectroscopy the photoluminescence of quantum dots comes from electron-hole pairs in the $1S_e$-$1S_{(3/2)h}$ energy level; so excitons occupying higher energy levels such as those shown in Figure 1-27 above[41] must relax down to the emitting state. These relaxations occur on very fast timescales, in the range of picoseconds (10^{-12}) down to femtoseconds (10^{-15}).[43-45]

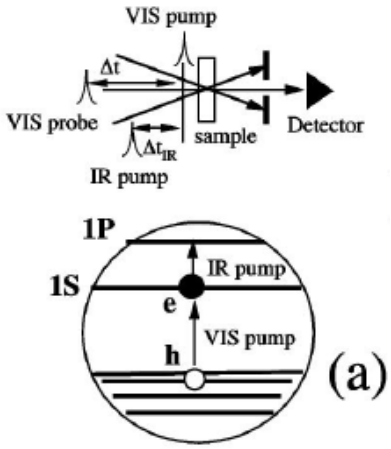

Figure 1-28 Schematic of Pump-Probe Spectroscopy Showing Intra-band Electron Transitions[46]

One method for observing these dynamics is transient absorption pump-probe spectroscopy where a sample of quantum dots is excited by a pulse of light to form an exciton (pump) which is then re-excited by a second pulse of light (probe) as shown in Figure 1-28 above:[46] In this case, the pump pulse creates an exciton that occupies the 1S electron level while the pulse excites the electron from the 1S to 1P level. In techniques such as this, the pump pulse is generally composed of visible light photons that posses the required energy to create the

electron-hole pair while the probe pulse is tuned to the energy difference between intra-band energy levels (typically in the infra-red region) which can be calculated using simple "particle in a box" equations.

Occupation of the conduction band energy levels will create changes in the absorption spectrum of the quantum dots, since partial occupation of an energy level will result in lowering the probability a second electron can occupy the same level and therefore a weaker absorption signal. Similarly, total occupation of an energy level will completely "bleach" the energy level from the spectrum since full occupation makes it impossible for another electron to occupy the orbital. Since the hole is able to quickly relax through its close packed density of states the transient features are caused by electron energy level occupation.[44, 47] By altering the time between pump and probe pulses and observing the changes in the absorption spectrum it is possible to see how electrons relax from higher energy levels down to the 1S state where it can emit a photon.

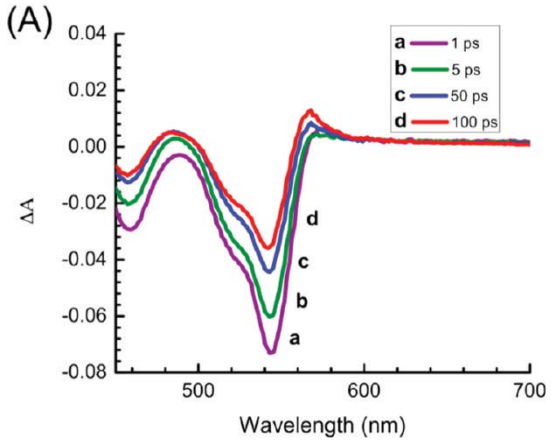

Figure 1-29 Transient Absorption Spectrum of CdSe Quantum Dots[48]

A typical transient absorption signal from CdSe quantum dots is presented in Figure 1-29 above.[48] The quantum dots samples have a $1S_e$-$1S_{(3/2)h}$ band-edge transition at ~540 nm while the broad hump at ~480 nm is the $1P_e$-$1P_{(3/2)h}$ energy level . A probe pulse arriving 1 ps (a) after the pump pulse shows a change in absorption of ~0.075 indicating that the 1S state is partially bleached due to the exciton occupying one of the two available electron states. Probe pulses arriving at later time intervals show less negative changes in their spectrum indicating that electron occupation of the 1S state is decreasing as the quantum dots give off photons, making it more probably that another electron can fill the 1S state.

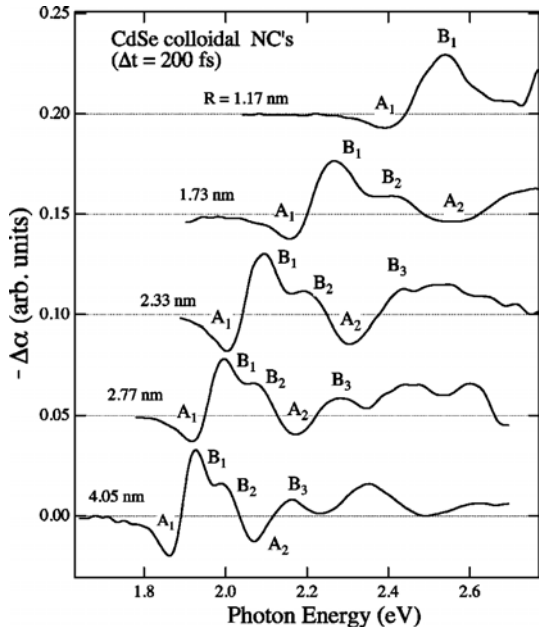

Figure 1-30 Derivative Transient Absorption of CdSe Quantum Dots[44]

Closer inspection of Figure 1-29 shows several less intense peaks and shoulders compared to the major transient signal associated with the band-edge absorption feature. Figure 1-30 shows these features in closer detail on an –Δ scale where positive changes correspond to negative changes in absorption and make it easier to see when bleaching is increasing.[44] Figure 1-30 also shows how the transient features are related to the size of the quantum dots probed, for instance very small quantum dots (radius = 1.17 nm at the top) only show the A_1 and B_1 features while larger quantum dots (radius = 4.05 nm at the bottom) show two "A" features and three "B" transitions. These features arise due to lowering the intraband energy level values as the quantum dot size increases.

The spectrum shown in Figure 1-30 are complicated to interpret but in the end yield very useful information on how electrons relax down to the 1S emitting state. The increase in absorption slightly red shifted from the band-edge absorption feature (A_1) is caused by "Coulombic many-particle interactions" caused by the formation of bi-excitons and trions. [43, 44, 46] The formation of these "particles" induces an electric filed that activates a Stark effect, which splits the angular momentum degeneracy of the 1S orbital and "turns on" a lower energy l orbital making it optically active. This phenomenon is called photoinduced absorption and is also seen for the 1P orbital as well, where it is labeled as A_2 in figure 1-30.

The other "B" peaks in Figure 1-30 are linked to the bleaching of the higher-order excitonic peaks seen in Figure 1-25. Klimov and coworker have assigned B_2 to the$1S_e$-$2S_{(3/2)h}$ transition and B_3 to the $1P_e$-$1P_{(3/2)h}$ transition based on their calculated energy levels compared to the 1S energy level and their overlapping positions with the same energy levels indicated in Figure 1-25.[44] By comparing how the B_2 and B_3 bleach signals recover over time Klimov and co-workers were able to determine electron relaxation from B_2 to B_1 and B_2 to B_1 both occur over ~300 fs.

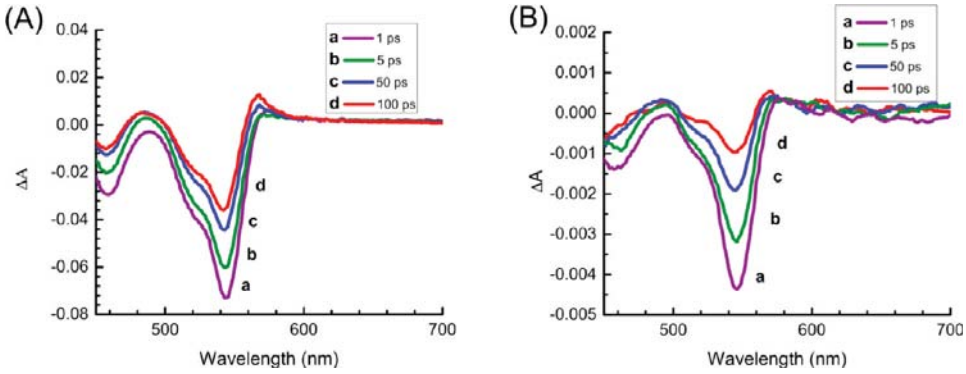

Figure 1-31 Transient Absorption Spectrum of CdSe Quantum Dots in Solution and CdSe Quantum Dots Attached to Carbon Nano-Cup Fibers[48]

Finally transient absorption has been used to show how electrons can be transferred from the quantum dot conduction band into other nano-structures[48]. Figure 1-31 (A) are the same quantum dots shown in Figure 1-29 above while the quantum dots in (B) have been attached to carbon nano-cup stacks with thioglycolic acid (TGA).[48] The main piece of information to take away from Figure 1-31 is that the quantum dots attached to the nano-cup stacks show much faster recovery of the 1S bleach. In (A) the 1 ps spectrum shows a ΔA change of 0.075 while the 1 ps spectrum in (B) has a ΔA of 0.004, indicating that at times as low as 1 ps the electron in the 1S conduction band level is no longer occupying the 1S energy level, and has been transferred to the carbon nano-cup stack. Second, while the quantum dots in solution have only recovered about one half of their bleach at 100 ps in (A), after 100 ps the quantum dots attached to the nano-cups in (B) have recovered ~75% of their bleach. Similar results have been reported for quantum dots attached to TiO_2 structures and will be discussed more in-depth in a later section.[8, 49-51]

Time-Resolved Photoluminescence

The fluorescent properties of quantum dots are strongly tied to the condition of the particle surface.[16] The high surface atom to bulk atom ratios mean up to one third of the atoms in a quantum dot are located on the surface. Defects in the crystal structure at the surface such as uncoordinated electron orbitals, missing atoms, or impurity atoms can have a dramatic effect on the emission characteristics in an ensemble of quantum dots. As discussed above, static fluorescence spectroscopy can tell some of the story, but in order to get a true picture of the nature of the quantum dot surface ultra-fast fluorescence spectroscopy is needed.

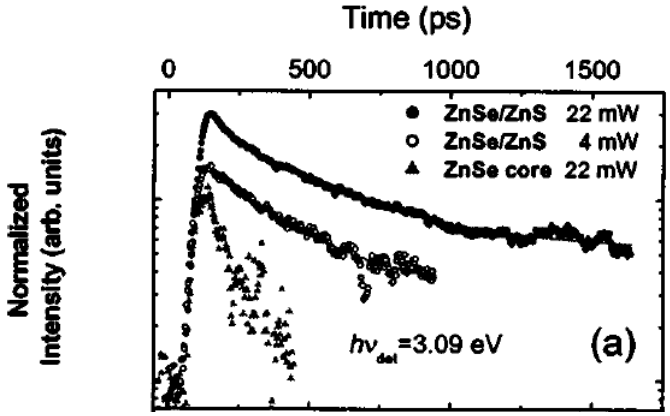

Figure 1-32 Time Resolved Fluorescence Decay for ZnSe and ZnSe@ZnS Core-Shell Quantum Dots[52]

In Figure 1-32 the fluorescence from samples of ZnSe and ZnSe@ZnS quantum dots is plotted on the picosecond time scale.[52] In this case the ZnSe only particles are represented by triangles while ZnSe@ZnS core-shell particles at two different excitation intensities are the open and closed circles. When presented on a semi-log plot as this data is, it is easy to see in this data that the ZnSe particles have a much shorter fluorescence lifetime than core-shell particles; almost all the fluorescence is gone by 500 ps while over half remains at 1000 ps for the core-shell particles. The wide bandgap ZnS coating removes surface defects that act as recombination sites for the electron-hole pair. Core only particles have surfaces with dangling bonds and lattice vacancies that cause quick recombination.

Quantum Dot Applications and Devices

The usefulness of a material only extends as far as it's versatility. In this regard, quantum dots have the potential to be one of the most useful materials science has ever given civilization. The

vast majority of quantum dots applications center around exploiting the amazing optical properties discussed in "Optical Properties of Quantum Dots." The two main categories that this work falls under are emission applications and absorption applications. Emission applications generally involve using the quantum dot's fluorescence as an indicator that a process is occurring, while absorption applications center around the quantum dot's ability to absorb light mainly in the capacity as a light harvester for solar cells.

Chemiluminescence

Chemiluminescence refers to phenomenon of light emission as the result of a chemical reaction. An everyday example of chemiluminescence is the glow-sticks we give to children on Halloween so they can be seen in the dark. The glow sticks work on the simple principle that when bent, or "cracked," two chemicals mix together and the reaction between them gives off the distinct green or orange glow. This process is generalized as:

$$A + B \rightarrow AB^{*} \rightarrow AB^{0} + h\nu$$

where AB* indicates a chemical species in the excited state and AB^0 denotes the same chemical in its ground or rest state and hν represents a photon of light given off. Chemiluminescence can be used for much more than this illustration, for example to detect pollutants in water or the presence of an unwanted chemical in a reaction.

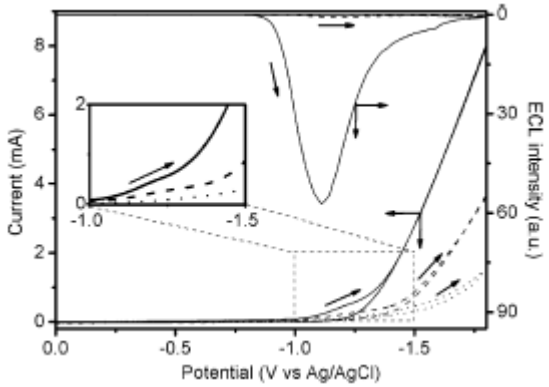

Figure 1-33 Chemiluminescence Quenching of CdSe Quantum Dots by Hydrogen Peroxide[53]

Jiang and Ju showed that a electrode covered in thioglycolic acid (TGA)modified CdSe quantum dots could be used to detect the presence of H_2O_2.[53] Figure 1-33 shows the cathodic fluorescence from the TGA capped CdSe quantum dots decreasing when hydrogen peroxide is added. The arrows indicate the direction of the cyclicvoltometery scan. In both TGA

functionalized CdSe quantum dots and TGA functionalized quantum dots in the presence of peroxide, the band-edge fluorescence occurs at ~-1.0 volts vs. the Ag/AgCl electrode, indicating that peroxide does not alter the bandgap of the particles.

It can clearly be seen from the vertical scale that adding peroxide (dashed and dotted lines) reduces the electrochemiluminescence (ECL) of the quantum dots (solid line). The authors offer the following explanation illustrated in Figure 1-26 below: the electric excitation of the quantum dots promotes an electron into the conduction band where it is able to react with peroxide around the quantum dot surface to generate the hydroxide radical (reduction of peroxide). The reduction potential of the hydroxide radical is sufficient that it accepts another electron from the quantum dot, causing the creation of an electron vacancy in the $1S_h$ energy level of the valence band that is responsible for the quenching of fluorescence from the quantum dot (hole injection).

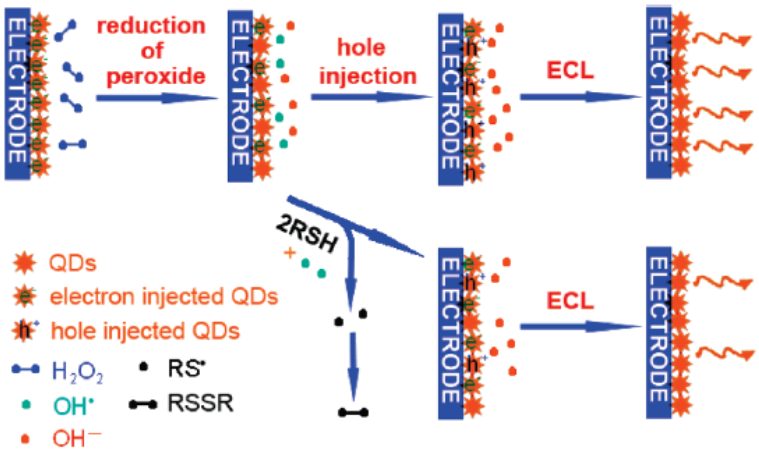

Figure 1-34 Mechanism of Electrochemiluminescence Quenching by Peroxide[53]

Jiang and Ju were also able to show that by introducing a radical scavenger such as glutathione, the ECL of the system was quenched. As the lower pathway in Figure 1-34 shows, when two thiol molecules encounter two hydroxide radicals they first form a thiol radical (black dots, $RS^{\cdot}$) which combine to form a thiolether. By removing the radical from solution, the $1S_h$ valence band level is not oxidized, and there is no bleaching of the CdSe quantum dot fluorescence. The authors note that FT-IR spectral analysis shows only S-Cd bonds, indicating no –SH groups were available to quench fluorescence.

This example illustrates the ability to use quantum dot fluorescence to detect two different chemical species in the same system. This method can be used to detect the presence of

a strong oxidizer such as peroxide through photoluminescence quenching or the presence of a radical scavenger by tracking the emergence of fluorescence as the scavenger eliminates radicals.

Fluorescence Imaging

Using quantum dots for fluorescence imaging possesses several advantages over conventional organic imaging dyes; quantum dots have narrow emission profiles whereas organic dyes have much broader photoluminescence profiles and quantum dots are more resistant to long term photobleaching than organic dye molecules.[7] Moreover, quantum dots posses the ability to be tailored to almost any need by altering their surface ligands, sometimes by simply stirring the quantum dots in an excess of the desired surface ligand, commonly a thiol-carboxylic acid species where the thiol group coordinates to the cadmium surface and the carboxylic acid creates a hydrophilic exterior.[7, 54] However this simple method creates short lived water solubility and suspensions have shelf lives of only a few days.[7, 55] Longer shelf lives are achieve through more complex procedures such as encapsulation in co-block polymers[56] or functionalized porous silicon.[57]

As an illustration of the superiority of functionalized quantum dots over organic dyes, the Alivisatos and Larabell groups applied quantum dot fluorescence to phagokinetic tracking of cancer cells, a process previously ill-suited to fluorescence imaging technique because of the short lifetimes of organic dyes.[55] Phagokinetic tracking was first proposed by Albrecht and Buehler as means for observing the mobility of live cells by tracking cell movement by the ingestion of marker molecules.[55] Traditionally this tracking was done with gold microcrystals (~0.15μm), which were difficult to incorporate into the cell culture medium and could compose up to ~1% of the cells volume over short distances. Quantum dots could be tailored to fit with the culture medium and their nanometer diameters represent a much smaller volume percentage of the cell.[55]

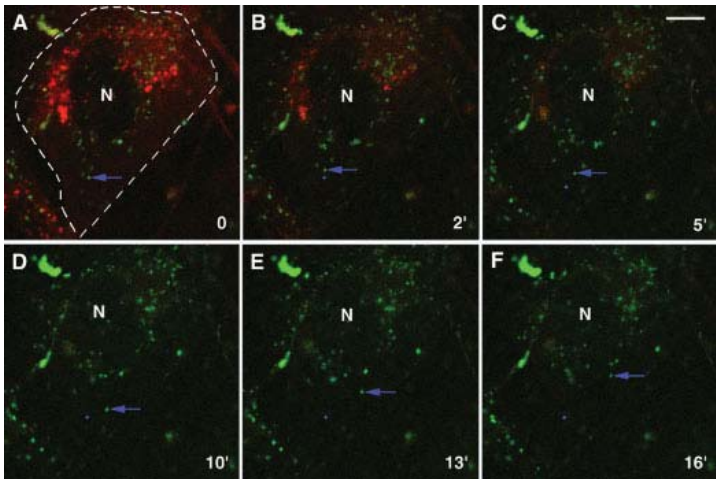

Figure 1-35 Human Mammary Epithelial Tumor Cells Cultured with Water Soluble Quantum Dots and FM4-64[55]

Human mammary epithelial tumor cells were cultured in the presence of water soluble silanized quantum dots and imaging dye FM4-64 in Figure 1-35[55]. The quantum dots appear as green light whereas the FM4-64 dye is red. Both the quantum dots and dye are encapsulated in vesicles inside the cell (white dashed boarder in A). As time elapses the FM4-64 dye degrades and is no longer visible after 10 minutes (D) while the quantum dot fluorescence remains. The blue arrow is tracking a vesicle filled with quantum dots as it travels through the cytoplasm towards the cell nucleus (N in all panes).

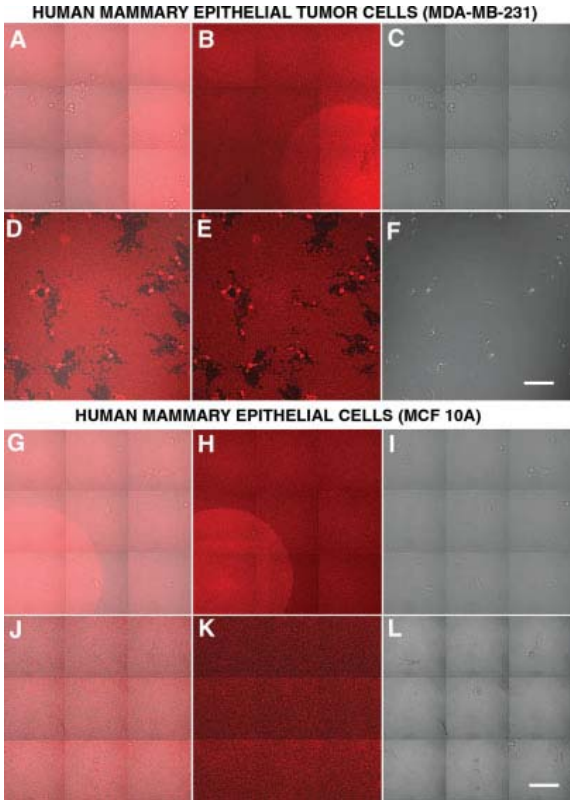

Figure 1-36 Phagokinetic Tracking of Cancer and Benign Breast Cancer Cells using CdSe Quantum Dots[55]

Tumor and non-cancerous cell phagokinetic tracking using quantum dots is presented in Figure 1-36[55]. Tumor cells are shown in the upper panes while healthy cells are tracked in the lower panes. The red color is from red-fluorescing quantum dots. Confocal fluorescence microscopy is shown in B, E, H, and K while differential interference contrast (DIC) images are shown in C, F, I, and J. Confocal and DIC images are merged in A, D, G, and J. Images B and H are at the time of 3 hours after culture while E and K are 24 hours after culture. Clearly, the tumor cells move much more than the healthy cells as evident from the large black tracks seen in E. The black tracks indicate that the tumor cells are consuming, or absorbing, the red fluorescing quantum dots as they move while the healthy cells do not. The authors use the term "voracious" to describe the manner in which the tumor cells consume the quantum dots, which can be seen 24 hours later fluorescing from inside the tumor cells.

The study discussed above highlights the potential of quantum dots in terms of biological imaging. Quantum dots were shown to have superior durability compared to a commonly used organic dye; furthermore quantum dots were able to introduce fluorescence detection to

phagokinetic tracking of small epithelial cancer cells, a technique previously impossible due to size limitations of the imaging agent.

Quantum Dot Based Solar Cells

The high absorbance cross-sections of quantum dots have led several researchers (the Klimov[58], Nozik[59] and Kamat[49] groups being the most notable) to believe that quantum dots can successfully be integrated into existing photovoltaic archetypes and open the door to the new generation of solar cells needed to meet the energy needs of the future. In addition to high rates of light absorption, the size tenability of quantum dots based on material and size increase the promise quantum dots pose in this field. Finally, the quantum confined energy states in the conduction band of quantum dots may allow for the exploitation of so called "hot electrons" and the controversial carrier multiplication or multi-exciton generation to increase the efficiency of quantum dot based solar cells[9, 41, 58-60] Currently, the highest efficiency rating for a silicon based solar cell is 25%, which is below the 33% limit predicted by Shotkey and Quessler.[61]

Quantum dots show true potential in the devices known as third generation solar cells. Generation III solar cells are based on the archetype proposed by Gratzel[62], where a wide bandgap semiconducting metal oxide such as titanium dioxide is "sensitized" with a visible light absorbing organometalic dye, traditionally containing Ruthenium.

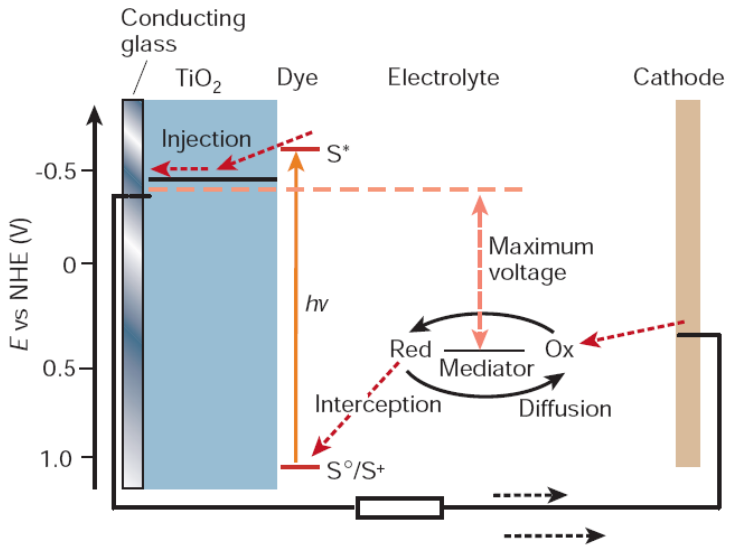

Figure 1-37 Dye Sensitized Soalr Cell[62]

The mechanism of a dye sensitized solar cell is outlined in Figure 1-37. Light is absorbed by the metal center of the dye molecule and undergoes Metal to Ligand Charge Transfer, whereby the excited electron moves into the LUMO of the organic ligands. The LUMO of the organic ligands must be higher in energy than the conduction band minimum of the metal oxide in order for rapid transfer of the electron to occur, minimizing the chances of electron-hole recombination. The dye molecule is anchored to the metal oxide by pi-conjugated ligands that are bound to the metal oxide surface through a M-OOCR bond. This bond allows for coupling to the metal oxide conduction band states and rapid electron injection from the excited dye into the metal oxide. From the metal oxide, the electrons flow through a conducting glass and into the closed circuit. On the reverse side of things, electrons from the cathode reduce an electrolyte such as the I^-/I_3^- couple. This redox pair is in a higher energy state than the ground state of the dye molecule, so reduced electrolyte will in turn transfer electrons back to the dye, allowing the cycle to repeat itself. Currently, devices based on this design are between 11% and 15% efficient in turning a photon into a usable electron in circuit.[63]

Due to their excellent size tunable bandgaps in the visible range, CdSe quantum dots have been studied as replacements for the ruthenium based dyes, which are expensive and arguably unsustainable due to the limited amount of Ruthenium in the earth's crust. The Kamat group has done extensive work on coupling CdSe quantum dots to mesopourous layers of metal oxides such as TiO_2[8, 50], SnO_2[51], and ZnO[51]. In these studies, the mesoporous metal oxide layer was dipped in thiolglycoic acid (TGA) to functionalize the surface to adsorb CdSe quantum dots of various sizes. After submerging the TGA functionalized anode in a toluene suspension of quantum dots for 12 hours, the absorbance of the TiO_2-TGA-CdSe system was measured and is shown in Figure 1-38 below.[8]

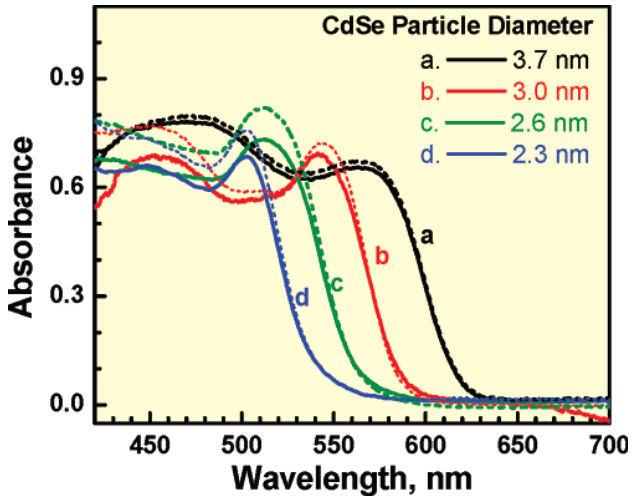

Figure 1-38 Absorbance Spectra of CdSe Quantum Dots and Quantum Dots Attached to TiO_2 Nanoparticles[8]

The absorbance spectrum of TiO_2-TGA-CdSe quantum dots (dashed lines) is almost identical to the absorbance spectrum of CdSe quantum dots in toluene (solid lines), indicating that the electronic properties of the quantum dots have not been altered by TiO_2-TGA functionalization. However, the photoluminescence of the CdSe quantum dots was found to be significantly reduced, indicating that the electrons generated by optical excitation were being transferred from the quantum dots to the TiO2 where they could no longer recombine with the hole and emit a photon.

Transient absorption spectroscopy showed that when CdSe quantum dots are adsorbed on TGA funtionalized TiO_2 the photobleaching is significantly reduced, as shown in Figure 1-31 above. When CdSe quantum dots are excited with a pump-probe pulse laser system, the 1Pe energy state is populated with electrons as well as the $1S_e$ level at the bottom of the conduction band. The so called "hot" electrons in the $1P_e$ level relax to the $1S_e$ level where they are transferred into the conduction band of the TiO_2, which eliminates photobleaching by making the quantum dot's conduction band accessible to excitation again through depopulation. In cases where the quantum dots were tethered to the metal oxide, the transitive bleach recovered (decrease in bleach indicated by a positive or negative Δ(A) in Figure1-31 more on the same time scales as quantum dots in solution. In solution, the only route for depopulation of the conduction band states is through photoemission, which occurs on the nanosecond time scale while injection from quantum dot to metal oxide occurs on the picosecond time scale (100x

faster than emission). These results are further supported by time-resolved photoluminescence decay studies shown below:[8]

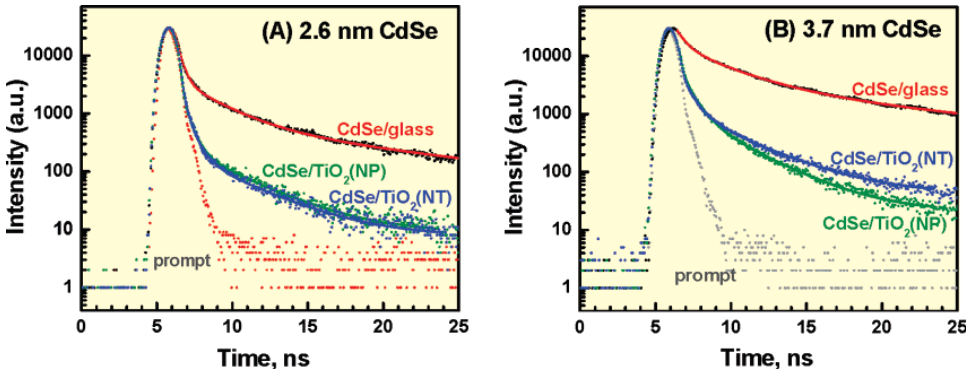

Figure 1-39 Time Resolved Fluorescence Decay Spectra of CdSe Quantum Dots Deposited on Glass and Attached to TiO_2 Nano-structures[8]

In Figure 1-39 above it is clear that for both 2.6 nm and 3.7 nm CdSe quantum dots the fluorescent lifetimes are significantly reduced for quantum dots attached to TiO_2 nano-particles (green line) and nano-tubes (blue line) than for quantum dots on glass (red line). This reduction of life-time is caused by the electrons being separated from the hole in the quantum dots by injection into the TiO_2 conduction band which is slightly lower in energy than the quantum dots 1S state. When the quantum dots are only coated on glass, there is no lower energy position for the electron to relax to and it remains in the quantum dots 1S conduction band level until normal radiative recombination can occur.

Further studies on the electron injection process revealed that charge transfer is size dependant. By measuring the Incident Photon Conversion Efficiency (IPCE) of a quantum dot sensitized solar cell, the Kamat group determined that smaller quantum dots with larger bandgaps have higher IPCE's than larger quantum dots with smaller bandgaps. The conduction band minimum of TiO_2 is at -0.5 V relative to the negative hydrogen electrode while most quantum dot conduction band minimums are at ~1-.0 V with respect to the NHE. Therefore it is energetically favorable to inject the electron generated by photoexcitation into the TiO_2 conduction band. The larger the offset between the quantum dot's 1Se level and the metal oxide's conduction band, the faster electron injection occurs.

It has also been postulated that the nature of the TiO_2 layer will play a role in the final efficiency of a Generation III photovoltaic. Some have argued that nanotubes will provide directed conduction of electrons into the closed circuit faster than a mesopourous layer of

particles due to direct contact with the anode and a less random pathway from quantum dot to circuit through a maze of particles. The Kama group again showed that TiO_2 nanotubes have a 10% IPCE efficiency increase over TiO_2 particles ~10-30 nm in diameters, shown in Figure 1-() above.

Doping Semiconductors

Doping semiconductors to increase their conductivity is the foundation of our modern electronic devices, and will be the foundation of future electronics as well. Doping is a powerful tool to introduce new properties to a material, mainly in the catagories of magnetic properties and increasing conductivity.

The intrinsic[64] (impurity concentration less than 1 part in 10^{10}) carrier concentration (n) in a bulk semiconductor is largely related by the ratio of the band gap to the thermal energy:

$$n \; 1/\alpha \; E_g/(k_B T)$$

which generally gives semiconductors resistivities between 10^{-2} and 10^{14} Ω*cm^{-1}. This means that at low temperature semiconductors have poor intrinsic conductivity (as $T \rightarrow 0$, $n \rightarrow 0$).[64] It is possible to increase the conductivity of a semiconductor through a process known as doping, intentionally adding impurity atoms that create extra electrons or electron vacancies in the crystal lattice. This limits the amount of current that can be passed through the material. In order to increase the conductivity, and the current able to pass, impurity atoms, or dopants, can be added to the host material.

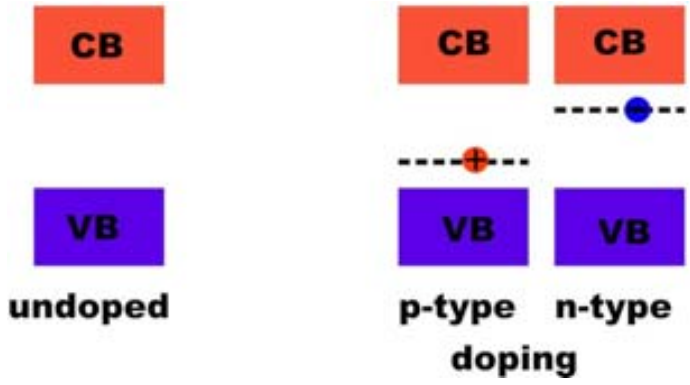

Figure 1-40 Semiconductor N- and P-Type Doping Schemes

Using silicon as an example if an atom with fewer valence electrons such as boron is added in low percentages (~1%), the boron replaces silicon atoms in the crystal lattice. Because boron has one fewer electrons than silicon, a positive vacancy is generated that can act as an electron acceptor. This is depicted as "p-type" doping in Figure 1-40 above. Similarly, if an element such as phosphorous containing an extra electron is inserted into the lattice depicted as "n-type" doping in Figure 1-40. The extra electron is weakly bound to the donor atom and is easily ionized into the conduction band by sub-bandgap voltages or photons. The donor level energy can be calculated in eV by[3]:

$$E_d = (13.6/\varepsilon^2)(m_e/m)$$

where 13.6eV is the ionization energy of hydrogen, m_e is the effective mass of an electron in the material, m is the mass of the electron-hole pair and ε is the dielectric constant of the material. Therefore the dielectric constant of the material is the determining factor in donor energy levels. A true n-type doped semiconductor has its donor electrons ionized into the conduction band at room temperature, however the number of donor electrons ionized into the conduction band can be calculated at any temperature by[3]:

$$n = (n_0 N_d)^{1/2} \exp(-E_d/2k_bT)$$

where $n_0 = 2(m_e k_B T/2\pi h^2)^{1/2}$ and N_d is the donor concentration per cm^{-3}. Complete ionization would occur at a temperature where $k_BT = E_d$ while any temperature below that will result in only partial ionization of the donor states. As an example of doping's effectiveness, the resistivity of intrinsic silicon is on the order of $1x10^5$ Ω-cm's while donor concentrations of 1ppm result in resistivities on the order of 10^{-2} Ω-cm and heavily doped Si has a resisitivity on the order of 10^{-3}.[65]

Doping bulk semiconductors is generally done through ion-beam implantation.[66] Ion beam implantation involves a lengthy process of photomasking and etching on a semiconductor wafer to expose the regions of the material that are destined to be doped either n-type or p-type followed by exposure to a molecular beam of the dopant atom and finally annealing to allow even distribution as shown in Figure 1-26.[67]

Challenges Associated with Doping Quantum Dots

Doping CdSe quantum dots has proven more difficult than bulk CdSe, in general owing to the incredibly small cystal size.[68] Despite these difficulties, successes have been reported,

particularly when transition metals have been incorporated to introduce magnetic properties to the CdSe quantum dots. However studies on carrier doping in CdSe nanostructures are few and far between.[69-72] There are two main arguments for why this is the case, one thermodynamic[73, 74] and the other kinetic.[75, 76]

Thermodynamic Barriers to Doping Quantum Dots

As pointed out in the section "Growth of CdSe Quantum Dots" above, thermodynamics play a crucial role in the nucleation and growth of quantum dots. The Gibbs-Thompson equation and energies determine whether or not a particle of a given radius will dissolve or continue to grow in solution. It should come as no surprise then that thermodynamics should play a role in whether or not a quantum dot is successfully doped. As mentioned before, doping involves the deliberate introduction of defects into the crystal lattice, which in turn effects the lattice formation energy (ΔF_v) and thus ΔG[73]:

$$\Delta G^* = 16\pi\gamma^3/3\Delta F_v^2$$

and yields the following result:

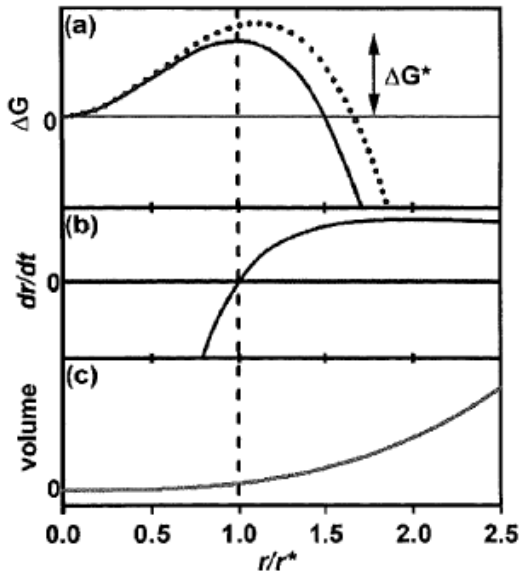

Figure 1-41 Effects of Doping on r* [73]

Bryan, Schwartz and Gamelin showed that introducing Co^{2+} dopant atoms into ZnO clusters caused a relaxation of the lattice and a reduction of the lattice formation energy (ΔF_v) and increasing the ΔG^* (dotted line in Figure 1-41a). The net result is that the ΔG^* required to allow a particle with radius r^* to continue to grow rather than dissolve is increased. The black

line in Figure 1-41 shows the ΔG maximum occurs at $r/r^* = 1$ for an undoped ZnO cluster. However, when the lattice relaxation caused by an impurity atom is taken into account (dotted line) the ΔG maximum occurs at $r/r^* \sim 1.1\text{-}1.2$. This increase in the r^* for a doped quantum dots indicates that doped crystallites are more soluble in the growth solution and nucleation is less likely to occur.

Furthermore, the ΔG for cobalt doped ZnO was found to be 5.75 kcal/mol higher than for pure ZnO. An Arrhenius plot indicates that this increase in energy reduces the nucleation rate by 10,000 times, making it highly unlikely to nucleate a quantum dot with the dopant atom at the exact center where theoretical modeling showed it has the most overlap with the quantum dot's band structure.[77]

Successful incorporation of dopant atoms into the host quantum dot is not the end of troubles. Dopant effectiveness is also an issue as a result of quantum confinement. The dopant defect energies (DX^- centers) must line up with the $1S_e$ energy level in the conduction band[74, 77].

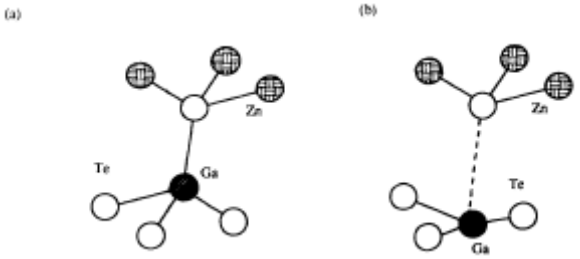

Figure 1-42 Origin of DX^- Centers in ZnTe:Ga[74]

When dopant atoms are incorporated into the host lattice the create distortions in the bonding of atoms, as seen in the case for ZnTe:Ga in Figure 1-42 where the tetrahedral sp^3 nature of ZnTe (a) is locally distorted to planar sp^2 at the gallium doptant center (b).[74] These DX^- centers determine whether or not a dopant is effective in a host material and why some materials can only be doped p-type or n-type but not the other.

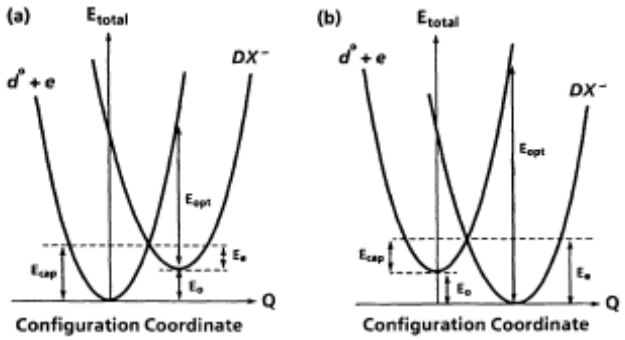

Figure 1-43 DX^- Band Alignments with Conduction Band Edge

The conduction band and DX^- band alignments for ZnSe and ZnTe are presented in Figure 1-43 (a) and (b) repectivly. In the case of ZnSe the DX^- band has a minimum that is higher in energy than the conduction band minimum. When the donor electron is ionized into the conduction band, a positive vacancy is left at the donor atom site and is able to capture an incoming electron; having the DX^- minimum above the conduction band minimum allows for efficient charge injection into the conduction band. Therefore ZnSe can be doped n-type while ZnTe cannot because the DX^- band minimum in ZnTe lies below the conduction band minimum as shown in Figure 1-43b.

Another factor governing dopant effectiveness in quantum dots is the phenomenon of "compensation" where the host lattice begins to form defects on its own that counteract the carrier introduced by the doptant atom.[78] In the case of an n-type doped semiconductor, at high levels of doping, the material will form defects that act as p-type acceptors to counteract the donor electrons. This lowers the donor energy (Ed) back towards a universal energy known as the Fermi Stabilization Energy (E_{FS}).

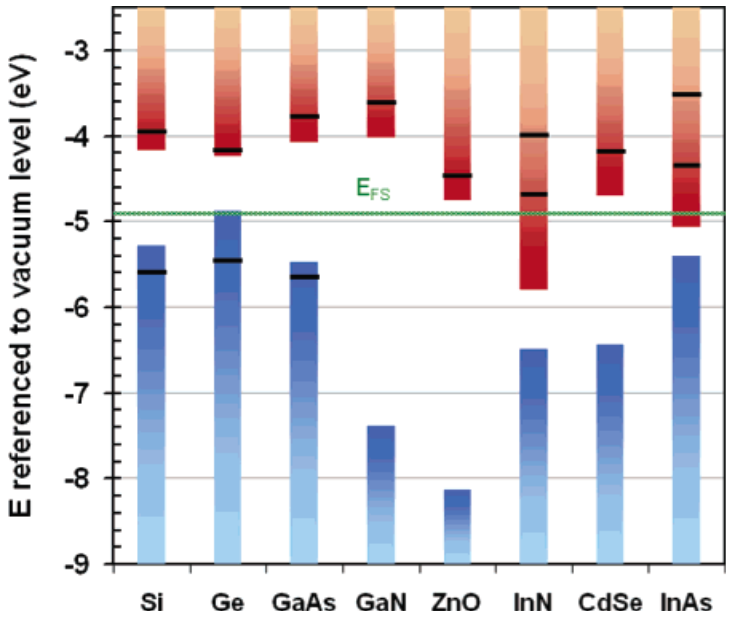

Figure 1-44 Fermi Stabilization Energy in Relation to Band Energies of Common Semiconductors[78]

The Fermi Stabilization energy (E_{FS}) at 4.9eV is shown in relation to several heavily researched semiconductors valence and conduction band edges in Figure 1-44. Khanal et al. point out that the closer a band edge is to the E_{FS} the more likely it is to be dopable to p-type in the case of the valence band or n-type in the case of the conduction band. Because the two bands do not shift equally upon quantum confinement, it may be even more difficult to dope a quantum dot for carrier conduction. Specifically, materials like CdSe, where the conduction band shifts much more than the valence band due to heavy-hole approximations, may be more difficult to dope n-type than their bulk phase because of the drastic increase in the energy of the conduction band edge. In this case, doping may increase compensation in the material due to a thermodynamic desire to return the donor level to the E_{FS}.

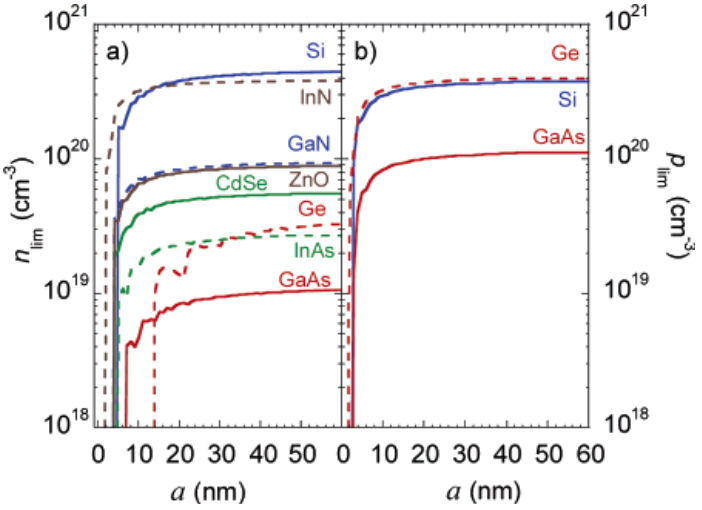

Figure 1-45 Donor (a) and Acceptor (b) limits in Nanowires as a Function of Width[78]

Khanal was also able to show that for many semiconductors the donor and acceptor limits are heavily suppressed in nanowires less that 20nm in diameter, as shown in Figure 1-45 (a) and (b)[78]. However, above 20nm in width, the donor and acceptor limits quickly approach those of the bulk material. This corroborates several reports of doping in both nanowires and quantum dots where the determined dopant content varies from the stoicheometry employed[75, 79].

Kinetic Barriers to Doping Quantum Dots

Some researchers have argued that because quantum dots are grown far away from thermodynamic equilibrium that kinetic factors must be considered when approaching the problems posed by the difficulties in doping quantum dots.[68, 75, 76] Much of the work done in this area focuses on surface morphology of the quantum dots and determining where the most favorable binding facets are located.

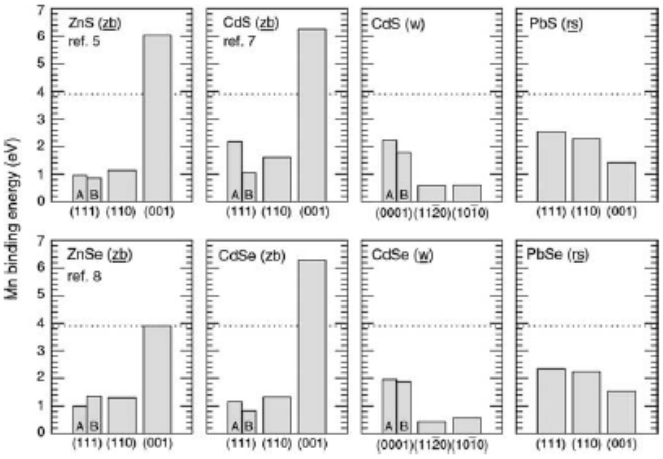

Figure 1-46 Binding Energies of Mn^{2+} to Crystal Facets of Various Quantum Dots[75]

Erwin et al. were able to show that the (001) crystal face of several II-VI quantum dots in the zinc blende had a higher binding affinity for Mn^{2+} than any of the wurtzite faces as shown in Figure 1-46[75]. Here all of the (001) faces show binding affinities approaching 6eV for ZnS, CdS, and CdSe while ZnSe has a (001) binding affinity of ~4eV. In contrast, the facets of wurtzite crystal of the same materials show binding affinities around 1eV. Du and colleagues claim that an activation energy of ~1.5eV is necessary to remove a dopant atom from the surface during growth.[76] Clearly, binding a Mn^{2+} dopant to the (001) surface of these materials is energetically favorable and should result in dopant incorporation.

However, in the section "Quantum Dot Growth" above, it was discussed that the vast majority of synthetic schemes generate CdSe quantum dots in the wurtzite crystal phase. Erwin was able to show that by synthesizing quantum dots in selenium rich conditions it was possible to grow zinc blende CdSe quantum dots that showed improved Mn^{2+} uptake via elemental analysis.[75]

To further understand the role of binding energies play in dopant uptake, Du et al. investigated the role of binding energies on nanorods/nanowires.[76] Peng showed that all nanorods/nanowires and tetrapods originate from a zinc blende magic-sized nanocluster and convert to elongated shapes with a wurtzite crystal structure due to surface ligands.[34]

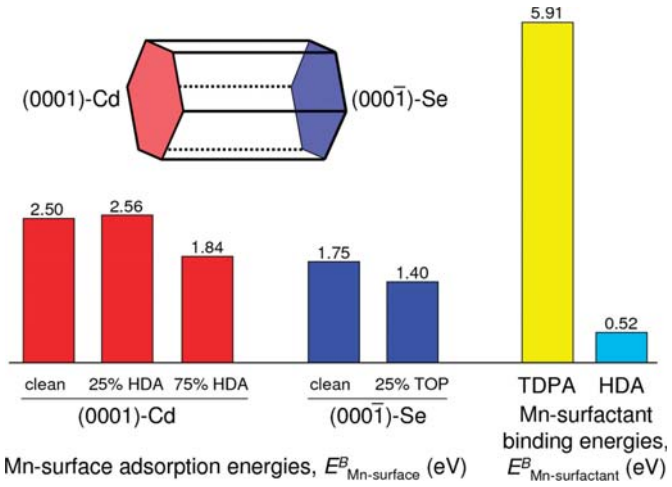

Figure 1-47 Mn^{2+} Binding Affinities for Various Facets of CdSe Nanowires[76]

The results of the above mentioned study are shown in Figure 1-47. In the case of nanowires, growth occurs solely along the (0001) axis of the wurtzite structure, which is highly anisotropic due to being cadmium terminated in one direction and selenium terminated in the opposite. Du et al.'s work shows that Mn^{2+} binds more favorable to the cadmium terminated (0001) face by a factor of as much as ~1eV.[76]

Du also calculated the binding energies of Mn^{2+} with tetradecylphosphonic acid and hexadecylamine, two ligands crucial to changing the zinc-blende magic-sized nanocluster seed into the elongated rod shape, also shown in Figure 1-47, and found a binding energy of almost 6eV for the phosphonic acid and ~0.5eV for the amine.[76] This calculation confirmed what several groups had suspected, that the organic acids commonly used in hot injection methods were binding too tightly to dopant atoms and preventing the dopant atoms from entering the quantum dots.[70, 71, 80]

Selfpurification of Quantum Dots

The preceding sections have outlined the difficulties of incorporating dopant atoms into quantum dots. Regardless of the strategy used to grow the doped quantum dots, the thermodynamic and kinetic barriers must be overcome. However, one hurdle remains; the process referred to as "self-purification," whereby the quantum dots expel dopant atoms that have cleared the thermodynamic and kinetic obstacles and incorporated into the nanocrystal.

Dalpian and Chelikowski point out that self-purification is not unique to quantum dots, all crystals will undergo self-purification; rather that self-purification is problematic to quantum

dots because of the shorter distances the dopant atom must diffuse through before reaching the surface of the quantum dots.[81] Dopant diffusion is a well known phenomenon in bulk semiconductors where it is known as transient dopant diffusion or TED.[66] As with the previous challenges to doping quantum dots, Dalpian and Chelikowski propose that self-purification is driven by thermodynamics, specifically the heat of formation for an impurity (in their case manganese).

$$\Delta H_f = E_T^{Mn} - E_T + (E_{Cd} + \mu_{Cd}) - (E_{Mn} + \mu_{Mn})$$

In the above equation ΔH_f is the heat of formation, E_T^{Mn} is the total energy of the doped quantum dot, E_T is the total energy of an undoped quantum dot, E_{Cd} and E_{Mn} are the elemental energies of cadmium and manganese respectively, and μ_{Cd} an μ_{Mn} are the chemical potentials of cadmium and manganese respectively. Therefore ΔH_f can be interpreted as the energy required to substitute a cadmium atom with a dopant atom. If the chemical potentials are ignored the expression simplifies into a relative value $\Delta H_f = E_T^{Mn} - E_T$.

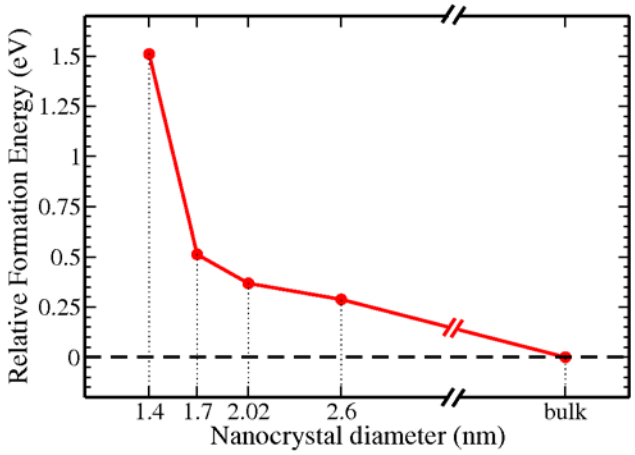

Figure 1-48 Relative ΔH_f of Manganese Dopant as a Function of Quantum Dot Size[81]

Dalpian and Chelikowski argue that because smaller quantum dots have larger E_T than larger crystals, the ΔH_f of doping is also size dependant, as shown in Figure 1-48 above.[81] Calculations on the Mn^{2+} energy levels in CdSe quantum dots (not shown) indicate that Mn^{2+} shows a strong valence band overlap at ~-2.5eV, and that under selenium rich conditions such as those used by Erwin et al.[75] , the chemical potential of cadmium is ~ -1.5eV which greatly lowers the ΔH_f for a manganese impurity atom.

Chelikowski goes on to argue that because the bond length for Mn-Se is only 0.001 A shorter than the Cd-Se bond, there is negligible surface relaxation in small quantum dots that

would lower ΔH_f.[82] Furthermore, Chelikowski points out that the 0.2 eV increase in E_T for a ~5 nm quantum dot, it is enough to reduce the equilibrium defect population by two orders of magnitude.[82]

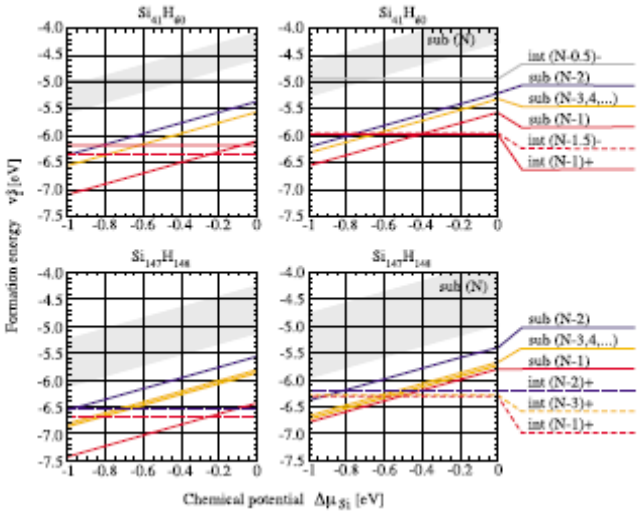

Figure 1-49 Interstitial and Substitution Heats of Formation in Si_{41} and Si_{147}[83]

Leitsmann, Küwen, and Bechstedt calculated the ΔH_f for interstitial (dotted lines) and substitution (solid lines) manganese (left) and iron (right) sites in hydrogen passivated Si_{41} (upper) and Si_{147} (lower) quantum dots shown in Figure 1-49 above.[83] They found that interstitial dopants are more stable than substitution dopants as evident from the flat formation energies represented by the dotted lines while substitution dopants increase in formation energy as chemical potential occurs. Also note that the Si_{147} quantum dots have lower dopant formation energies than the Si_{41} quantum dots, confirming Dalpian and Chelikowski's work discussed above.[81, 82] Similarly, at low silicon chemical potentials substitution dopants have lower formation energies, akin to Erwin et al's finding that anion rich conditions are favorable for cationic-substitution doping; and Lott et al. showed that indium doping of CdSe films is more successful when preformed under selenium vapor pressure.[84]

Quantum Dot Doping Strategies

Based on the energetic and kinetic difficulties of doping discussed above, it is clear that a well thought out strategy is needed for doping quantum dots. As Bryan et al. pointed out, the surface relaxation associated with a dopant atom at the exact center of a quantum dot acts as a barrier to

center-doped nucleation.[73] Pradhan proposes a different strategy based on separating nucleation doping and growth doping.[85]

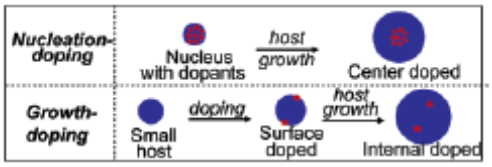

Figure 1-50 Nucleation Doping vs Growth Doping[85]

Nucleation and growth doping are shown in Figure 1-50 above.[85] In nucleation doping a small nucleus with the dopant atoms is created by tuning the chemical precursors so that at the time of injection both host and dopant precursors are active, but upon the rapid cooling the dopant precursor becomes inactive and the host material grows around the doped nucleus. This allows the dopant to participate in the supersaturation and nucleation event ensuring that the dopant's location in near the center of the quantum dot. By ensuring that only the host precursors are active after the rapid cooling, pure host material is able to grow around the nucleus of the quantum dot, keeping the dopant at the center where it has been proposed that there will be maximum overlap between the dopant atoms atomic orbitals and the quantum dot's energy states.[77]

Pradhan et al. argue that the Lewis acid model governs the selection of precursors.[85] In the case of manganese doped zinc selenide, the authors point out that Mn^{2+} is a harder Lewis acid than Zn^{2+} towards the same ligand such as sterate or acetate, and therefore should be less reactive. Upon injection, both the zinc and manganese complexes are active and supersaturate the solution, while after the cooling only the zinc complex is active. The result is a manganese doped nucleus of zinc selenide with pure zinc selenide grown over it.

Growth doping on the other hand, involves the nucleation of a pure host small quantum dot followed by the surface trapping of the dopant advocated by Erwin et al.[75] and Du et al.[76] followed by overgrowth of the host material. In this case the doping is random and uncontrollable; in that there is little control over the location or number of dopants incorporated into the quantum dots. Clearly, nucleation doping if preferable to random growth doping since precise control over the dopant atoms concentration and location are needed to optimize the performance of any device founded on doped quantum dots.

Carrier Doping CdSe

Having discussed the difficulties associated with doping quantum dots, the following section will highlight the few successful reports of carrier doping in CdSe nanostructures. Included in this section will be a short description of electrochemical "charging" as well, and its effects on the optical properties. Reports of doping quantum dots with transition metals will not be included, due both to numerous reports and studies discussed above investigating the difficulties associated with quantum dot doping.

Levy and co-workers were the first to report n-type CdSe thin films doped with indium.[86] In this case, the authors used pulsed laser ablation to grow thin films on a wafer substrate with powders of CdSe and In as source materials. The photoluminescence spectrum of one sample is shown below:

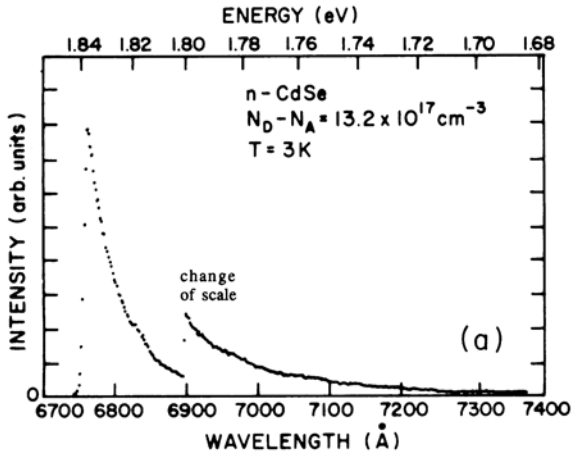

Figure 1-51 Photoluminescence of Heavily Indium Doped CdSe Thin Film[86]

In Figure 1-51 there are two peaks: one at ~6850 A indicating band-edge recombination and one at ~7080 Å indicating recombination with the donor level. The donor level recombination is so weak that an alteration of the vertical scale is required to see it (scale change occurs at 6900 Å). In both cases the emission from these levels appears as a weak shoulder compared to emission from higher energy recombination in the band continuum, due to weak confinement in only a single dimension.

Rouleau and Lowndes also used pulsed laser deposition to form indium doped CdSe films on GaAs.[87] Their work showed that thin films of CdSe doped with indium display a bimodal carrier concentration: films either have carrier concentrations greater than $3x10^{20}$ per cubic centimeter or below $4x10^{18}$ per cubic centimeter. Unfortunately, the authors claim that no experimental parameter was responsible for this.

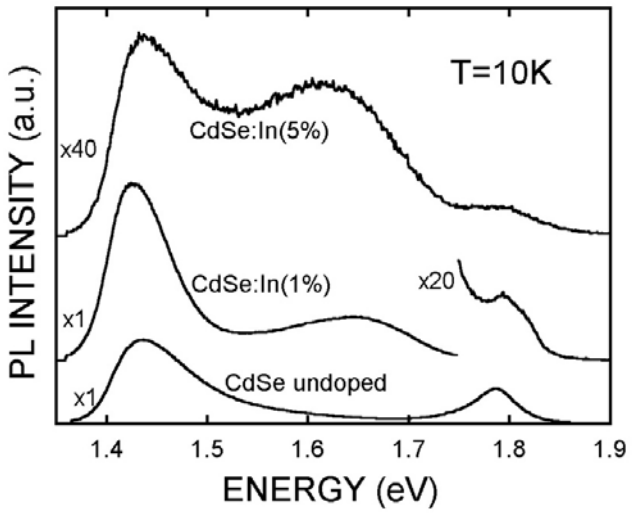

Figure 1-52 Fluorescence Spectra of Lightly Indium Doped Thin Films of CdSe[88]

Perna *et al* used XRD to show that phase separation into CdSe and $CdIn_2Se_4$ begins to form between 1% and 5% indium content in thin films.[88] The authors also report that low levels of indium doping alter the extinction coefficient (absorption cross section) near the band-edge region. Most importantly, Perna and co-workers showed that indium doping introduces a second fluorescence peak ~0.2 eV below the bulk band-edge emission peak (E_g of bulk CdSe at T = 5 K ~1.8 eV) as shown in Figure 1-52 above. The major emission feature to notice is the broad peak growing in between 1.6 and 1.7 eV as the amount of indium increases.

Lott investigated both indium[84] and gallium[89] doping of CdSe. In both cases the authors report that conductivity of doped CdSe films is weakly temperature dependant and that at 1% indium composition there is no phase separation.

He *et. al* were able to synthesize indium doped CdSe nanowires in a chemical vapor deposition (CVD) apparatus.[72] Indium doped nanowires showed improved conductivity in simple a source-drain circuit. The authors also showed that the conductivity improvements were related to the rate of indium evaporation during synthesis and annealing.

The Guyot-Sionnest group have several reports of electrochemical charging of CdSe quantum dots through electron injection from sodium biphenyl.[90, 91] In these reports, CdSe quantum dots were stirred in a heptamethylnonane solution with sodium biphenyl, which donates an electron to the quantum dots, effectively creating an n-type doped particle. The optical effects of this process are shown in Figure 1-53 below:[91]

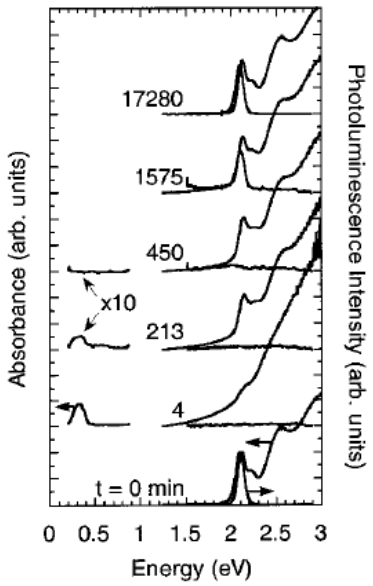

Figure 1-53 Sodium Biphenyl Charged CdSe Quantum Dots[91]

Charging quantum dots with sodium biphenyl leads to two distinct optical changes: first the sharp band edge absorption seen at ~2 eV in t = 0 minutes begins to disappear and second, a new absorption peak below 0.5 eV begging to grow in. At long time frames the donated electrons leave the particle leaving the 1S energy level open to excitation occupation and the band-edge absorbance and fluorescence return. This is due to the donated electrons from the biphenyl no longer occupying the 1S electron level. Work with CdSe/ZnS core shell particles and charging experiments indicate that in the 2 electron maximum (full occupation of the 1S level) an Auger relaxation pathway with a time constant of 100 ps is present.[92]

During the early stages of the work described in this dissertation a single report of indium doping of CdSe quantum dots was published by Knox *et. al*.[69] Indium doped quantum dots were synthesized by the hot injection method with $InCl_3$ used as the indium source. The report indicates that indium is lost during a pyridine ligand exchange of bare CdSe particles but not when a ZnS capping layer is added suggesting that most, if not all, the indium is located on the particle surface. This is used to explain why indium doped quantum dots have lower quantum

yields than undoped CdSe particles, but aside from lower quantum yields the electronic structure of the quantum dots remains unchanged.

Thesis

In the following chapters data will be presented to show that CdSe quantum dots have successfully been doped with indium, tin, and gallium. The data will also show that despite many of the challenges discussed above, successful doping was achieved with a simple modification to a pre-existing synthetic scheme and that the presence of dopant atoms greatly alters the growth kinetics of quantum dots. Soft-neutron absorption decay and energy dispersive x-ray spectroscopy will show that dopant atoms are incorporated into the quantum dots.

The data will also show that doping does in fact have a dramatic effect on the electronic properties of quantum dots. Temperature dependent photoluminescence (TD-PL) will show that fluorescence quenching is related to the dopant's energetic location relative to the conduction band. TD-PL will also show that gallium is more easily ionized into the conduction band energy levels than tin, which is in turn more accessable than indium. Simple current vs. potential measurements (I-V curves) will show that thin films of indium and tin doped quantum dots have higher conductivity than thin films of undoped quantum dots. Higher conductivity translates into higher current densities. Indium doping also induces a light response to the quantum dots, yielding higher current under overhead light illumination than in the dark. Finally, Transient Absorption spectroscopy will show that indium doping introduces a ~80 meV blue shift in the 1S absorption feature bleach, indicating a new electron energy level has been introduced by the dopant atom.

Doping quantum dots to introduce n-type donor levels into the electronic structure has profound effects on the properties of CdSe quantum dots. These changes show that doping quantum dots will become a powerful tool to customizing the electronic properties of quantum dots, and make doped quantum dots ideal platforms for a new generation of electronic devices.

Chapter 2 - Initial Efforts to Dope CdSe Quantum Dots with Indium

Introduction

In recent years semiconducting nanocrystals, or "quantum dots," have gained attention due to their size dependant properties.[4] CdSe has received the lion's share of interest because the bandgaps of CdSe quantum dots span the visible spectrum, making them ideal for applications such as bio-medical tagging, [7] and photosensitizes.[59] The ability to readily synthesize batches of quantum dots with narrow size distributions[18] coupled with the ability to control the shape of the nanocrystals[23] makes CdSe nanostructures ideal platforms for a new generation of electronic devices.

Like many other semiconductors CdSe suffers from poor intrinsic conductivity and will require doping to achieve maximum effectiveness in device construction. Doping CdSe thin films with elements such as indium[84, 86]and gallium[89] has proved to increase conductivity. Indium doping has also been reported in CdSe nanowires.[72] However doping to increase the conductivity of CdSe quantum dots has not been extensively explored; while many reports exist for doping to introduce magnetic properties.[75, 80, 85] This is partly due to the general difficulties predicted in doping quantum dots[68, 73] and the fact that similar results can be achieved through electrochemical reduction of quantum dots with sodium biphenyl in a process known as charging.[90]

The self-purification mechanism in quantum dots, where defect atoms are thermodynamically driven out of the nanocrystal or to the surface poses another challenge to successful doping.[82] The valence orbital of dopant atoms on the surface of the quantum dots do not overlap well with the band structure of the host lattice which hinders carrier donation.[77] Therefore it is highly desirable to introduce dopant atoms in or as near to the nucleus of a quantum dots during growth. This is a process termed "nucleation doping" by Peng and co-workers.[85] Nucleation doping has been successful in introducing magnetic dopants into CdSe quantum dots.[75, 79] In this process the dopant precursor is present at the time of the nucleation

injection of Cd/Se precursors into the hot co-ordinating solvent. After the quantum dot nuclei form with the dopant inside, a "pure" phase of CdSe grows around the doped nucleus.

The goal of this initial work is to synthesize indum doped CdSe quantum dots via the hot injection method and explore the changes in photoluminescent properties of the doped quantum dots. Hot injection is the most common, established, and acceptable method for making high quality quantum dots. Therefore indium doped CdSe quantum dots produced by this method should be considered free of defects aside from the dopant atoms; and any and all changed in the properties of these nanocrystals could be explained by the presence of indium.

The addition of $In(CH_3)_3$ dissolved in tri-octylphosphine shortly after the injection of TOP:Se into a solution of TOPO and HPA-Cd produces several novel features to CdSe quantum dots. First, a large Stokes Shift is introduced to the photoluminescence spectrum of the quantum dots. Second, the emission profile of the quantum dots ensemble broadens significantly due to the introduction of new electronic states. Last, the fluorescence profile of indium doped quantum dots changes significantly during pyridine ligand exchange with a blue shift in the PL peak position and the emergence of a shoulder on the red side of the spectrum.

Experimental

Chemicals: Tri-n-octylphosphine (TOP) and tri-n-octylphosphine oxide (TOPO) are distilled at ~2 torr. TOP was stored in a glovebox under inert atmosphere. A 1M stock solution of TOP:Se is made by stirring appropriate amounts of selenium powder in the distilled TOP. $In(CH_3)_3$ in TOP is mixed fresh before synthesis. CdO and hexylphosphonic acid (HPA) are stored in a glovebox and used as is. Anhydrous methanol, toluene, and pyridine were used as purchased.
Procedure: A three neck flask equipped with a temperature probe and injection arm is loaded with 0.1284 g 1(mmol of CdO) and 0.84 g of HPA in a glovebox and brought out into the lab. After 10 minutes under Ar flow the HPA/CdO mixture is gently heated to 300 °C and stirred until the CdO dissolved. The Cd-HPA complex is cooled to room temperature and aged overnight under Ar flow. The following day 17 g of distilled TOPO is added and the solution is heated to 200 °C for 2 hours to drive off oxygen and water. The temperature is increased to 280 °C and 1 mL of TOP:Se diluted with13.3 mL of TOP is rapidly injected. Immediately following the TOP:Se injection a 5 mL solution of $In(CH_3)_3$ The quantum dots are allowed to grow until *in situ* absorbance spectroscopy indicates the quantum dots have a first-excitonic transition at 560

nm. The reaction is cooled to 80 °C and the quantum dots are precipitated by the addition of 20 mL of anhydrous methanol. The precipitated solution is centrifuged and the resulting solid id resuspended with anhydrous toluene. Purification is repeated two more times.

The pyridine ligand exchange is preformed by suspending the purified CdSe quantum dots in ~50 mL of anhydrous pyridine and refluxing the resulting solution under Ar flow. Aliquots of the CdSe in pyridine solution are taken out at specified time intervals. The absorbance and photoluminescence of the ligand exchanged quantum dots is recorded immediately.

Results and Discussion

The procedure described above quickly and easily produced batches of quantum dots that remained stable for several months after purification. Two batches of CdSe quantum dots were studied in depth; one where 10 mol % of Indium with respect to the cadmium content injected according to the experimental section and one where 5 mL of distilled TOP was added without $In(CH_3)_3$ after the TOP:Se injection. This second batch without the indium in the TOP was made as a check against the additional TOP altering the properties of the particles in growth.

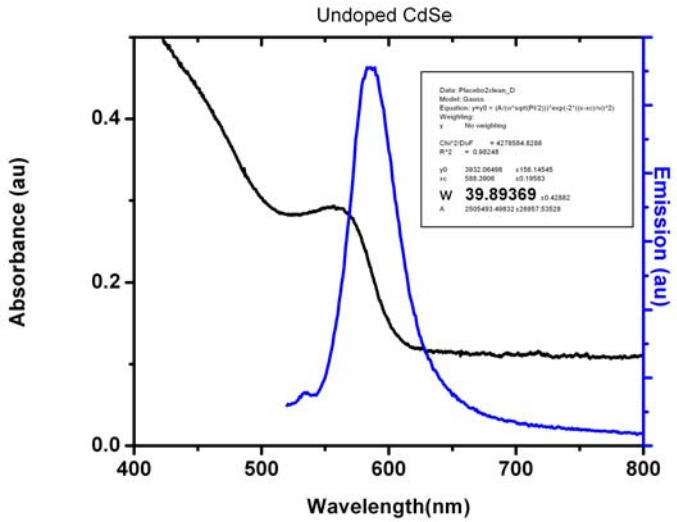

Figure 2-1 CdSe Quantum Dots Growth via Hot Injection Method

The absorption and photoluminescence of the normal CdSe quantum dots are presented in Figure 2-1 above. The absorbance peak (black line in Figure 2-1) is located at ~540 nm indicating a mean particle radius of 3.2 nm according to effective band edge calculations.[4] The good peak-to-valley ratio of the absorption peak indicates a narrow size distribution. The

photoluminescence peak (blue line) is located at 555 nm and has a FWHM of ~40 nm according to Gaussian fitting indicating a narrow distribution of emitting states. Some trap emission can be seen in the 650-800 nm range, however the dominant feature of the PL spectrum is the band-edge emission. The addition of indium as a dopant leads to several changes in the spectral features.

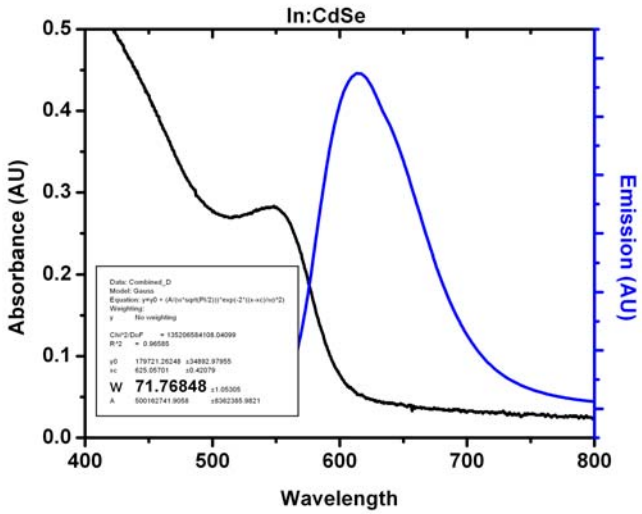

Figure 2-2 Indium Doped CdSe Quantum Dots Grown by Hot Injection Method

Absorbance and photoluminescence spectra of 10 mol % indium doped CdSe quantum dots are shown in Figure 2-2. Quantum dots doped with indium display a 1S absorbance peak at 545 nm. Like the normal CdSe quantum dots in Figure 2-1 these quantum dots also have a distinct peak-to-valley ration indicating a narrow size distribution. Photoluminescence spectra show a peak at 601 nm with a FWHM of 72 nm. The photoluminescence spectrum of indium doped quantum dots is significantly different from undoped quantum dots in two regards.

First, the photoluminescence peak of indium doped quantum dots is much further red-shifted than undoped dots. The undoped sample shows a 15 nm difference between the absorbance and photoluminescence maximum (Stokes Shift). In the indium doped sample this shift is 56 nm. This large Stokes Shift indicates significant relaxation of the exciton to a lower energy state than in the undoped quantum dots which show Stokes Shifts comparable to literature.[6, 28, 93]

Second, indium doped quantum dots PL peak has a much larger FWHM than undoped quantum dots. Undoped quantum dots PL spectrum has a FWHM of ~40 nm while the indium

doped quantum dots have a FWHM of ~72 nm. This indicates a wider distribution of emitting states caused. However because both the undoped and indium doped products have similar sizes (~3.2 nm) this wider distribution of emitting states cannot be explained simply by size distributions alone.

As discussed in the introductory chapter, the photoluminescence of quantum dots is strongly tied to the condition of the particle surface. Therefore it is most likely that the indium dopant atoms are located on or just below the surface layer of the quantum dots. Several reports in the literature show that refluxing quantum dots in pyridine will remove surface defects as well as remove surface atoms from the particles.[19, 80] In order to confirm that the changes in the photoluminescence spectrum is due to successful dopant incorporation, a samples of the indium doped quantum dots and normal quantum dots are refluxed over night in pyridine with samples taken out at intervals.

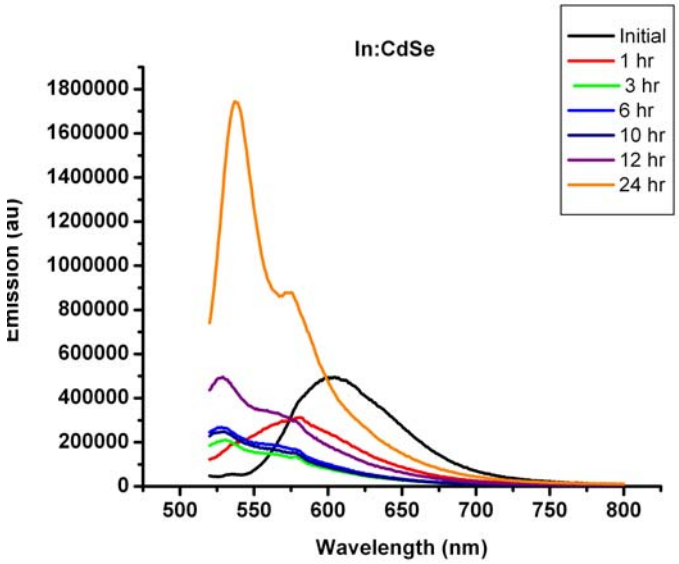

Figure 2-3 Indium Doped Quantum Dots Undergoing Pyridine Surface Exchange

The photoluminescence spectra of indium doped quantum dots undergoing pyridine ligand exchange is displayed in Figure 2-3 above. The exchange process occurs over 24 hours while the particles are refluxed in anhydrous pyridine. The initial spectrum is shown in black above. After one hour of reflux, the peak position has blue shifted from 601 nm back to 575 nm. Further ligand exchange results in the slow emergence of a dominant peak at 540 nm with a shoulder at 565 nm. The absorption peak remains fixed at 540 nm, however after 24 hours of reflux time, it had broadened out indicating the size distribution is not as narrow as before.

However, the fact that the peak remains fixed at 540 nm indicates that Ostwald Ripening has not begun and therefore the peak at 565 nm is not due to a slightly larger size of quantum dot.

When undoped quantum dots are subjected to the same procedure the changes in fluorescence is much less compelling; the band-edge emission increase in intensity over 24 hours (not shown). Therefore it can be concluded that the changes observed in the indium doped sample is due entirely to the presence of indium on or near the particle surface. As the pyridine ligand exchange progresses and some of the surface atoms are removed the dopant induced emission at 601 nm disappears and is replaced by the peak at 575 nm and finally the peak-shoulder structure in Figure 2-3.

This progression of changes in the photoluminescence indicates that the surface bound indium atoms are removed within the first hour of reflux followed by any indium atoms just below the surface. After sufficient ligand exchange and surface atom removal only indium atoms deep in the core of the quantum dot are left and manifest as the shoulder at 565 nm while the band-edge emission emerges.

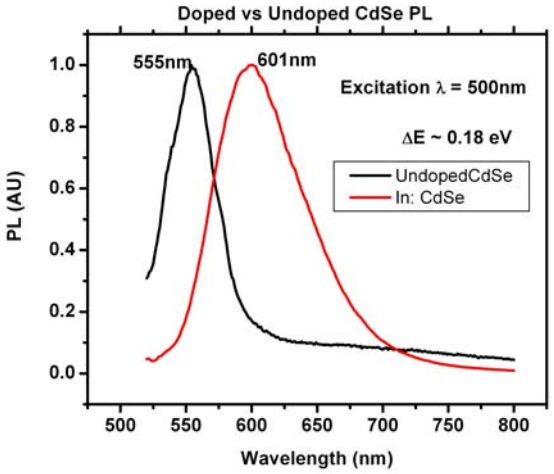

Figure 2-4 Energy Difference Between Indium Doped and Undoped CdSe Quantum Dot Photoluminescence Peaks

Figure 2-4 shows the calculated energy difference between the fluorescence peaks of the doped and undoped quantum dots before reflux. The difference in energies of the two peak positions is calculated to be 0.18 eV. This value is on par with the 0.2 eV reported by Levy for "heavily" doped CdSe thin film doped with indium. This corroboration of results indicates that when indium dopant atoms are located at the surface they create a surface defect that reduces the

energy of an exciton upon collision by an amount comparable to values reported in the literature. However, as the surface defect states are removed the emission blue shifts because energy is no longer being lost to collisions with the dopant atom.

Conclusion

CdSe quantum dots are successfully doped with indium. The incorporation of indium into the quantum dots results dramatic changes in the fluorescence characteristics of the doped quantum dots. Indium atoms on the surface of the quantum dots result in a Stokes Shift roughly four to five times larger than the Stokes Shift for normal CdSe quantum dots. Indium atoms on the surface also cause the fluorescence spectrum to broaden out by 50%, indicating a larger variation of emitting sates. Pyridine ligand exchange results in a loss of these surface states and the fluorescence spectrum blue shifts to a spectrum dominated by band-edge emission with a shoulder from indium atoms deep in the particle core.

The results described above are difficult to reproduce. Subsequent batches of indium doped dots did not display the three main characteristics discussed in this chapter; for example particles would display a larger Stokes shift but a narrow FWHM and did not display the same behavior under pyridine ligand exchange. Calculations by the Efros group have shown that the hexylphosphonic acid binds very strongly to manganese and does not allow it to be incorporated into CdSe quantum dots very efficiently.[76] The synthetic method used here contains a 6:1 ratio of phosphonic acid to cadmium which leaves excess phosphonic acid molecules to bind to the indium precursor as it is added.

In one experiment to determine if the phosphonic acid is interfering with doping, a flask ia loaded with hexylphosphonic acid and TOPO, heated as described in the Experimental section and the TOP:Se solution is injected followed by the TOP/$In(CH_3)_3$ solution in an effort to nucleate InSe quantum dots which should have bandgaps in the visible range. The initial addition of indium did not induce nucleation, indicating that the indium is strongly bound to the phosphonic acid. Indium selenide is nucleated after three subsequent injections. As a control, a second flask is loaded with TOPO, heated, and the TOP:Se is injected followed by addition of the TOP/$In(CH_3)_3$. This immediately resulted in a yellow solution. This series of experiments confirmed the suspicion that phosphonic acids tightly bind to indium and inhibits incorporation into quantum dots.

Several different synthetic systems are tested in an attempt to reproduce these results including steric acid-cadmium complex, oleic acid-cadmium complex, and the cadmium-mystrate complex that yields zinc blende quantum dots. In all cases, it appears that any organic acid binds tightly to the indium and inhibits doping. Clearly it is necessary to develop a synthetic system that does not include an organic acid moiety if CdSe quantum dots are going to be successfully doped with electron donating atoms.

Chapter 3 - Heterogeneous Growth of Indium Doped CdSe Quantum Dots

Introduction

Semiconductor nanocrystals have garnered significant attention due to their size dependant optical properties,[18] shape control,[23, 37] and the formation of core/shell particles.[17, 19] Due to their wide absorption cross-sections and narrow emission bands, CdSe quantum dots (QDs) have attracted interest in fields of photosensitizers[59] and biomedical imaging.[7]

Traditionally, the optical and electronic properties of CdSe QDs are controlled by the size of the particle. Doping provides an alternative route to controlling the electronic properties of quantum dots without changing the size and has begun to attract attention[94]. Doping can be achieved in two ways: electrochemical or by incorporation of impurity atoms. Electrochemical doping, or charging, has already been reported[91] while doping in the form of introducing impurity atoms was predicted as difficult[68] due to the phenomenon of self purification.[81] Most reported results of doping in CdSe QDs have been restricted to the incorporation of transition metals in the 2+ state[95, 96] that replace Cd^{2+} and seek to exploit the magnetic properties of the dopant atom's unpaired electrons. Few reports exist concerning the doping of CdSe quantum dots to form shallow, hydrogen-like, acceptor or donor levels (n-type and p-type conduction respectively). Indium is routinely used in n-type doping of bulk CdSe[86] and in CdSe thin films.[88] Indium is ideal for doping CdSe because the atomic radii of Cd and In are equal, reducing lattice strain when In^{3+} replaces Cd^{2+}. Encouraged by reports of successful incorporation of Mg^{2+} into CdSe QDs using $MgCl_2$ and the $Li_4[Cd_{10}Se_4(SPh)_{16}]$,[80] we began to explore the effects of $InCl_3$ on CdSe QDs grown with this single source precursor method.[28]

Quantum dots containing acceptor and donor levels can be used to create quantum confined p-n junctions capable of improved charge carrier separation over bulk semiconductors. These quantum p-n junctions can lead to improved efficiency in solar cells, serve as a "bottom-up" platform for microchip technology, and increase sensitivity of photo detectors. CdSe has become a benchmark system of study in the quantum confined size region, and therefore is an

ideal system to develop not only a quantum p-n junction, but also to be a general model of how doping effects quantum dots.

Although many studies focused on the preparation of doped QDs, much less efforts have been committed to explore the role of dopant atoms on the growth kinetics. This work has three important contributions, which clarify this role. First, a heterogeneous growth regime of the CdSe QDs is reported here, which significantly differs from the usual focusing-defocusing regime of the nanoparticle growth.[31] During the early growth stages, the presence of two very different sized CdSe nanoparticles is observed. Second, *in situ* fluorescence spectroscopy is described and demonstrated as a practical tool to study the growth kinetics as well as the defects of the semiconductor QDs during growth. Third, it is shown that, the various forms of the dopant precursor affect the success of doping as well as the nanoparticle growth kinetics. In addition, the effect of the dopant on the growth kinetics can be different at different temperatures as demonstrated by the experimental data.

Experimental Section

Chemicals: Selenium powder, acetonitrile, methanol, toluene, thiophenol, triethylamine, $InCl_3$, $Cd(NO_3)_2 \bullet 4H_20$, $Li(NO_3)$, diethylzinc, $S(TMSi)_2$ and $In(CH_3)_3$ were used as purchased. Hexadecylamine (HDA) and trioctylphosphine (TOP) were distilled under vacuum with the second fraction collected and stored in a glove-box under N_2 atmosphere in the case of TOP, while HDA was stored on the shelf. The $Li_4[Cd_{10}Se_4(SPh)_{16}]$ precursor molecule was prepared by the method described by Cumberland *et al*.[28]

Synthesis of CdSe Quantum Dots: The method used to synthesize In doped CdSe QDs is similar to the method described by Magana *et al.*[80] Briefly, 0.02 g (0.1 mmol) of $InCl_3$ is loaded into the flask shown in Figure 1 along with a magnetic stir bar in the glove-box. 25 g of HDA is added, followed by 0.3g (1mmol) of the $Li_4[Cd_{10}Se_4(SPh)_{16}]$ precursor molecule. Under Ar flow the flask is gently heated until all of the HDA had melted (~40-50 °C). At this point, the *in situ* absorbance and photoluminescence equipment discussed below are set up for recording and the setup is covered in tin-foil to reduce heat loss. The temperature is increased to 120 °C and the reaction is stirred overnight under Ar flow. For the experiments where trimethylindium is used as the doping agent, the appropriate amount of trimethylindium is dissolved in ~3 mL of TOP and injected once the HDA had melted and the temperature is set to 150 °C to ensure decomposition

of the complex and left overnight. Approximately 16-18 hrs later, the temperature is increased to 240 °C for 3 hours to allow further growth. Afterwards, the temperature is increased to 250 °C and 4 mL of a Zn/S/TOP stock solution containing 7.5 mL of diethylzinc and 0.75 mL of hexamethyldisilithane diluted in 30 mL of distilled TOP is added over five minutes and the reaction is left at 250 °C for an hour to allow for shell growth. Upon cooling the crude material is centrifuged to remove metallic zinc. Further purification is achieved by precipitation of (CdSe)ZnS particles with MeOH followed by further centrifugation. The supernatant is discarded and the QDs dispersed in toluene. A final precipitation with methanol followed by centrifugation and dispersion in toluene completed the purification process.

***In Situ* Monitoring of Absorbance and Photoluminescence:** Figure 1 shows the flask and equipment used for the *in situ* monitoring of the absorbance and the photoluminescence of the quantum dots. The experimental details of the *in situ* absorption spectroscopy used in the experiments are previously described.[38] Briefly, a 1 mm path length cuvette is attached to the reaction vessel. The hot solution is continuously flows through the cuvette, which allows monitoring the absorbance of the growth solution. The pathlength of the cuvette is optimized to ensure optimum mixing in the cuvette and to achieve the desired optical density. A fiber optic absorption spectrometer is used to obtain the absorbance spectra. A separate fiber optic fluorescence spectrometer is utilized to acquire the photoluminescence spectra of the reaction mixture. A fluorescence Raman probe equipped with a 395 nm excitation wavelength LED is used to collect photoluminescence. The photoluminescence probe is situated as close to the reaction flask as possible and positioned so as to maximize the amount of signal collected. The amount of the fluorescence collected from the reaction flask has varied from reaction to reaction as well as the positioning of the Raman probe. However, the relative changes of the fluorescence during growth have remained constant. The back reflected excitation source intensity allowed for monitoring of the stability of the fluorescence setup, which remained constant throughout the experiment.

Results and Discussions:

***In Situ* Observation of Photoluminescence:** The experimental setup used to monitor the photoluminescence spectrum during growth if shown in Figure 3-1. The setup is identical to the one reported previously[38] with the addition of a surface Raman probe (D). The surface Raman

probe is equipped with a LED with emission centered at 395nm. The probe is adjusted to allow for maximum collection of the excitation light with the narrowest peak.

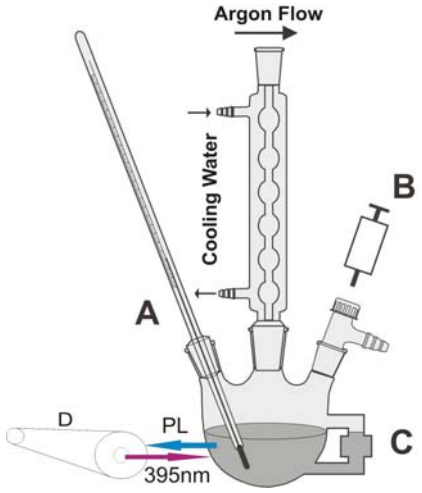

Figure 3-1 In Situ Photoluminescence Set-Up[70]

Heterogeneous Growth of CdSe Quantum Dots: Figure 3-2 shows the evolution of photoluminescence with respect to time during the growth phase of the synthesis of CdSe quantum dots. Figure 3-2a is the temperature profile while Figure 3-2b is the compiled photoluminescence spectra over the growth phase. As the temperature is slowly raised to 120 °C the $Li_4[Cd_{10}Se_4(SPh)_{16}]$ cluster decomposes and a single peak develops and shifts to the red until reaching 450nm. After a short time, a second peak begins to grow out of the first and shifts further to the red. The arrows correspond to (1) the emergence of the first peak, (2) the maximum fluorescence of the 1st peak, (3) the emergence of the second peak, (4) the second peak's maximum fluorescence. Arrow 5 denotes the photoluminescence peak position after 3 hours of growth at 240 °C. During this growth, the photoluminescence is greatly reduced, and reappears upon cooling to lower temperatures. When the solution is heated, the photoluminescence is quenched due to both the accelerated formation of structural and surface defects in the nanoparticles and increased phonon population at higher temperature. Arrow 6 denotes the emission peak position during the growth of the ZnS shell material. During the growth of the ZnS shell, a red shift is observed in the emission spectrum of the CdSe core and the intensity of the emission begins to increase.

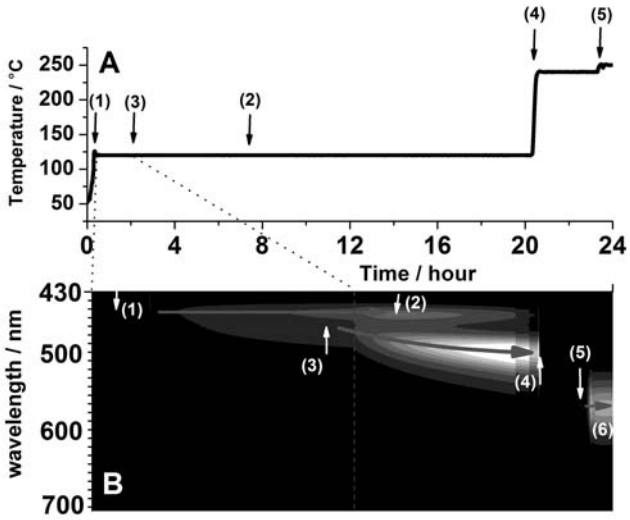

Figure 3-2 Temperature Profile and Fluorescence Spectum in the Heterogeneous Growth Regime[70]

As the reaction progresses the second peak becomes more intense than the first. After several hours, the maximum intensity at 460 nm is reached, at which point emission begins to decrease. While the emission centered at 460 nm begins to diminish, the emission from the second peak begins to steadily increase. This suggests that the smaller "magic size" family of QDs is consumed, facilitating the growth of larger particles. This differs from 'traditional' Ostwald ripening in two ways: (1) the growth is not continuous from one size to the next, there is only the peak at 450nm and then the second peak around 500nm and nothing in between; and (2) the final purified photoluminescence spectra show a non-Gaussian size distribution as shown in Figure 3a. Ostwald ripening occurs during colloid growth when the concentration of monomers drops below the supersaturation limit. Without substantial monomer concentration, smaller colloids decompose in order to provide monomers that enable the larger particles in solution to grow. When Ostwald ripening does occur, there is a continuous growth of the colloid sample, the absorbance and photoluminescence peaks shift smoothly to the red end of the spectrum. In the case of heterogeneous growth as described here, there is no smooth shift from blue to red, rather there is a gap between the two groups of particles. Inside this "growth gap" there is no evidence for the existence of any particles. Simply put, no QD sizes can exist in significant concentration between the group at 460nm and the group at ~500 nm under these growth conditions. While Ostwald ripening widens the size distribution of the QD ensemble, the distribution remains a smooth Gaussian distribution.

The absorbance and emission spectra of the magic size nanocluster observed in these experiments is represented in Figure 3-3. Two significant observations can be made from Figure 3-3: (1) the magic size nanocluster's (MSNC) emission spectrum is asymmetrical and (2) the magic size cluster exhibits surface trap emission in the range of 500-600nm. The tailing of the emission spectrum towards the red is generally considered more characteristic of molecular fluorophors than quantum dots.

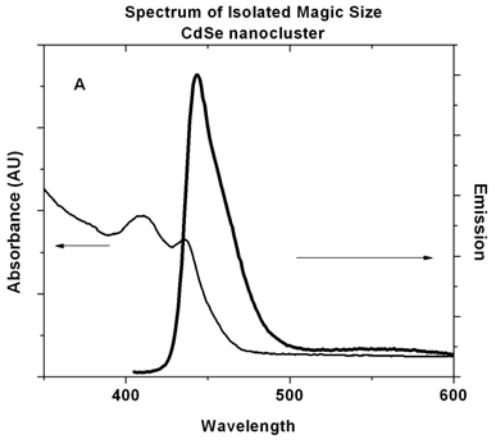

Figure 3-3 Fluorescence of Magic Sized Nanocluster[70]

In an effort to better understand the formation of the MSNC, matrix assisted laser desorption ionization time of flight (MALDI-TOF) mass spectrometry was preformed on purified solution of the MSNC. As seen in Figure 3-3 there are two peaks shown in the blown up inset where the first corresponds to $(CdSe)_{25}$ at 4784 mass units and a second and more intense peak at 4800 mass units. The broad peak encompassing both the 4784 and 4800 m/z peaks is present to represent the isotope distributon. Using the established densities for both wurtzite and zinc blende crystal structures and idealizing the nanocluster as a perfect sphere, a radius of 0.49 nm is obtained for wurtzite and 0.495 nm for zinc blende. It can therefore be concluded that regardless of crystal structure the magic size cluster reported here has a diameter of ~1nm. The absorption peak position of 435 nm corresponds to particles larger than 1nm in diameter, so this $(CdSe)_{25}$ particle is not likely to be the magic sized nanocluster observed during our synthesis. It is possible that this particle size is the result of fragmentation of larger particles caused by the laser.

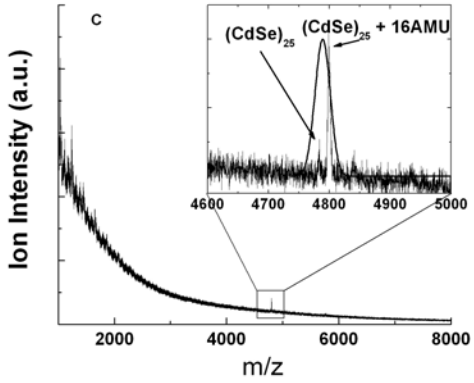

Figure 3-4 MALDI-TOF Mass Spectrum of $(CdSe)_{25}$ Nanocluster[70]

We propose that the more intense peak at 4800 mass units is the 1nm $(CdSe)_{25}$ cluster with an oxygen ion coordinated to its surface. At this time it is not possible to determine if the oxygen is present in the synthetic system or is a result of exposure to oxygen during purification and during the MALDI experiment.

Magic sized nanoclusters are generally explained by two phenomenon. The first a closed-shell structure[22] where the surface atoms obtain a closed valence shell structure. This generally occurs in the zinc blende crystal structure because of the tetrahedral bonding scheme.[22] In this state, the dangling bonds of the surface atoms are either minimized or absent. The second explanation for MSNC is the formation of a minimum on the overall Gibbs-Thompson energy of the particles.[97, 98] With the overall energy minimized, the particles cease to grow and the size distribution is focused to the magic size in order to lower the energy of the collective system. In the case of heterogeneous growth, a magic size cluster is obtained but due to the high monomer concentration additional monomers are added to the surface - most likely at high energy surface sites such as corners and edges. This addition breaks the closed shell configuration and the particles grow to the next most stable size under the reaction conditions. Interestingly, this event only takes place at the early stage of the growth. In the case presented, the 450 nm size represents the first closed shell configuration to which an additional monomer unit is added. Upon losing the closed shell and the stability that accompanies it, the particle behaves as a 'normal' particle and continues to grow until monomers are unavailable. The size distribution of the magic sized nanoparticle at 450 nm can be estimated from the FWHM of the emission peak. Both high temperature photoluminescence data and the emission from purified samples show

approximately 80 meV FWHM, which agrees well with the best observed emission peak width in literature.[99]

Effects of Indium Chloride on Growth: Varying the concentration of indium chloride in the solution changes the heterogeneous growth kinetics observed in the experiments where no indium chloride is added. Figure 3-5 shows the compiled emission spectra of experiments with (a) 5 mol% (b) 10 mol% and (c) 15 mol % indium chloride with respect to the number of moles of cadmium. The first change produced by the addition of the doping agent is that the time to reach the 1st peak's maximum emission decreases as the amount of indium increases (15%>10%>5%). In Figure 3-5 it can also be seen that the second family of particles emerges faster with increasing indium concentration. The second peak emerges at earlier times in the 10 mol % and 15 mol % maps than in the 5 mol % map.

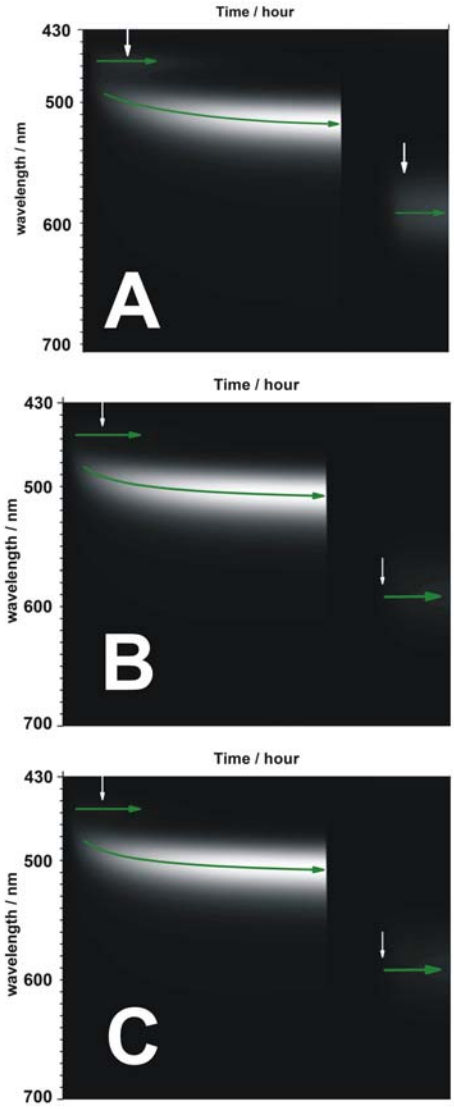

Figure 3-5 Heterogeneous Regime Fluorescence Plots of 5 (A), 10 (B), and 15 (C) mol % Indium Doped CdSe[70]

There are two possible explanations for this phenomenon: (a) the presence of indium chloride in solution activates the CdSe monomers or (b) the indium chloride activates the quantum dots' surface. With respect to (b), it can be argued that when an atom of indium or chlorine bonds to the surface of the particle, the surface energy is increased making the surface more susceptible to growth. The second difference the addition of $InCl_3$ produces is that the 1st peak is eventually consumed at the benefit of the second peak, indicating that adding indium chloride activates Ostwald ripening at early stages of growth. This will be discussed below. Thirdly, when the ZnS shell is added and indium chloride is present the photoluminescence maximum is reached quicker. The role of the ZnS shell is to passivate the CdSe core. As the

amount of time to reach maximum emissivity decreases, it can be concluded that the ZnS shell reaches its maximum effect quicker. An explanation for this is that a fundamental change in the particle core has occurred as a result of the indium chloride and no further improvements to the particle's emission are obtained by surface passivation. No correlation between the amount of indium added and the growth rate of the ZnS shell is observed and the previous observation cannot be explained by the passivating material growing faster. The data show that as the amount of indium increases the emission of the ensemble of quantum dots is decreasing; further data on quantum yields and amount of indium detected by nuclear activation analysis will be presented below.

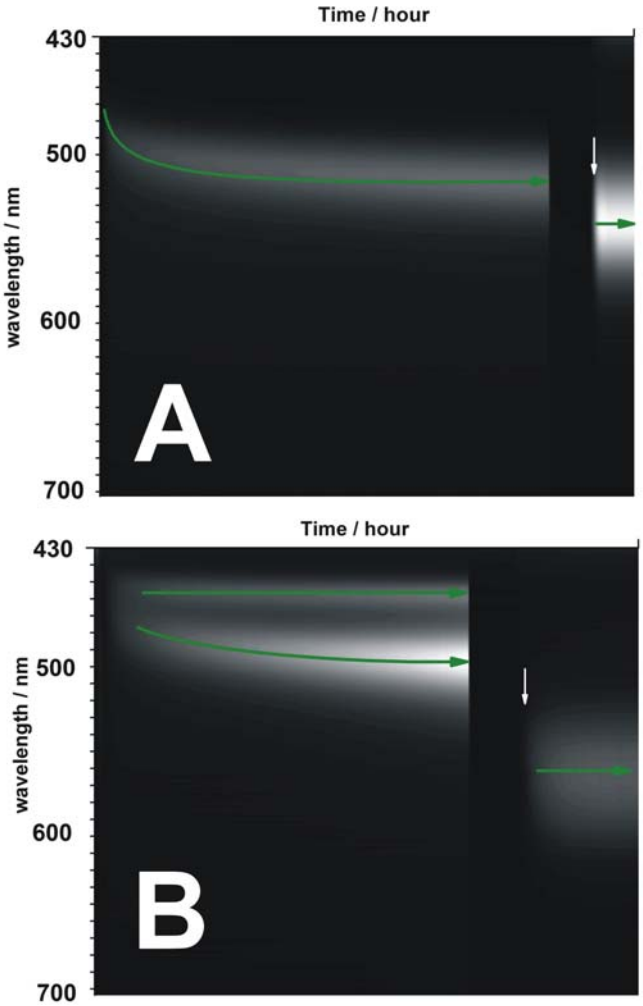

Figure 3-6 Heterogeneous Growth Regime Fluorescence Plots for Quantum Dots Grown With $In(CH_3)_3$ (A) and NaCl (B)[70]

The experiments represented in Figure 6 are designed to determine if the changes shown in Figure 3-6 are caused by indium (a) or chlorine (b). In Figure 4a 10 mol% of $In(CH_3)_3$ is used as a source of indium. The effects of using $In(CH_3)_3$ are dramatic: the first peak that forms at 460 nm is never observed. Instead, a single peak grows in and continually shifts to the red, eventually reaching 510nm and stopping. When the temperature is increased and the ZnS shell is added, QDs grown with $In(CH_3)_3$ do not grow as large as those grown with InCl3 or no indium present. Figure 5b shows the effects NaCl has on the heterogeneous growth. It should be noted that in the NaCl experiment, the amount of NaCl added is equivalent to the number of moles of chlorine associated with 10 mol% $InCl_3$. NaCl is selected because it is believed that the ionic radius mismatch between Na^+ and Cd^{2+} will either force Na^+ ions to the surface of the particles or caused their complete removal from the particles. Similarly to the synthesis where indium and chlorine were excluded, both emission peaks persist during the low-temperature phase of the synthesis instead of the first eventually being consumed to provide growth material for the second peak. It will be shown later that, within the experiment time scale (~ 20 hrs), the NaCl experiment never reaches a maximum photoluminescence point at 460 nm whereas all other experiments show a photoluminescence maximum reached some time during the low-temperature phase, indicating that the 460 nm peak is stabilized by the presence of NaCl. Also, after the ZnS shell is grown, it can be seen that the final particle emission spectrum is noticeably broader than that in all other experiments.

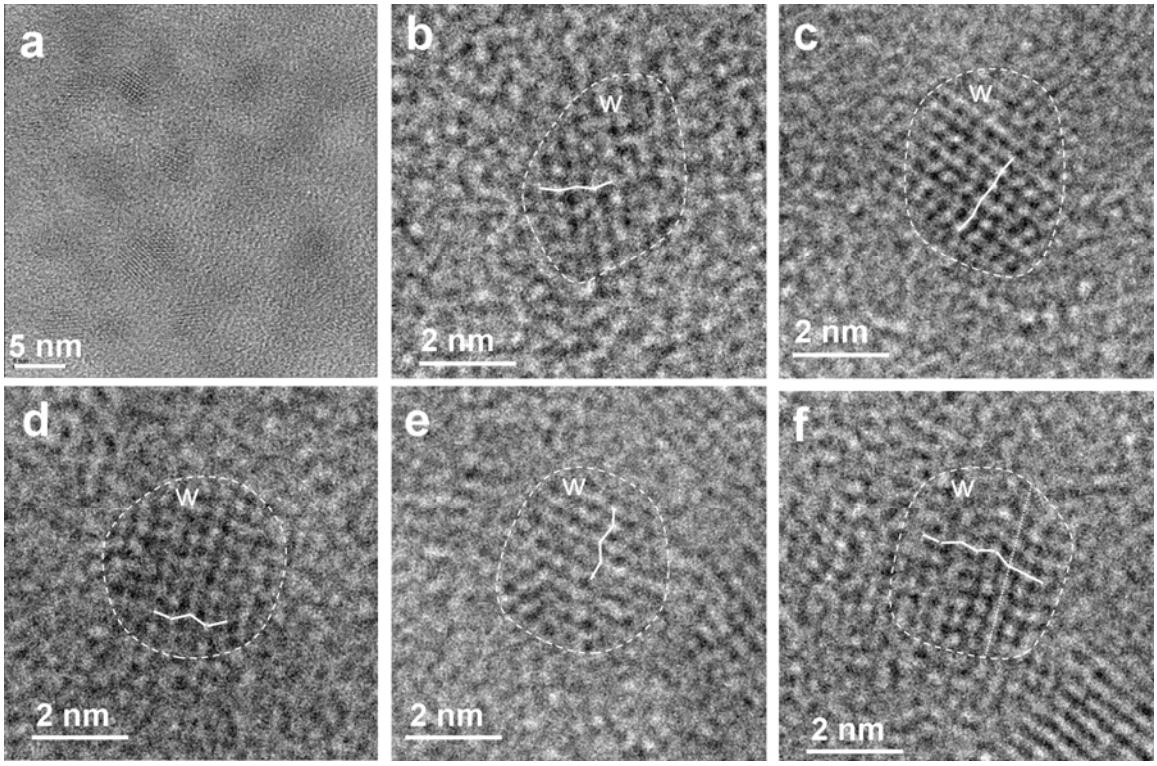

Figure 3-7 High Resolution TEM Images of Indium Doped CdSe Quantum Dots[70]

HRTEM images in Figure3-7a-f are representative of particles grown by the method outlines in this manuscript. These specific quantum dots are taken from the 5 mol% $InCl_3$ product. A wurtzite structure is clearly visible though a white zig-zag line, representing the ABABAB…stacking sequence of the hexagonal basal planes, has been added to guide the viewers eye.

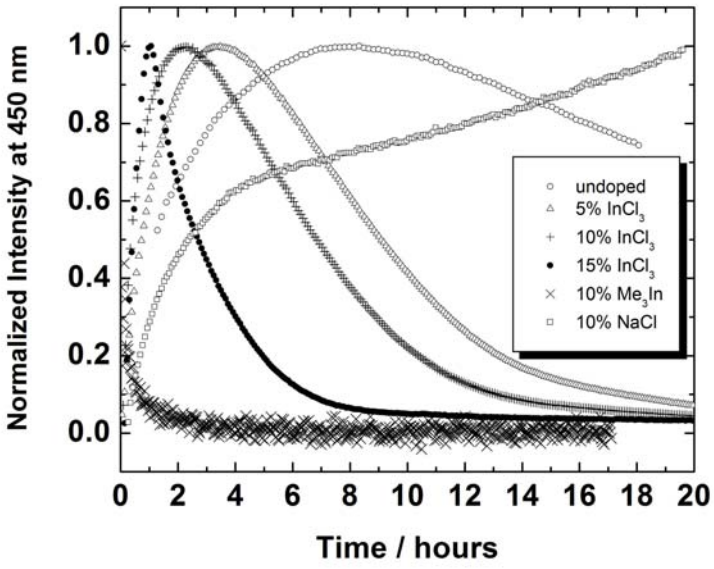

Figure 3-8 Normalized Fluorescence of the Magic Size Nanocluster at 480 nm Over Time[70]

A more in depth analysis of the effects of indium and chlorine on the growth of QDs is presented in Figure 3-8 showing the changes in normalized photoluminescence intensity at 460nm with respect to time depending on the various doping agents and concentrations. As the concentration of $InCl_3$ increases, the maximum emission is reached quicker, while $In(CH_3)_3$ reaches a maximum emission almost immediately. Additionally, as the concentration of indium chloride increases, the emission at 460 nm decreases quicker, indicating that the magic sized nanoparticles producing emission at 460 nm are removed faster in the presence of indium. The addition of NaCl causes the ensemble to never reach a maximum emission within the time frame of the experiment (~ 20 hrs); rather it begins to steadily climb, indicating that NaCl actually stabilizes the particles against further growth. Final proof can be seen in the $In(CH_3)_3$ line as it drops off almost immediately once reaching a maximum emission intensity.

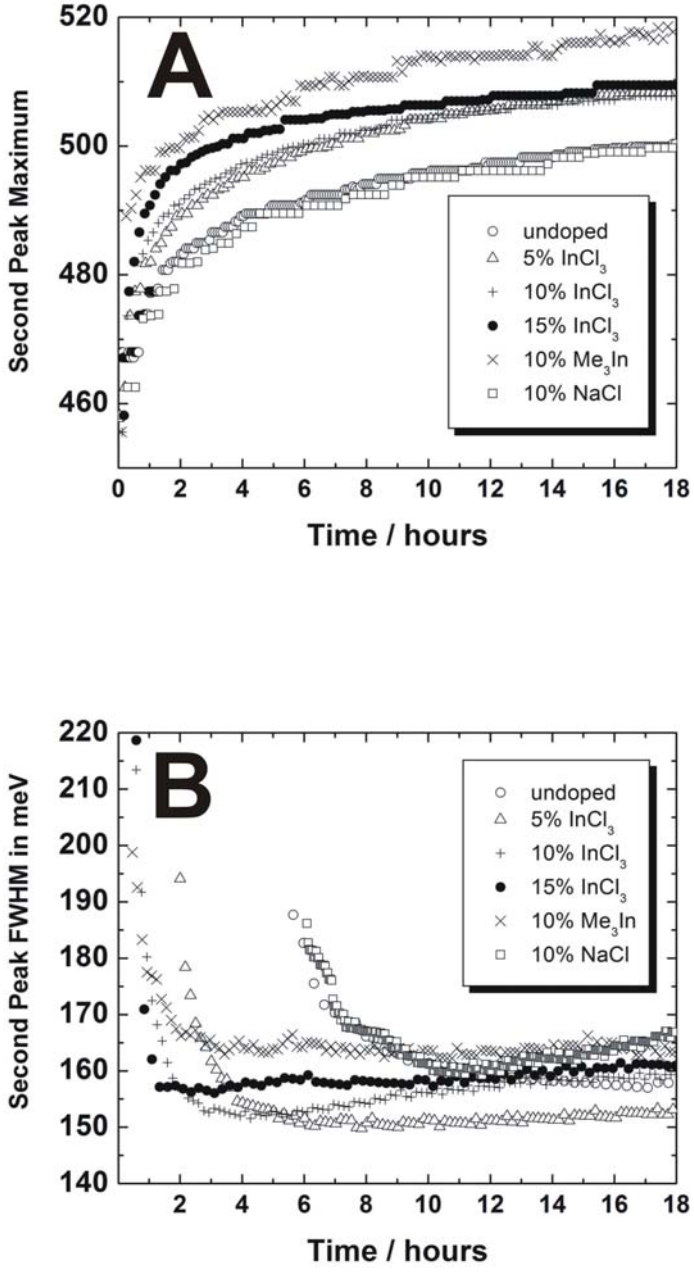

Figure 3-9 Peak Position of Larger CdSe Quantum Dots Over Time (A) and FWHM of Fluorescence Peak (B)[70]

Figure 3-9a shows the maximum position of the second peak with respect to time. All of the syntheses follow a similar trend, in which the rate of growth has slowed considerably by the fifth hour. The amount of $InCl_3$ or $In(CH_3)_3$ alters the growth rate until the fifth hour, the 10 mol% $In(CH_3)_3$ grows quickest during the initial hours, while the growth rate increases with

increasing mol % of $InCl_3$. QDs grown without dopant or with NaCl display virtually the same growth rate, which is significantly slower than QDs grown with doping agents present. Combining the information given in Figures 8 and 9a, a compelling case can be made that the addition of a doping agent activates the particle surface to further growth. The trend in growth rate provided by Fig 9a corresponds to the trend in maximum emission time at 450 nm, the faster growing particles reach a maximum emission at 450 nm quicker.

Figure 9b shows the relationship between the full-width-half-maximum of the second peak with respect to time and the type and concentration of the doping agent in meV. When the 450 nm peak reaches its maximum intensity in Figure 8, the second peak reaches its narrowest FWHM (Figure 9b), providing evidence that a size focusing takes place. This holds true for all experiments discussed here, except for the NaCl synthesis which never reaches a maximum intensity at 450 nm. Again, combining Figure 6 with Figure 9b provides still more proof that the presence of indium activates particle growth. The FWHM minimum shown in Figure 9b corresponds to the period of time in Figure 8 where the emission at 450 nm is decreasing. This indicates that once a maximum emission at 450 nm is reached, the smaller particles are consumed to provide monomers for the larger particles. There is also a relationship between the growth rates (Figure 9a) and the minimum of the FWHM, where the minimum FWHM corresponds to the approximate time the growth rate of the second peak begins to curtail. At this point, the monomer concentration in the solution has dropped below the critical concentration for colloid growth and Ostwald ripening begins to occur.

Analysis of the CdSe Nanoparticles: Table 3-1 summarizes the quantum yield of different batches of particles in relation to the amount and type of dopant added to the synthesis as well as final peak position of the purified dots and the amount of ^{116}In detected by neutron activation. For clarification, the maximum emission position reported in Table 2 differs from those seen in the figures previously discussed: the in situ monitoring shows the peak position at 250 ºC and the peak position at room temperature are vastly different. This is due to the thermal excitation of the particles. As the particles cool, thermal energy is removed and the band edge sharpens due to fewer thermally excited phonons and or electrons. The QY decreases when a doping agent is added and when NaCl is added. This is indicative of defects deep inside the particle caused by successful incorporation of indium or of surface traps caused by indium atoms bonded to the surface of the particles. It should be noted that these surface traps are caused by a

defect atom and not a dangling bond, and therefore cannot be eliminated with the growth of a ZnS shell on the particle surface, and will continue to quench fluorescence after a passivating shell is grown. The syntheses with 10 and 15 mol % of $InCl_3$ have roughly the same quantum yield, suggesting that at 10 mol % the effects of indium chloride are maximized. The change in QY is greater moving from 10% to 5%, and can be explained as a decrease in defects correlating to a decrease in available dopant. Interestingly, $In(CH_3)_3$ shows a far lower drop in QY compared to $InCl_3$, but the drop in QY of the NaCl batch is also far reduced from the undoped batch. Both indium and chloride ions effect the QY as seen from the NaCl and $In(CH_3)_3$ samples, with the NaCl having a more pronounced effect. If the quantum yield data from Table 1 is compared with the time evolution of the photoluminescence data in Figures 2-4 the conclusion is that the initial quantum yield of the nanoparticle at 120 ºC is over 50% which indicates high quality crystals present in the growth solution. The exception is the Me_3In data in Figure 4b, when the quantum yield is actually higher after growing the shell around the particle compared to the low temperature growth data.

Table 3-1 Quantum Yields, Diameters and Indium Conentrations for Indium Doped CdSe Quantum Dots[70]

experiment	QY	final PL peak position (nm)	indium detected (mol %)	λ_{abs}	diameter (nm)	concentration mol/L	In atoms per QD	In atoms per QD after pyridine exchange
no indium	27%	532	ND	517	5.11	1.13×10^{-6}	0	0
5% $InCl_3$	10.7%	563	0.40	550	5.79	9.53×10^{-7}	7.5	6.5
10% $InCl_3$	7.9%	571	0.49	558	6.00	1.06×10^{-6}	10.1	12.3
15% $InCl_3$	8.2%	581	0.44	572	6.43	9.62×10^{-7}	11.3	9.2
10% Me_3In	17.9%	504/519	NA	506	4.93	1.08×10^{-6}	NA	NA
30% NaCl	12.7%	543(shoulder)/558	NA	526	5.27	1.31×10^{-6}	NA	NA

Table 3-1 contains the data regarding the effects of indium doping on the nucleation of QDs. The concentration of particles is calculated by the method outlined by Yu.[100] First, the calculated diameters of the particles differ as explained earlier. Second, all of the concentrations of QDs are within 10% of the mean value, indicating that adding indium or chlorine does not change the nucleation of particles grown by this method. Failure to alter the nucleation pattern indicates that this method does not create more highly energized nuclei that would alter the growth kinetics, rather that the indium and chlorine that are responsible for the activation of growth. If indium or chlorine were to effect the nucleation, significant deviation in the

concentration of the particles would be expected, indicating that smaller or larger nuclei are required to begin the growth phase.

Nuclear Activation is used to detect whether or not indium is successfully incorporated into the QDs. Crude material was purified 8 times through the MeOH/toluene process. After eight washes the articles were no longer soluble in toluene indicating the amine surface ligands had fallen off. Loss of surface ligands ensures that any indium located on the surface of the ZnS shell is washed away. The mol% detected for the 15% $InCl_3$ sample shows that there is no relationship between the mol% added to the system and the amount of indium detected, as the amount of indium detected for the 15 mol% sample is lower than the amount detected for the 10 mol% sample. There does appear to be a correlation between the amount of indium detected and the quantum yield, as the quantum yield decreases the amount of indium detected increases. This suggests that indium doping quenches fluorescence.

Pyridine ligand exchange was shown to remove Mg^{2+} surface bound atoms[101] and the same technique is used here to remove any surface bound indium atoms. After refluxing the particles for 2 hours in pyridine and precipitation with hexanes nuclear activation data show no observable loss of indium atoms within the experimental error (20%). This indicates the vast majority of the indium atoms are deep enough in the particle that they are not lost during pyridine exchange. It is clear from this data that indium atoms incorporated into the quantum dots are retained through surface ligand exchange.

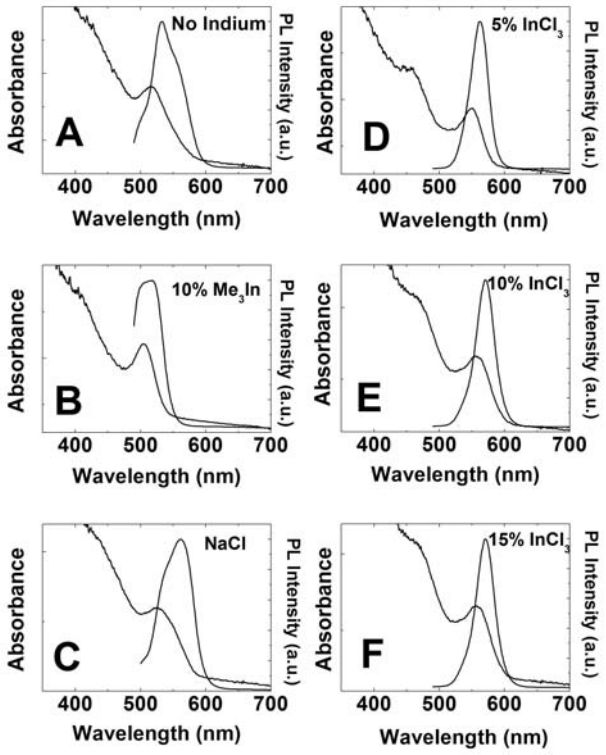

Figure 3-10 Absorption and Fluorescence Spectra of Indium Doped Quantum Dots[70]

Figure 3-10 shows the absorption and emission spectra of the purified samples. The absorption and emission features of the $InCl_3$ samples are very narrow. FWHM of the emission peak is approximately 120±5 meV for all three $InCl_3$ samples. This is a significant improvement over 160 meV in Figure 9b after the 18 hour reaction at 120 °C. The narrowing emission peak strongly suggests that there is a second focusing stage when the temperature is raised to 240 ºC. The second focusing stage may be the result of the further activation of the remaining precursor fragment producing high monomer concentration. The width of the peak is still broad compared to the best literature result.[99] The undoped and the NaCl samples show complex emission and absorption structures. This is the result of an aggregated type of growth of the magic sized nanoparticles still present after 18 hours of reaction at 120 ºC and the second size[38]. It is noted also that the Me_3In sample also shows double peak behavior, which suggests a second nucleation step leading to aggregated type of growth.

Growth Model: The general growth model for the effects of indium doping during the low-temperature growth phase is depicted in Figure 3-11. The figure only shows the relationship between the monomer exchange of the magic size nanoparticle and the solution.

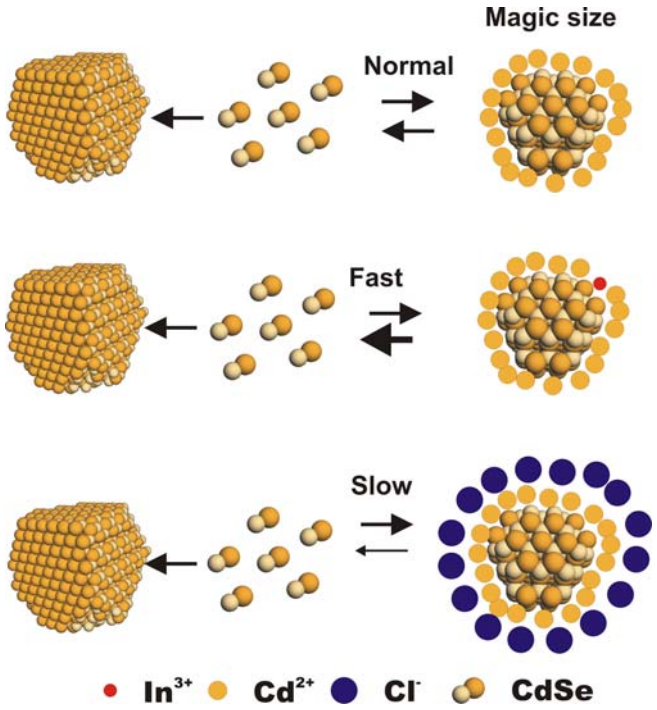

Figure 3-11 Heterogeneous Growth Model for Doped Quantum Dots[70]

The top image represents the growth when no dopant is present. The monomers released from the single source precursor molecule readily form the magic sized nanoclusters. Due to the increasing monomer concentration at the beginning of the growth the concentration o the magic size nanoparticles increases. At the same time, the larger nanoparticles continue to grow and their size distribution focuses. Once the monomer concentration drops below the solubility limit, the size distribution of the nanoparticle increases and the nanoparticle growth significantly slows down (see Figure 9). The second scheme shows how adding indium to the particle surface accelerates the dissolution of MSNC to monomers. This results in a growth that occurs much faster because of the alteration of the surface energy caused by placing a +3 ion instead of a +2 ion. This may also cause a stronger bond for the next monomer, so that the rate of monomer attaching to the surface far exceeds the rate of monomers falling off the particle surface, which would explain why the $In(CH_3)_3$ reaction proceeds so fast that the MSNC is almost not observed. Last, the scheme shows how the chlorine ions actually stabilize the MSNC as observed in Figure 8. When the chlorine ions bond to the particle surface, the rate of monomer exchange on the

surface slows. It can be concluded that the indium atoms have a greater effect on the growth kinetics, otherwise the $InCl_3$ samples would not have a larger final size after the high temperature growth phase. Also, when only indium is present, the rate of dissolution and growth rate to the second size is so fast that few monomers remain for the high temperature growth phase. This explains why the final particle size is so much smaller. The presence of a shoulder on the blue side of the spectrum- at the high temperature growth phase- Ostwald ripening is more prominent when chlorine is present and acting to stabilize the MSNC. This stabilization ensures that when the high temperature growth phase begins, there are sufficient monomers left to prevent Oswald ripening from dominating the high temperature phase.

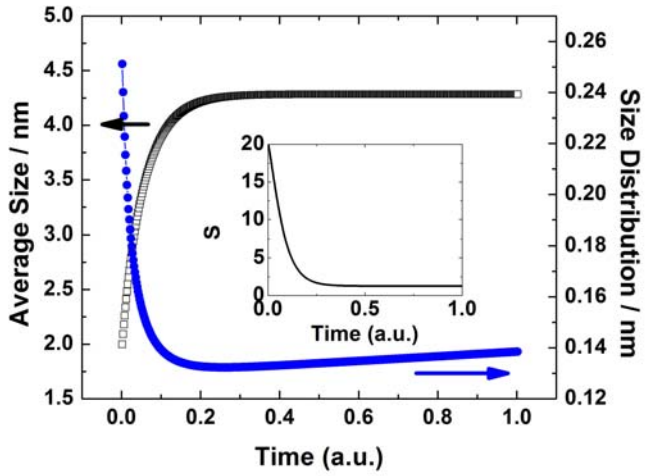

Figure 3-12 Growth Kinetics of Indium Doped Quantum Dots[70]

Figure 3-12 shows a simulation of how the ensemble of CdSe QDs in the present synthesis evolves. The second peak in the experimental data is used to monitor the focusing and defocusing of the particles. The details of the simulation are described elsewhere.[30] The inset of the graph shows that initially there is high monomer concentration present in the reaction mixture represented by S, which is the supersaturation of the monomer. As long as high concentration of monomers is present, the average QD size increases and the size distribution becomes narrower. The relatively long supersaturation can be explained by the presence of the small clusters that results higher solubility of the monomer; therefore larger supersaturation. Once the parameter S approaches 1, Ostwald ripening takes over the process. Initially, no significant change in average size takes place, but the size distribution becomes broad. Qualitatively, this data fits very well with the data presented in Figure 3-9.

The simulation assumes an initial size distribution to calculate the evolution of an ensemble of nanoparticles. The simulation predicts that the initial distribution will focus over time. If we take the magic size nanoparticle size distribution (FWHM=~80 meV) as the initial distribution, a narrower emission is expected for the second peak. The observed initial distribution for the second peak is close to 200 meV, which seems contradictory. If the nucleation event is not instantaneous then the broad initial distribution can explain the observed broadening. Although the theory can give reasons for the broadening, the physical meaning of this broadening remains to be explained. Potentially, if the nucleation event in this synthesis can be controlled, the synthesis could yield high quality nanoparticles via seeded growth.

A recent article by Knox et al.[69] concluded that indium doping does not change the optical properties of CdSe quantum dots, that the vast majority of the incorporated indium is present on the surface of the particles, and that no correlation exists between the amount of indium added to the synthetic system and the amount of indium detected by ICP elemental analysis or the degree to which photoluminescence is quenched.

Particles synthesized in the Knox report were created using a hot injection method where the doping agent ($InCl_3$) was injected simultaneously with the TOP:Se at the time of nucleation, and a ZnS shell was grown on several batches of particles. Introducing the dopant during the nucleation injection can result in amorphous In_2Se_3 forming which would not show up in XRD or SAED studies. Also the mole ratios of Cd:In are so small in this report it is possible that an undetectable amount (by XRD) of this material is created. Finally, it is possible that trace amounts of In_2Se_3 remain in the quantum dots sample even after extensive washing.

The use of a single source precursor like the one used to produce the results reported here is preferable to a hot injection method. In the single source precursor method, the cadmium and selenium are already bonded together in very small clusters and the growth system is cadmium rich. This environment allows for the indium atoms present to bond directly to a preformed CdSe cluster. The cadmium rich conditions also prevent the formation of a separate amorphous or crystalline indium containing particles, in fact cadmium rich conditions might aid doping in this case by “soaking up” some of the chloride ions. However, at this time it has not been possible to determine the location of the indium within the particles. Because the emission properties of (CdSe)ZnS core-shell quantum dots are determined by the narrower band gap

CdSe, it is most likely that the indium incorporated in the particles reported here is on the "surface" of the CdSe core, sandwiched between CdSe and ZnS.

Like the Knox report, our results do not show a significant change in Stoke's shift or FWHM from particles growth without indium present and those grown in the presence of indium. All of the differences reported here such as peak shape and position can be explained by changes in size of the particles. Unlike the report by Knox et al., the results presented here suggest a correlation between the amount of indium detected by nuclear activation and the quantum yield of the particles.

Conclusion

This study has shown that particles of significantly different size can co-exist in a colloid system. It was previously believed that only one "family" of particles, centered about a single average size, could exist and that growth occurred in a stepwise manner from family to family. Here it is clearly seen that two distinctly different families can exist simultaneously. When various doping agents are introduced, the growth and dissolution rates of the particles change. The addition of indium as a doping agent effects not only the optical properties of the nanocrystals but also their growth kinetics. Indium is found to activate the smaller MSNC to further growth, while chlorine was shown to stabilize the MSNC against further growth. Both indium and chlorine are found to effect the quantum yield of the particles, and nuclear activation verified the presence of indium in the quantum dots after all growth phases were completed. The presence of indium indicated that some of the indium is retained by the quantum dots. At this time is it not possible to determine the location of the indium atoms, but strong evidence exists to support their location being in the top most layers of the CdSe core.

Chapter 4 - Indium and Tin Doped CdSe Quantum Dots

Introduction

After several decades, semiconductor quantum dots still remain in the focus of the scientific community. From the point of fundamental science, the initial thrust of quantum dot research mainly concentrated on the size control and the phenomena associated with size dependence.[102] The emphasis of the research gradually shifted towards achieving more delicate control over the quantum dot properties. Significant advancements include the control of the shape,[23, 39] the surface of the quantum dots[7, 103] and initiating their self-assembly to more practical structures.[104, 105] These important developments of semiconductor quantum dot research have opened up multitude of applications.[106] While these research areas continue to be important and relevant, one of the next frontiers of quantum dot research will focus on the inside of these quantum dots. Specifically, how foreign atoms affect the electronic structure of quantum dots during doping (incorporating a foreign atom into the semiconductor).[75, 90, 91] As expected, incorporation of dopants into semiconductor quantum dots will play a crucial role in curtailing the quantum dot properties. Doping makes the manipulation of the conductivity of the quantum dot possible (n and p-type material), which will facilitate the creation of quantum dot based p-n junctions. Critical components of this research are to find ways to circumvent challenges and understand the underlying mechanisms of doping of nanoparticles including quantum dots.

Challenges in doping semiconductor nanoparticles come from the lack of understanding of the science of the underlying principles of doping as well as from the technical difficulties to characterize the doped particles. While studying the nucleation of small metal crystals from binary metallic melts, Turnbull et. al[107] suggested that doping of small crystallites would be difficult because small nuclei contain relatively few atoms. Specifically, dopants expected to be incorporated into quantum dots randomly, therefore, producing only a few doped particles with varying amount of dopants. Another important question is the stability of the dopant inside the quantum dots. Self purification is expected to potentially affect the doped particles whereby the dopant is pushed to the surface of the quantum dots. Despite these difficulties, doped nanoparticles are successfully produced. Recently, Norris et al[75] showed that the above difficulties may not be applicable to Mn doped ZnSe nanoparticles, but rather the morphology of

the surface plays a crucial role during quantum dot synthesis. By manipulating the ratio of the Zn/Se, they have successfully increased ratio of the <001> facet, which resulted in increased absorption of Mn dopants. While the thermodynamic argument is useful if equilibrium conditions can be achieved, Norris[94] suggested that at lower temperatures growth kinetics via trapping the dopant can play an essential role in the incorporation of dopants into quantum dot.[76] Dopants not only can get trapped, but may activate the quantum dot surface to accelerate the monomer exchange rate, therefore, influencing the overall growth kinetics of the particles. Our group has recently showed that the addition of indium dopant increases the rate of magic-sized CdSe quantum dissolution kinetics.[70]

In addition to the conceptual difficulties, characterization of the doped quantum dots is complex. Determination of dopant concentration in the ensemble of quantum dots is straightforward, but per particle chemical analysis is rather challenging. Spectroscopic techniques via photoluminescence quenching offer indirect evidence of n-type quantum dots shown by Shim et al.[90] No similar method exists for p-type quantum dots. Static electrical conductivity measurements may contain ambiguities of the conductivities of individual quantum dots. Recently, the development of terahertz spectroscopy offers some hope to measure the increased conductivity of p or n-type quantum dots.[108] While terahertz measurements provide the AC conductivity (polarizability) of the doped quantum dots, extraction of such information is not straightforward if phonon resonances contribute to the measurements. In the case of Mn doped CdSe quantum dots, electron spin resonance is used to interpret the hyperfine splitting of the Mn^{2+} dopant.

In this research, we aim to explore the possibility of forming doped CdSe quantum dots using indium and tin dopants. By using high-resolution electron microscopy techniques, the presence of tin and indium dopant has been confirmed. Terahertz spectroscopic results suggest alloy formation in case of tin doped samples. Photoluminescence measurements clearly indicate increased temperature dependence of the doped samples in accordance with the expected n-type nature of the quantum dots. Time-resolved PL shows that the carrier dynamics is significantly different in the oxidized doped samples.

Experimental Section

Core-shell CdSe/ZnS particles are synthesized using two steps. In the first step, a single precursor $Li_4[Cd_{10}Se_4(SPh)_{16}]$ is used to grow CdSe quantum dots in the presence of hexadecyl amine (HDA). The $Li_4[Cd_{10}Se_4(SPh)_{16}]$ single source precursor is prepared according to the Cumberland's method.[28] In a typical synthesis 25 g of HDA is placed in a three neck flask. 0.3 g of $Li_4[Cd_{10}Se_4(SPh)_{16}]$ precursor is placed on the top of the solid HDA to avoid exposing the precursor to the direct heat from the heating mantle during the initial melting of the solid HDA. For the indium and tin doped CdSe quantum dots, an additional 10 mg of dopant (5 mol % $InCl_3$ or $SnCl_2$) are added along with the single precursor. The flask is purged under argon flow while slowly heated to 120 °C. The growth of quantum dots in solution is continuously monitored via an *in situ* fiber optic fluorescence setup. The *in situ* fluorescence setup consists of a Raman probe attached to the side of the reaction vessel. A 380 nm broadband light emitting diode is used to excite the quantum dots and the reflected photoluminescence (PL) is analyzed by a fiber optic spectrometer. The solution is stirred for 18 hours at 120 °C except the high temperature sample, which is kept at 250 °C. After 18 hours of quantum dot growth, the temperature is increased to 250 °C and is kept there for 2 hours to remove the remaining precursor molecules in the solution. During this temperature increase, the fluorescence of the quantum dots falls below the detection limit of the apparatus. A solution made of 4.8 mL distilled TOP, 175 µL diethyl zinc and 26µL hexamethyldisilithiane is added drop-wise to grow a ZnS shell around the doped nanoparticles. The ZnS shell is grown for 1 hour at 250 °C. When the ZnS solution is added, the quantum dot PL reappears as expected when the surface traps of the quantum dots are passivated. During the ZnS growth, the PL is increased dramatically. The experiment shows that the PL of the quantum dot stabilizes after sometime, which is an indication of the completion of the ZnS shell growth. All chemicals are used as is except HDA and TOP those are vacuum distilled at ~2 Torr. The Zn/S solutions are prepared fresh for each synthesis.

The temperature dependant PL data are taken with *in situ* fluorescent setup described above without exposing the quantum dots to atmospheric oxygen and water. After 1 hour of ZnS shell growth at 250 °C, the heat is removed from the reaction vessel. The solution is stirred as it is cooled down to ~60 °C. PL spectra are collected. Once the temperature inside the vessel reached ~60 °C PL collection is stopped and the flask is reheated to 250 °C for 5 minutes and then cooled again to ~60 °C. While the PL is collected for the heating cycle as well, the cooling

resulted in smoother PL data due to the lack of the fluctuations induced by the heater. The process is repeated for a total of 10 cycles. Temperature data along with the spectral data are digitized. PL peaks are integrated to obtain quantitative data on the PL intensity. The PL is arbitrarily normalized to the PL intensity at 1/T = 0.00191 (250 °C).

High-resolution electron microscopy (HRTEM) and energy-dispersive X-ray spectroscopy (EDX) of CdSe quantum dots are performed using a 200 kV FEI Tecnai F20 transmission electron microscope (TEM) with a field emission gun electron source. Holey carbon grids are used to prepare TEM specimens. For each sample, a droplet of toluene or methanol-based solution of quantum dots is cast on a holey carbon grid and the grid is evacuated for several hours before inserting it into the microscope. In order to evaluate the crystal structure of the quantum dots, HRTEM images are acquired from the dots oriented close to the $[11\bar{2}0]$ zone axis. This orientation enables direct imaging of stacking of hexagonal basal planes. Thus, the wurtzite structure can be easily distinguished from the zinc blend structure, and structural defects in the form of stacking faults can be readily imaged. For the EDX study, a nanoprobe of 1 nm in diameter is used. This study is performed in the scanning transmission electron microscopy (STEM) mode: High-angle annular dark-field (HAADF) STEM image of a selected specimen area is acquired first. The nanoprobe is then positioned at a specific quantum dot and an EDX spectrum is collected. Due to the low intensity of K-peaks and low concentrations of dopants in investigated CdSe quantum dots, long acquisition times of at least several minutes are required. To minimize any undesired effects caused by beam-induced decomposition of quantum dots, sample contamination and drift, the x-ray count rate as well as the shape of the EDX spectrum are monitored during the acquisition, and the nanoprobe is repositioned when needed. Spectra from several quantum dots, typically of the order of 50-100, are added together in order to increase the signal-to-noise ratio and to detect the K-peaks of tin or indium in doped quantum dots.

The terahertz time-domain spectrometer and the analysis has been described previously,[108] but here is a brief summary: The spectrometer uses a cavity dumped output of a mode-locked Ti:Sapphire laser (λ_{max} = 780 nm, repetition rate = 2 MHz, average power = ~80 mW), pumped by a diode laser (532 nm, 4.6 W), for the generation and gating of the THz radiation. The laser is focused onto a 100 μm thick GaP (110) crystal which generates THz radiation via optical rectification. The entire THz pulse is mapped out by a small portion of the

laser pulse (gating pulse) via electro-optic sampling in another GaP crystal. The digitized signal is the time dependent electric field of the THz radiation. Its temporal Fourier transform yields amplitude spectrum in the frequency domain. The spectrum spans from 0.5 THz to 8 THz. The signal-to-noise (S/N) ratio obtained is ~500. To obtain the response of the sample to the THz radiation, two measurements are made. First, the THz electric field transmitted through the empty sample cell ($E_{cell}(t)$) is measured. Next, the THz field transmitted through the cell filled with sample ($E_{sam}(t)$) is recorded. Several measurements, typically 20-50, are averaged to obtain a reasonable S/N ratio. As the measured signal is the time dependent electric field, the complex Fourier transform of E(t) directly yields the complex refractive index of the sample. The quantum dots are dissolved in toluene along with polystyrene and thick quantum dot films are cast in polystyrene matrix. The absorption of the polystyrene in the spectral range is corrected for using effective medium approach, which is appropriate if the quantum dots are separated at relatively large distance compared to the frequency of light.

Results and Discussion

In this study, doping CdSe quantum dots with tin and indium are investigated. The synthesis of the quantum dots are carried out by a relatively low temperature (120 ºC) method using a single precursor of the CdSe. The photoluminescence of the quantum dots are monitored while the reaction proceeds in a 24 hour time period. The dopants are introduced from tin and indium chloride at 5±0.3 mol% relative to the cadmium concentration at the beginning of the synthesis. The experimental conditions (solvent to complex ratio) are adjusted so the size of the tin, indium doped and undoped CdSe quantum dots are the same within the experimental error. At the final stage of the synthesis, a ZnS shell is overgrown on the quantum dots to isolate the quantum dot from its environment.

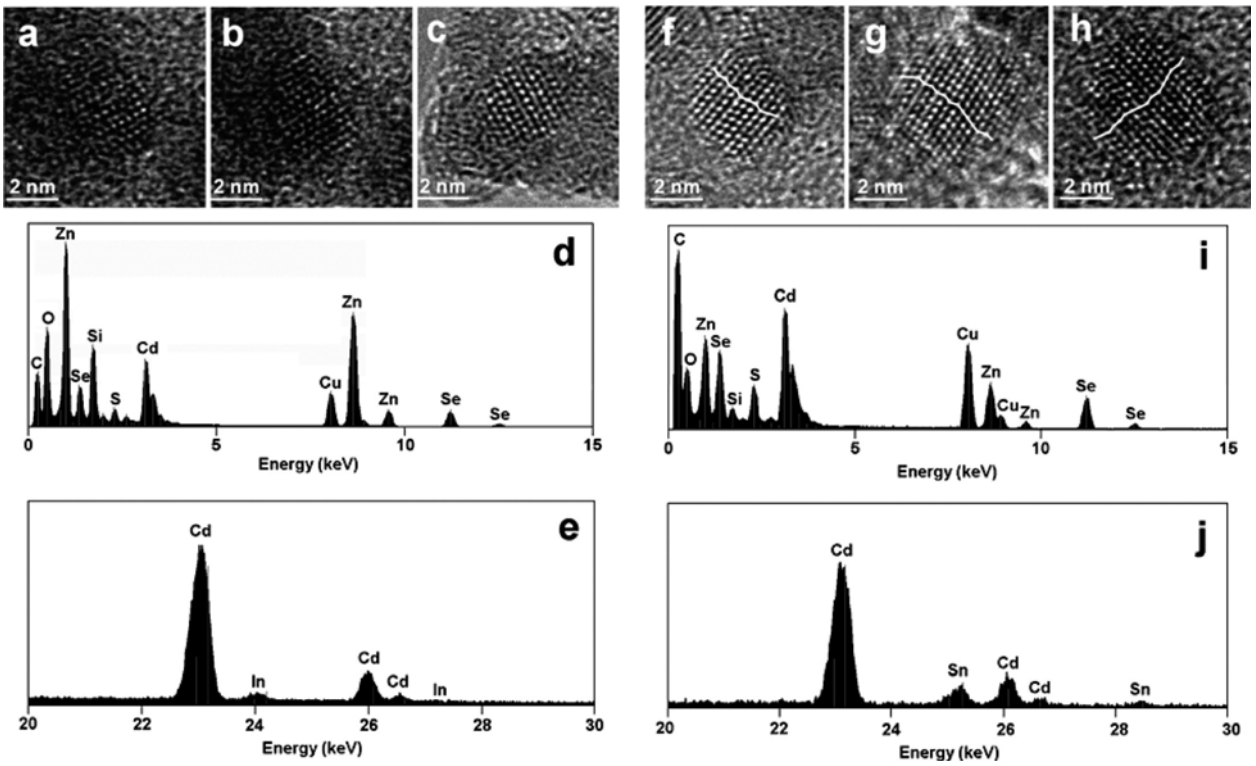

Figure 4-1High Resolution TEM Images of Indium and Tin Doped Quantum Dots along with EDX Data Confirming Dopant Incorporation[71]

Figures 4-1a-c and 1f-h show the HRTEM images of indium and tin doped CdSe quantum dots, respectively. These quantum dots exhibit high crystallinity and are found to be formed in the wurtzite structure primarily. Structural defects in the form of stacking faults of the hexagonal basal planes, equivalent to the local zinc blend structure, are frequently observed, as seen in the HRTEM images, especially in the Sn-doped sample (Figure 4-1f-h). More detailed interpretation of similar HRTEM images is given in literature.[109] EDX spectra of indium and tin doped CdSe quantum dots are also shown in Figure 4-1. From the lower-energy spectra, measured below 15 keV, it can be seen that the Zn/Cd peak intensity ratio in the indium doped sample (Figure 1d) is higher than the one measured in the tin doped sample (Figure 1i), suggesting slightly thicker ZnS shell in the former case. The low-energy part of the EDX spectrum (below 5 keV), also contains the information about the dopants as the characteristic X-ray L-peaks of In and Sn appears there. The extraction of the dopant information from this part of the spectrum is difficult as both, the In and the Sn L-peaks greatly overlap with the much stronger Cd L-peaks. Therefore, in order to study the incorporation of indium or tin into CdSe quantum dots, EDX spectra are also measured in the higher energy range between 20 and 30

keV, where well-separated K-peaks of Cd, In and Sn appear. This establishes the incorporation of indium and tin into CdSe quantum dots as shown in Figure 1d and 1j, respectively. In the indium doped sample, the dopant concentration is found to fluctuate significantly from particle to particle, whereas it is more stable in the tin doped sample. The EDX quantification yields approximately 11 ± 1 mol % and 5 ± 0.5 mol % average dopant concentration in the tin and indium doped quantum dots, respectively. It is possible that tin is present in greater quantities because replacing Cd^{2+} cations with Sn^{2+} dopant atoms is less energetically unfavorable than replacing Cd^{2+} with In^{3+}

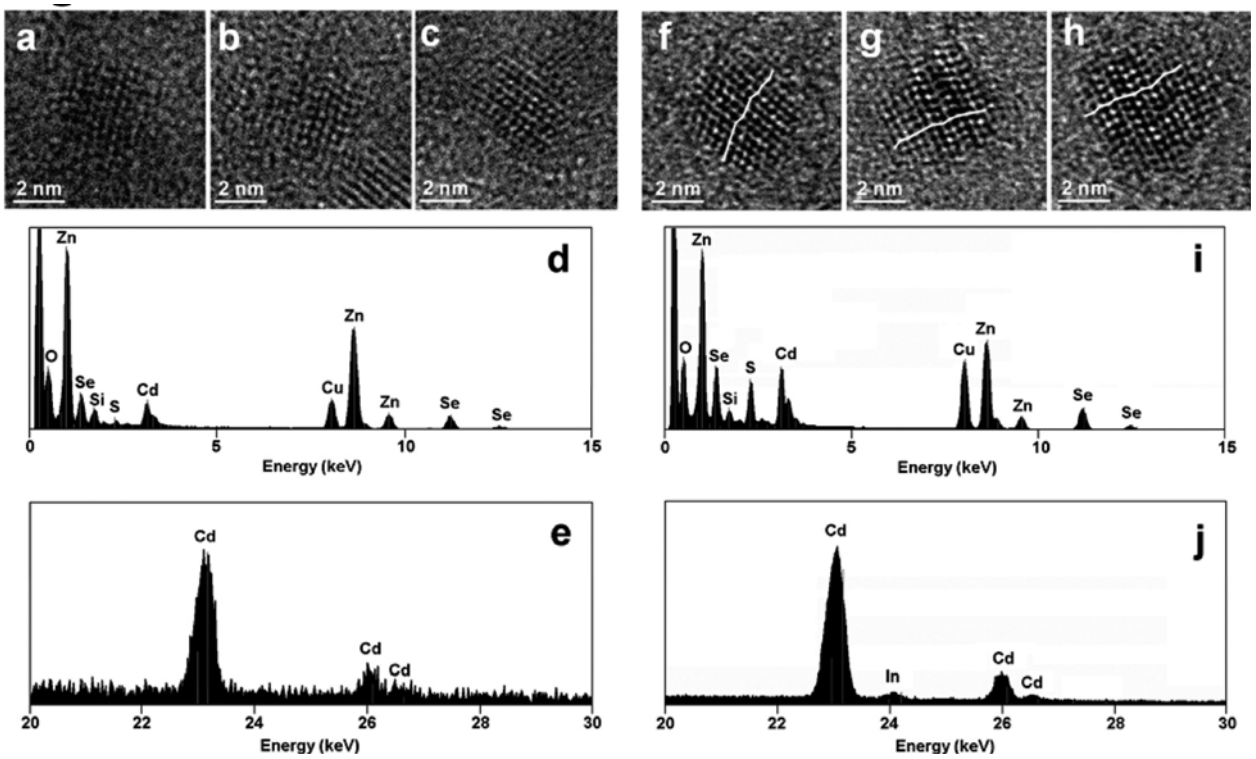

Figure 4-2 HR-TEM and EDX of Doped Particles Grown at 200 °C[71]

Figure 4-2 presents similar HRTEM and EDX results obtained from undoped CdSe quantum dots and quantum dots produced during 'high-temperature' indium doping at 250 ºC. The nanostructure of these quantum dots, as revealed by HRTEM study, resembles that of tin or indium doped quantum dots. Again, quantum dots are formed primarily in the wurtzite structure, however, numerous basal stacking faults are observed, especially in the In-doped sample (Figure 4-2f-h). Lower-energy EDX spectra of these samples indicate significantly high Zn/Cd ratio and thick ZnS shell (Figure 4-2d,i). No indium peaks were detected in quantum dots from the high-temperature doped indium sample (see Figure 4-2j). The higher-energy spectrum of this sample

resembles the spectrum measured for undoped quantum dots (Figure 4-2e): only Cd K-peaks are visible there with no significant trace of In peaks.

The dopants loaded into the reaction mixture may yield varying amount of dopants per particles.[110] The statistical theory below describes the simplest case of doping and any deviation from it is interpreted as a clue to the underlying mechanism of doping in the specific case. When uniform concentration of dopants is introduced into a solution during the growth of quantum dots, the probability of doping depends on the dopant concentration and the radius of the quantum dot. The probability of a given number of dopant (k) occupying a quantum dot with volume V is determined by the Poissonian distribution (eq. 1):

$$\text{(eq. 1)} \quad P(k) = \frac{e^{-Vn}(Vn)^k}{k!}$$

, where n is the dopant concentration given in $1/m^3$. The results predicted by the statistical theory are summarized in Figure 3. In these calculations, the quantum dots are assumed spherical and the dopant concentration corresponds to the experimentally used dopant concentration (5 mol%). Figure 4-3 UPPER shows the how k (# of dopant /particle) changes with the size of the quantum dot. According to this theory, as the particle becomes larger, the probability of doping increases. For the experimental size of the CdSe quantum dots (r=1.62 nm), the predicted dopant distribution for this size is shown in Figure 4-3 LOWER LEFT.

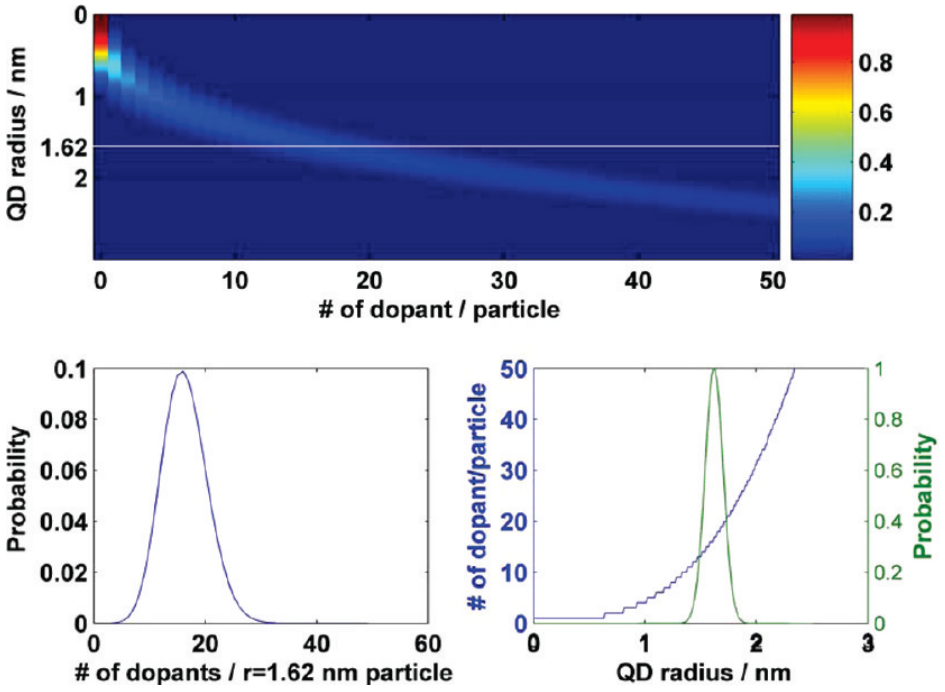

Figure 4-3 Probabilities of Dopant Incrporation[71]

From the peak maximum of the probability distribution, the number of dopants per particle is approximately 17 dopants. Since the nanoparticles have a finite size distribution of approximately 10%, it is expected that the maximum of the probability distribution number varies within the size distribution. Figure 4-3 LOWER RIGHT shows how the most probable dopant changes over the size distribution of the particles. The very small quantum dots will have only a few dopants, while the larger quantum dots may have twice as many dopants. These numbers are relatively high compared to bulk doping values, but not all the dopant would be active in case of quantum dots. The theory predicts though that it is more likely that larger particles have the 'right' dopant that could ionize more efficiently.[77] Due to the limitation of the analytical technique used to determine the dopant number/particle in this experiment, the size selective correspondence between theory and experiment cannot be established at this point. However, the experiment above shows that tin dopants preferentially incorporate into the quantum dots during growth, while the measured concentrations of indium dopants agrees well with the statistical theory.

Efros *et al*[76] have suggested that a dopant may incorporate into a quantum dot via 'trapping' at a particular location. The requirement of doping is that the dopant binding to the surface is strong compared to the thermal energy, and the dopant-surfactant complex easily

dissociates on the surface of the quantum dots. The data show that there is indium doping when the quantum dots are grown at low temperature, and indium is also incorporated into the quantum dots synthesized at 250 ºC at the same concentration level. Based on the growth conditions, the activation energy of the dopant desorption must be very small. Efros *et al.* also pointed out the role of the surfactant-dopant complex, which cannot be too strong under the experimental conditions; therefore, the 'usual' phosponic acid based synthesis of II-VI quantum dots would yield strong dopant-phosponic acid complexes. Following this argument, in this study, the quantum dots are synthesized in the presence of hexadecyl amine, which is also proven to be a better solvent for manganese doping of CdSe quantum dots.[75]

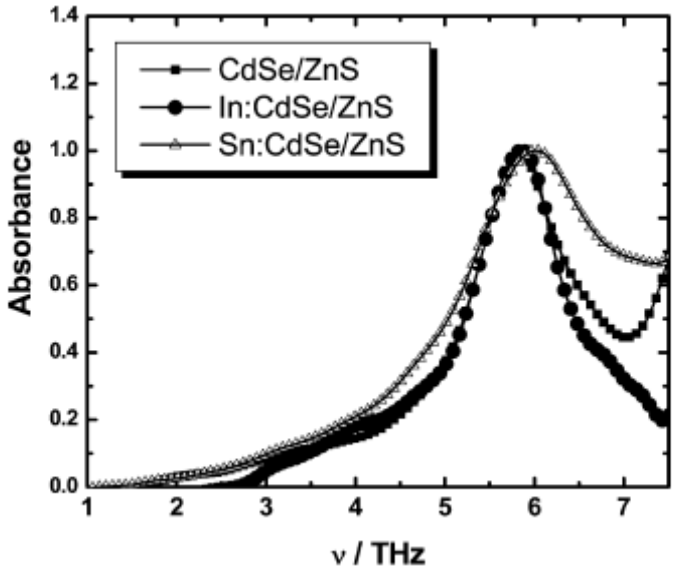

Figure 4-4 THz Spectrum of Indium and Tin Doped Quantum Dots[71]

While the indium doped samples show statistical distribution of the dopant, the tin doped samples indicate a different mechanism that leads to the preferential adsorption of tin. Figure 4-4 shows the experimentally measured terahertz absorbance of the doped and undoped quantum dots. The main feature in the THz absorbance spectra of the CdSe quantum dots is a strong resonance at ~5.75 THz (~ 192 cm^{-1}). This strong absorbance peak is due to a coupled mode between longitudinal optical (LO-211 cm^{-1}) phonon and transverse optical (TO-169 cm^{-1}) phonon modes, namely the Fröhlich mode, and has been observed earlier in simple far-infrared spectra for small CdSe nanoparticle ensembles.[111] The frequency of this particular mode exhibit a modest size dependence. For smaller particles, in addition to the Fröhlich mode, there are some other confined coupled vibrational modes which can be observed in the THz spectrum as

observed in the earlier study.[111] The Fröhlich mode in the small CdSe QD seems less intense and broadened, but this behavior is expected due to mode splitting. The data indicates a slight 15 cm^{-1} shift in the Fröhlich mode of the tin doped CdSe QDs. This shift can be interpreted as alloy formation on the surface of the CdSe quantum dots reducing the CdSe core size, which in turn increases the frequency of the resonance. Other explanations of the shift are also possible such as the modification of the phonon frequency due to alloy formation with tin. The indium doped sample does not exhibit the same behavior, but seems identical to the undoped samples within the instrumental resolution, which seems to support that the mechanism of tin and indium doping is different. Recent experimental data indicate that the indium incorporation into bulk CdSe is without the formation of a secondary phase up to 5 mol% of indium, therefore CdSe and indium tends to form a dilute alloy.[112, 113] There is no evidence to the author's knowledge about the tin in CdSe.

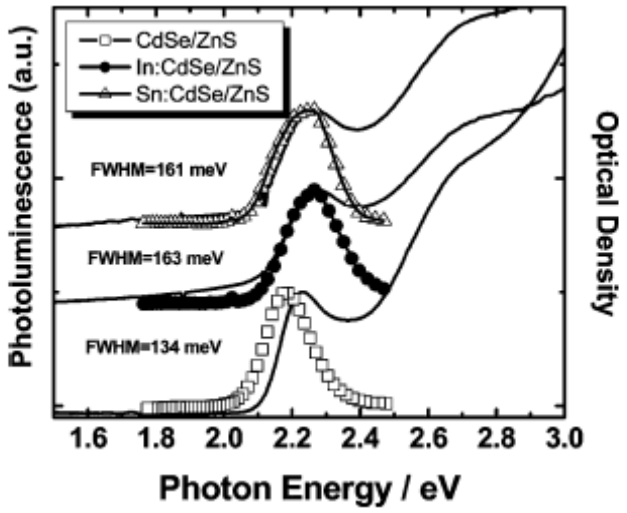

Figure 4-5 Absorbance and Photoluminescence Spectra of Indium and Tin Doped Quantum Dots[71]

Figure 4-5 shows the absorption and photoluminescence (PL) spectra of the CdSe quantum dots. The emission peak width of the undoped sample is noticeably narrower than the doped samples. The difference is mainly due to the effect of the dopant on the growth kinetics. Previous results[70] showed that the size distribution undergoes focusing during growth. As the dopant accelerates the growth, the doped samples cross the narrower distribution sooner resulting in a larger size distribution. Therefore, the broader distribution is not the result of the heterogeneous nucleation. The size of the quantum dots are controlled primarily by the initial

amount of precursor complex measured in the reaction mixture, and the reaction proceeds until most of the precursor molecules are consumed over the period of the reaction (18 hours). Both tin and indium doped samples exhibit no or little Stokes shift. The results indicate that lack of the Stokes shift is the direct result of doping. While in undoped CdSe the origin of Stokes shift is explained via dark states that are not allowed for direct 1 photon absorption, clearly is absent here. The conclusion is that the dopant levels are significantly altered the selection rules of the absorption and emission. As it will be shown later, the lack of Stokes shift could be the result of backfilling of the electron resulting in a more pronounced bright state emission.

Immediately after the synthesis and the overgrowth of ZnS shell, the temperature dependent photoluminescence of the quantum dots is measured in the temperature range of 343-524 K. The measurement takes place in the reaction vessel under argon to minimize the possibility of the oxidation of the doped quantum dots.[90, 94] This precaution is needed as predicted previously.[94] In addition, measurements of the photoluminescence are carried out after addition of the ZnS shell that isolates the particles from their environment. The results of the temperature dependent photoluminescence studies are summarized in Figure 4-7.

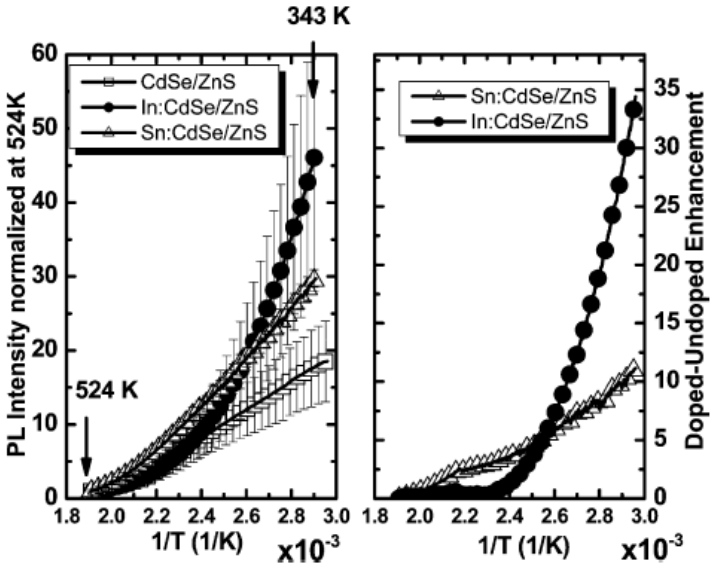

Figure 4-6 Temperature Dependent Photoluminescence of Indium and Tin Doped Quantum Dots[71]

Each curve represents the average of the 10 cycles and is normalized at 524 K for better visibility. All the curves show decreased PL with increasing temperature (or decreasing inverse temperature). The integrated PL of the undoped sample changes by a factor of approximately

18.5 between 343-524 K. In the same temperature range, the PL of tin and indium doped CdSe samples change by a factor of 29.5 and 47, respectively. Clearly, the PL of the doped samples has steeper temperature dependant curves. Figure 7 shows a complementary calculation to predict the PL quenching due to the presence of $1S_e$ electron in a 3.25 nm CdSe quantum dot in the experimental temperature range. The calculation uses a simple Fermi-Dirac statistics (eq. 2) to quantify the PL quenching via occupation probability of the $1S_e$ level from the dopants.

(eq. 2) $$n_i = \frac{1}{e^{(E_i - E_{Fermi})/kT} + 1}$$

The plot in Figure 4-5b assumes that the PL quenching is inversely proportional to the occupation probability ($1/n_i$) of the $1S_e$ level relative to the undoped quantum dot. The energy diagram of Figure 4-7 LEFT indicates the quantum confined hole and electron levels derived using the effective mass of the hole (0.45me) and electron (0.112me) in CdSe. The dopant levels are critical parameters in the calculation determining how steep the PL quenching curve.

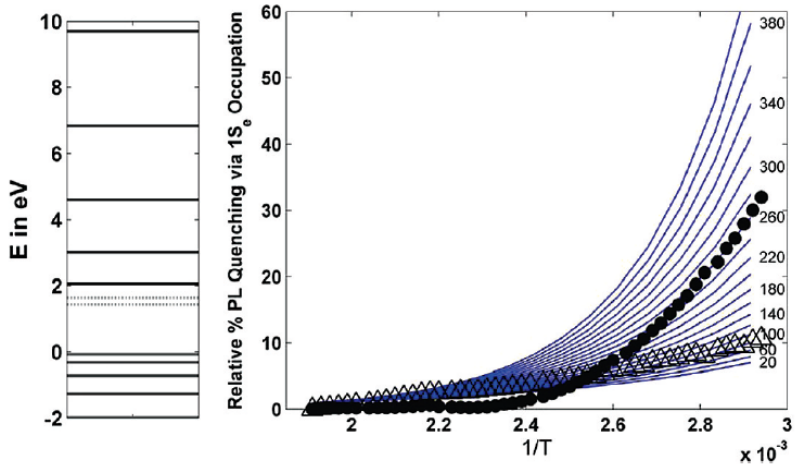

Figure 4-7 Fluorescence Quenching as a Function of Dopant Energy Level[71]

For the data presented here, dopant levels below the bulk conduction band are assumed to be between 20-400 meV to approximately match the experimental data. The calculated PL quenching is normalized at 524 K in order to directly correlate the calculation with the experiment. As both the experiment and the calculation indicates that the PL quenching increases at lower temperatures as in the case of the indium and tin doped CdSe quantum dot samples. The calculation also predicts that as the dopant energy level forms deeper below the conduction band, the temperature quenching of the PL becomes steeper. The calculation is highly approximate for several reasons. It assumes only a single dopant level (as opposed to a distribution of dopants

that accounts for the random nature of doping). It is expected that the dopants occupy several sites corresponding to different energy levels as well as the actual signal is the result from an ensemble of quantum dots (doped and undoped). The quantum dots contain a thin ZnS shell, which could contribute to the density of states above the dopant level. This later shortcoming is expected to be a lesser effect, because the quantum confined levels of ZnS conduction bands are significantly higher due to the band matching and quantum confinement. In conclusion, the calculation predicts that the tin and indium energy levels form approximately 100 meV and 280 meV below the bulk conduction band, respectively.

If electrons from the dopant levels are available for the quantum dots, one would expect backfilling of the lowest energy levels resulting in change of the optical emission. This backfilling will be temperature dependant. In CdSe, near the bandedge, there are several excitonic states from which a dark excitonic state is responsible to the Stokes shifted emission. In Figure 4-9, the PL peak maximum is shown against the temperature.

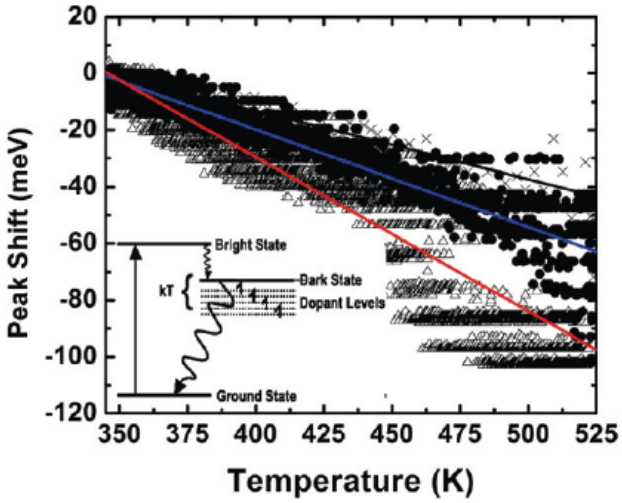

Figure 4-8 Temperature Dependent Stokes Shift[71]

In both doped samples, the peak maximum changes steeper than undoped sample. This steeper dependence could be very well the results of backfilling. In addition, the lack of Stokes shift in doped sample points towards this conclusion. Shim et al.[90] have shown that the optical absorption is also influenced by the backfilling resulting a shallow onset in case of n-type CdSe QDs. A similar feature is observable, but diminished intensity in Figure 4-8. The doped samples exhibit an extended onset in the optical absorption spectrum.

Time-resolved photoluminescence kinetics of the bandedge emission of the freshly prepared doped and undoped samples are measured, which show that the photoluminescence is dominated by a long (~35 ns) component. No significant difference could be observed between doped and undoped samples. After several days the doped samples undergo oxidation while the undoped samples remain unchanged. The time-resolved photoluminescence of doped and undoped samples are presented in Figure 4-9.

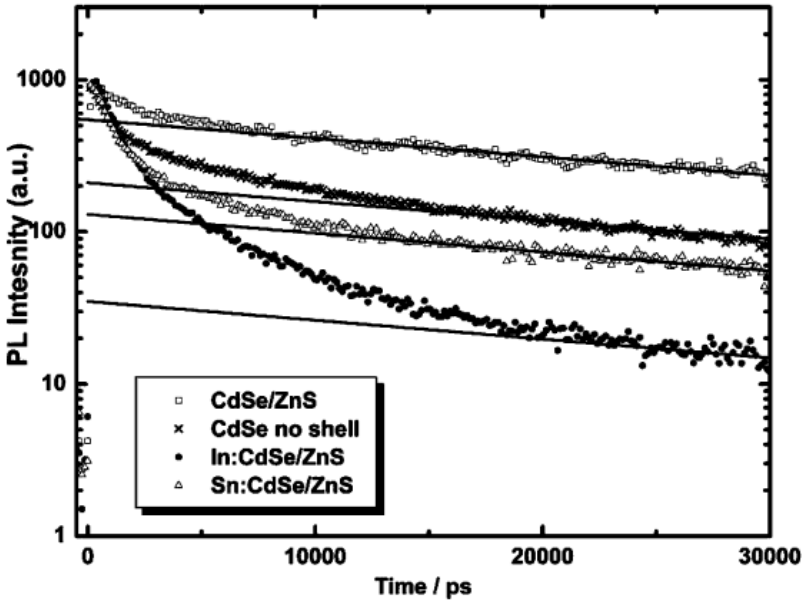

Figure 4-9 Time-Resolved Fluorescence Spectra of Indium and Tin Doped Quantum Dots[71]

The photoluminescence dynamics of the doped and undoped samples exhibit distinctly different kinetics. The kinetics of the undoped CdSe sample shows a small component of fast decay and a relatively large component of slow decay that can be fitted with a ~35 ns single exponential. Both indium and tin doped samples display very different kinetics from the undoped samples and their PLs are dominated by fast relaxation components. It is obvious from the logarithmic plot that these curves can not be fitted with a single exponential decay function, but multiple exponential components are needed to obtain a good fit. Because of the lack of the uniqueness of the fit, the data are not presented here quantitatively. Interestingly, the component of the 36.7±0.2 ns decay is present in each of the samples in Figure 4-9, which might mean that undoped quantum dots are present in all samples. As a reference an undoped sample is prepared (same size as the rest) without ZnS shell, which shows still significant ~35 ns relaxation

component compared to the doped samples. This comparison suggests that the observed fast relaxation kinetics is due to the indium and tin induced oxidation of CdSe quantum dots.

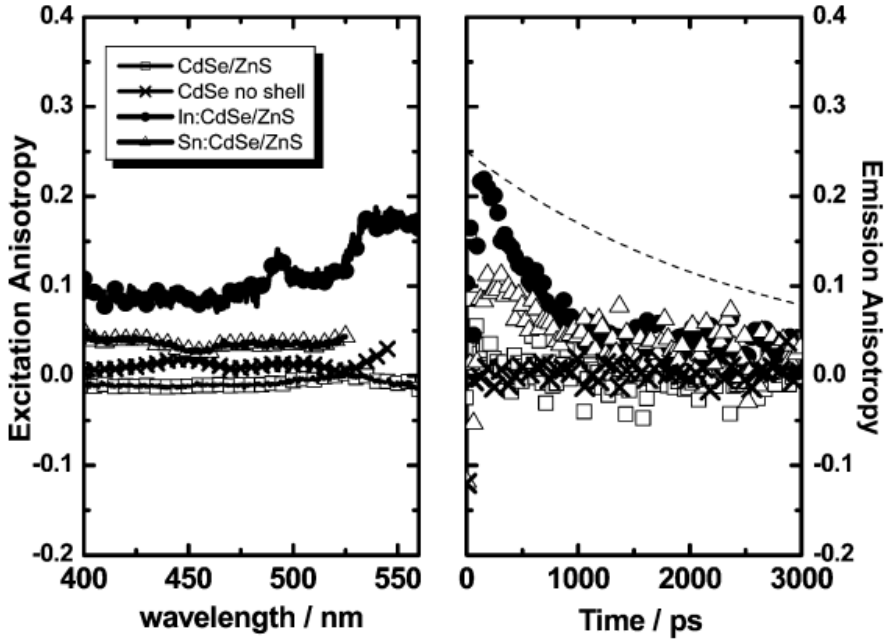

Figure 4-10 Excitation Anisotropy Measurements of Doped and Undoped Particles[71]

The excitation anisotropy (r) of the same samples is shown in Figure 4-10 LEFT. By definition $r=(I_{par}-I_{per})/(I_{par}+2*I_{per})$, where 'I' is the PL intensity parallel vs. perpendicular detection to the excitation polarization. The detector is set at the bandedge emission of the quantum dots and the excitation wavelength is scanned from 400 nm. The indium doped CdSe sample displays the largest positive anisotropy values for bandedge emission, while the anisotropy is decreasing in the order of tin, no shell and undoped CdSe/ZnS quantum dots. Again the freshly prepared tin and indium doped samples are very similar to the undoped samples showing no appreciable emission anisotropy as expected for spherical CdSe QDs. In agreement with the static anisotropy measurements, the time-resolved emission anisotropy (Figure 4-10 RIGHT) exhibit positive values of anisotropy in the same order. It should be noted that static anisotropy is the ratio of the time integrated anisotropy and the time integrated PL. Therefore, the relatively short photoluminescence lifetime of the indium doped CdSe combined with the large initial amplitude of the anisotropy results in the large static anisotropy values. In summary, the tin and indium doping induced oxidation has resulted in polarized emission if the quantum dots are excited (3.08 eV) significantly above bandedge (~2.2 eV). The decay time of the anisotropy of the samples is shorter than expected. The rotational diffusion time of 3.25 nm

sphere in toluene is calculated to be 2583 ps, which is indicated also in Figure 4-10 RIGHT by dashed line. Obviously, the emission is depolarizing faster than the rotational diffusion time of the quantum dot, which requires other sources of depolarization. A plausible explanation is the contribution from trapping dynamics, which does not stop after few picoseconds, but continues to be a factor. While the hole relaxation levels are typically faster due to the larger effective mass, it is assumed that the primarily the electron relaxation levels are affected leading to the relatively large observed anisotropies.

Conclusion

In conclusion, CdSe quantum dots are doped with indium and tin dopants. The presence of the dopants is confirmed on per particle bases. From the data it is concluded that the indium and tin doping takes place via different mechanisms. The dopant significantly changes the electronic structure of the quantum dot. Temperature dependant PL becomes steeper depending on the relative energy level of the dopant in agreement with the predictions. The PL dynamics indicate the retention of polarization in the aged doped quantum dots. The indium doped samples appear less stable even when covered with the ZnS shell, which leads to a new challenge of exploring ideas to stabilize quantum dots in the presence of the strongly reducing dopant electron.

Chapter 5 - Gallium Doped CdSe Quantum Dots

Introduction

Doping quantum confined semiconducting nanocrystals (quantum dots or QD's) will allow for a new generation of electronic devices built on a bottom-up construction model that are smaller and more powerful than devices currently fabricated by photon-lithography.[114, 115] The ability to synthesize high quality quantum dots[18, 22, 23] via bench-top chemistry makes doping quantum dots to enhance electrical properties of the utmost importance. Despite several drawbacks such low availability of elements in Earth's crust and high negative environmental impact,[116] CdSe quantum dots produced via colloidal synthesis are the ideal system for doping studies simply due to extensive investigation over the past 20 years.[117]

Due to the small number of atoms composing the QD doping was initially thought to be unlikely.[68] Several obstacles, such as self-purification[81] and low dopant solubility would have to be overcome. Reports of successful incorporation of manganese,[80, 118] cobalt,[73] chromium,[119]iron,[120]and copper[121] succeeded in introducing magnetic properties to CdSe QD's. Generation of n-type CdSe quantum dots via "charge injection" of an electron into the conduction band is accomplished using reducing agents.[91] However, up until several years ago there were no reports of attempting n-type doping of CdSe QD's. Indium has been reported in doping CdSe thin films[88] and CdSe nanowires[72] creating electron donor states below the conduction band characteristic to n-type semiconductors. Doping of CdSe QD's with indium was reported by Knox[69] however little evidence of the dopant atoms impact on the properties of the QD's was presented.

Previous reports of successful doping of CdSe QD's with indium[70] showed that the presence of indium had dramatic effects on the growth of CdSe:In. Briefly, CdSe dots grown in the presence of $InCl_3$ showed increased growth rates in the "heterogeneous growth regime" along with rapid size focusing; indium was found to activate the growth of QD's resulting in larger particles than QD's grown in the absence on dopant; and significant quenching of band-edge photoluminescence in spite of a ZnS passivating shell corroborating results reported with "charge-injected" particles,[8] as well as indium doping in thin films.[9] Further work on indium and

tin doped CdSe showed that donor electrons are not ionized into the conduction band until temperatures well above room temperature.[71]

In an ideal n-type semiconductor electrons from the donor level are ionized into the conduction band at room temperature due to the extra electron being weakly bound to the dopant atom. Due to the higher ionization temperature shown by tin and indium,[71] gallium is chosen for investigation due to reports of gallum doping in thin films of CdSe,[89] and the 4p gallium orbital may better align with the quantum dots $1S_e$ energy level and allow for better donor electron occupation.

Several new characterization techniques are developed and applied to determine the properties of gallium doped CdSe quantum dots. To our knowledge, single particle elemental analysis has never been applied and reported to determine successful doping of CdSe quantum dots. To test for donor electron ionization, we have developed and applied an in-situ photoluminescence monitoring technique across a mild range of temperatures that indicate more n-type behavior than previous reports of indium and tin doping. These studies show that the fluorescent properties of CdSe quantum dots doped with gallium are more strongly dependant on temperature than "pristine" quantum dots or those doped with indium or tin. Additionally, gallium doped quantum dots are subjected to single-photon time resolved fluorescence and are found to have significantly increased fast decay components at elevated temperature compared to undoped CdSe quantum dots and in the case of lightly doped quantum dots a third decay pathway is introduced at elevated temperatures.

Experimental

Chemicals: All chemicals were used as purchased with the exception of hexadecylamine, which is distilled at 2 torr. $InCl_3$, $SnCl_2$, $GaCl_3$, diethylzinc, hexamethyldisilithiane and tri-n-octyl phosphine (TOP) are all stored in an inert atmosphere/low water vapor concentration glovebox. Zn/S stock solution is prepared according Hines et al[16] by mixing 7mL of diethylzinc with 1mL hexamethyldisilithiane and 32 mL of distilled TOP. Tri-n-octylphosphine (TOPO) and 2-aminopropanol (APOL) are used as purchased and stored under ambient conditions.

Synthesis: Doped and undoped CdSe core particles are synthesized using the $Li_4[Cd_{10}Se_4(SPh)_{16}]$ single source precursor (SSP) prepared as reported by Cumberland[28] in

hexadecylamine with metal chloride as the doping agent. Briefly 50 g of distilled hexadeylamine and 0.6 g of the (SSP) are loaded into a three neck flask and passed into a glovebox where the appropriate amount of metal chloride is added. All dopant load percentages are based on the total cadmium content of the reaction. The reaction flask is purged on an Ar gas line for 20 minutes before being very slowly heated to 120 °C with careful attention made to minimize temperature overshoot, as the stability magic sized nanocluster is extremely sensitive to temperature. The solution is stirred at 120 °C for 18 hours while in-situ fluorescence spectra is collected.[70] After 12 hours the temperature is increased to 240 °C and the particles grow to their final size over 3 hours. ZnS shell growth is accomplished by using an automated syringe pump to dispense a solution of 2 mL of the Zn/S stock solution diluted with 8 mL of TOP over one half hour followed by one hour of growth at 250 °C. After one hour of shell growth, cooling studies are preformed. Following cooling studies described below, another layer of shell material is grown by repeating the slow injection at 250 °C. This sequential shell growth is repeated for a total of four injections.

Temperature Dependant Photoluminescence Studies (TDPL): Following ZnS shell growth the reaction mixture is allowed to cool from 250 °C to 60 °C with the flask covered with foil to ensure a slow, even cooling process. Photoluminescence spectra are recorded every second. This process is repeated five times without exposure to oxygen. A surface reflection probe equipped with a 400nm LED excitation source is used to collect the spectrum during all growth phases.

Particle Preparation for Low Temperature Photoluminescence Studies: ~1 g of crude reaction solution is dissolved in 10 mL of toluene and gently heated until all HDA is melted. This solution is centrifuged at 7000 rpm for ~5 minutes to allow all of the excess metal to precipitate out leaving a clean suspension of quantum dots. The toluene suspended quantum dots are refluxed in ~3 g tri-n-octylphosphine oxide for 4 hours followed by precipitation with methanol and resuspension in toluene and precipitated via methanol one final time. The solid is dried under vacuum for ½ hour after which 10 mL of APOL is added to the centrifuge tube and sonicated until the quantum dots disperse in the APOL.

Temperature Dependant Photoluminescence Studies of Purified Quantum Dots: A dilute solution of quantum dots in APOL is made by filling a fluorescence cuvette ¾ full with APOL and adding a pipette of QD's in APOL described above. The cuvette is fitted with a glass stem to allow accurate temperature measurement and sealed with a rubber o-ring to keep oxygen out. The experimental set up is a home-built 405 nm variable out-put laser diode equipped with UV-resistant fiber optic cables. Spectra are collected at 90° from the excitation fiber. A small heating element is located at the base of the set-up and attached to a programmable power-supply. The cuvette is placed in the experimental set up and heated to 80°C where the temperature is maintained at 80 °C for twenty minutes to ensure uniform solution temperature. The apparatus is then cooled via water pump at a rate of 1°C/minute down to 10 °C. During this time fluorescence spectra are collected every 10 seconds.

Results

High-Resolution Transmission Electron Microscopy (HR-TEM) images of 10% gallium doped CdSe@ZnS is presented in Figure 5-1. High quality, defect free core-shell quantum dots are observed. Lattice spacing of 4.3 Å are consistent with the "a" lattice constant of the wurtzite CdSe crystal phase. Particle diameter measurements support a CdSe core well passivated with ZnS based on absorbance data presented shortly.

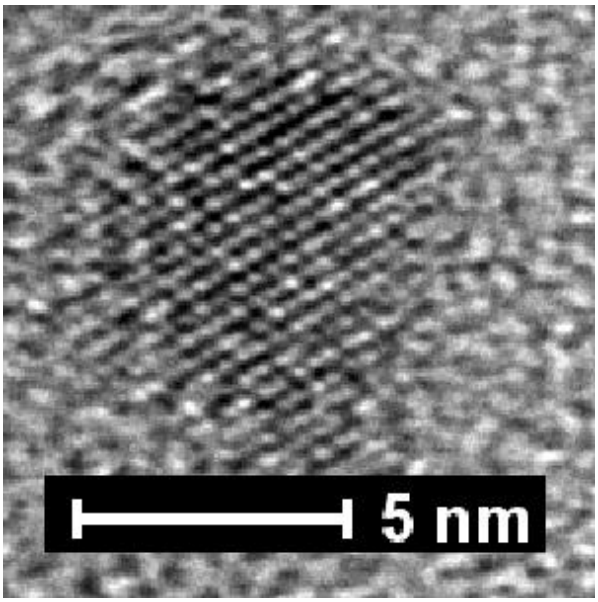

Figure 5-1 High Resolution TEM Image of a Gallium Doped CdSe Quantum Dots

Elemental analysis of single or few 5.0% gallium doped quantum dots is shown in Figure 5-2. The region of the line scan in the Scanning Transmission Electron Microscopy with High Angle Annular Diffraction (STEM-HAAD) image in Figure 5-2a clearly shows the path through several isolated quantum dots. The detected signals of various elemental x-rays of cadmium, gallium, selenium, zinc and sulfur in Figure 5-3 (respectively) show that significant detected signal for all composite elements corresponds to the location of the particles along the scanned line. The boxed region in Fig. 5-2a corresponds to a background sample region to determine baseline signal for elemental mapping.

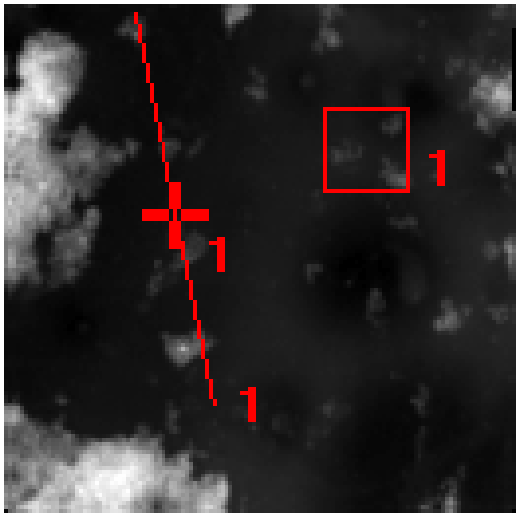

Figure 5-2 Line Scan Elemental Analysis Region

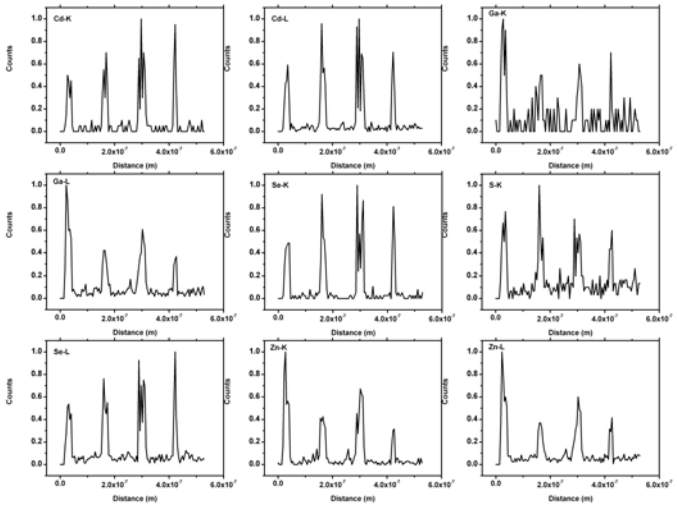

Figure 5-3 Elemental Signals of Cadmium, Gallium, Selenium, Sulfer and Zinc Along the Line in Figure 5-2

Absorbance and photoluminescence plots of the final products are presented in Figure 5-3. Undoped CdSe core-shell particles exhibit a sharp, well defined absorbance peak at ~2.3 eV. Gallium doped particles display less well defined absorbance features at ~2.23 eV, 2.21 eV, and 2.02 eV for 2.5, 5.0, and 10 % dopant loads respectively. This pronounced red-shift in the $1S_e$-$1S_h$ transition is the result of increasing core size observed in the HR-TEM images presented in Figure 1. The trend of core size increasing with the amount of dopant added to the reaction is consistent with previous results obtained from indium doping studies, indicating that doping activates the CdSe core for growth.[70] Table 5-1 summarizes the particle dimensions based on HR-TEM measurements and CdSe core diameters obtained by effective bandgap calculations.

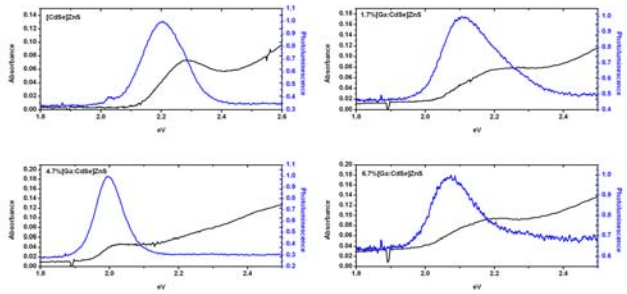

Figure 5-4 Absorbance and Photoluminescence Spectra of Gallium Doped Quantum Dots

Table 5-1 Particle Size Data for Gallium Doped Quantum Dots Obtained from HR-TEM and Bandgap Calculations

Gallium Load (%)	E_g (eV)	D_{CdSe} (nm)	ZnS Shell (nm)
2.5	2.23	3.04	0.63
5.0	2.21	3.11	1.0
10.0	2.02	4.04	1.0

The most notable feature of the fluorescence spectra in Figure 5-4 is the broadness of the PL peak. Undoped CdSe, 2.5, and 5.0 % Ga doped all show a significant tail into the blue region of the spectrum. This feature can safely be assumed to be caused by a significant population of core particles slightly smaller than the main size family rather than by trap emission which is characterized by tailing into the red region of the spectrum.

Previous studies on indium doped CdSe grown with the $Li_4[Cd_{10}Se_4(SPh)_{16}]$ single source precursor at low temperatures showed that the reaction solution contains two families of CdSe particles: a magic size nanocluster (MSNC) characterized by a narrow emission peak at 460 nm and a larger family of particles that originates from the MSNC and continues to grow following traditional colloidal growth mechanisms (continuous non-stepwise growth and size

focusing followed by defocusing or Ostwald Ripening). This novel growth has been dubbed the "heterogeneous growth regime," and is represented in Figure 5-5 for undoped CdSe quantum dots.

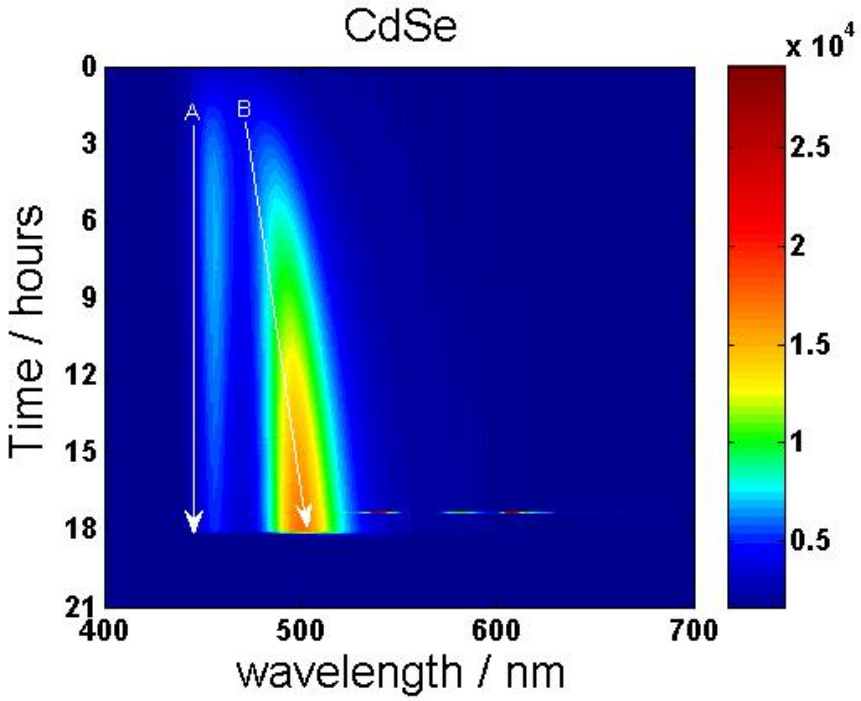

Figure 5-5 Two Dimensional Plot of Quantum Dot Fluorescence in the Heterogeneous Growth Regime

In this growth model, the MSNC signal appears at 460 nm and increases in intensity for some time while a second peak attributed to the larger particle grows out of the MSNC peak. The MSNC begins to dissolve providing monomer for the larger particle to grow. Doping CdSe with indium is shown to increase the rate of dissolution of the MSNC and increase the rate of size focusing in the larger particle. It followed that it should be possible to track similar changes using gallium as the dopant atom.

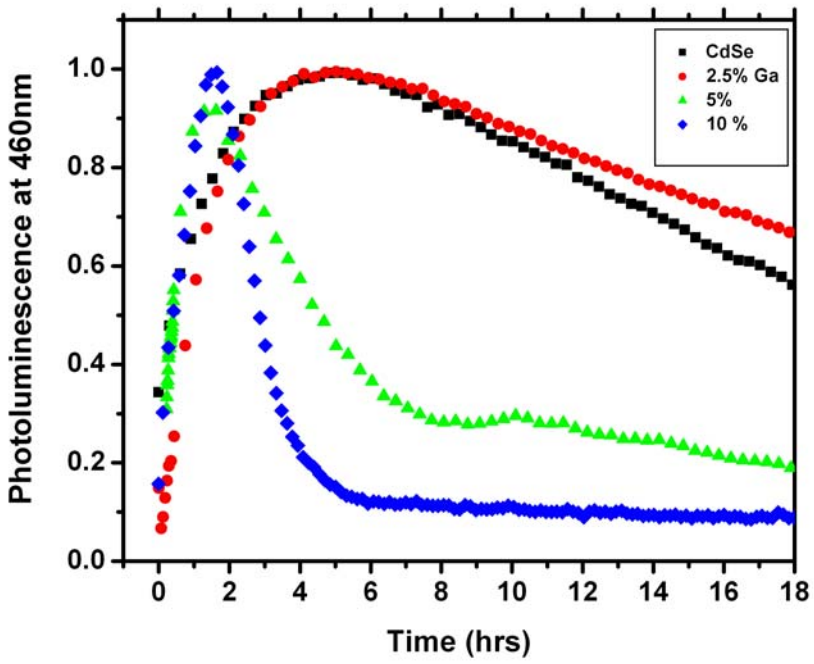

Figure 5-6 Photoluminescence of Magic Size Nanocluster at 460 nm Over Time

The photoluminescence of the MSNC at 460 nm during synthesis with different amounts of gallium added is shown in Figure 5-6. CdSe quantum dots grown without gallium chloride present reach a maximum emission at ~5 hours. CdSe QDs grown with 2.5 mol % relative to Cd also reach a peak emission at this time, indicating that low concentrations of gallium do not effect the consumption of the MSNC. This lack of influence can possibly be explained by side reactions in which the Ga^{3+} interacts with coordinating ligands and anionic species in the reaction, leaving few dopant atoms to interact with the MSNC. In both cases once maximum emission is reached the decline in intensity is slow, with over half of the maximum intensity present at 18 hours when the low temperature growth portion of the synthesis is terminated and the temperature is increased. This is believed to arise from the Cl^- stabilization effects observed when NaCl was added as a check in our previous work with indium doping.

Higher concentrations of $GaCl_3$ do show increased consumption of the MSNC as evident by the 5 % and 10 % synthesis in Figure 4b showing maximum emission at ~2 hours followed by rapid decline in signal intensity as the MSNC is consumed to provide monomer for the "classic" quantum dots. In these cases less than 20 % of the maximum signal is observed at the end of the low temperature segment of the synthesis.

Combining data from Figures 5-4 and 5-6 it is easy to see that the synthesis with the most signal from the MSNC at the end of the low temperature phase have the most broadening in their PL peaks with the heavy emphasis on the emission from slightly smaller particles. Both the 2.5% and 5.0% gallium doped samples display significant contributions in the blue region as well as have the most MSNC signal (undoped CdSe particles excluded). The 10% sample does not display this blue contribution in their final product emission profiles and have final MSNC emission intensities of ~10% of the maximum emission. This trend indicates that the MSNC will act as a growth center during high temperature growth instead of a monomer source, which leads to a polydisperse product with a significant population of particles slightly smaller than the main product.

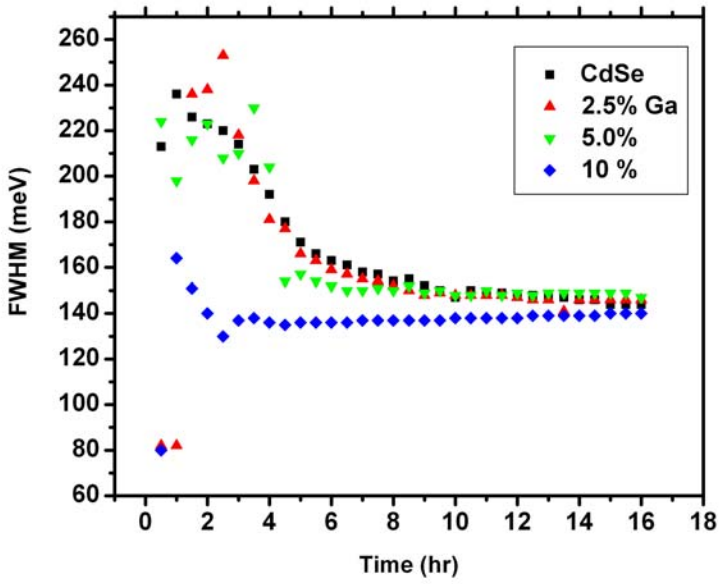

Figure 5-7 Quantum Dot Fluorescence FWHM Over Time

Size focusing data for the larger size particle in the reaction are shown in Figure 5-7. All particles except for the 10% doped sample show a final full-width-half-maximum (FWHM) of 140-150 meV. Similar to data presented in Figure 6 the undoped CdSe particles and the 2.5% gallium doped particles show very similar focusing behavior, both reaching the minimum FWHM range at 10 hours. The 5.0% batche reaches its minimum FWHM at ~6 hours while the 10% doped quantum dots reach their minimum at 3 hours. In this case, the more dopant added to the reaction the faster the second size particle reaches a minimum FWHM. It should be noted

that in the early hours of the reaction when the second size particle's PL peak is growing out from the MSNC's PL peak it is difficult for peak fitting software to resolve the two, leading to the inconsistent pattern in FWHM in hours 0-4.

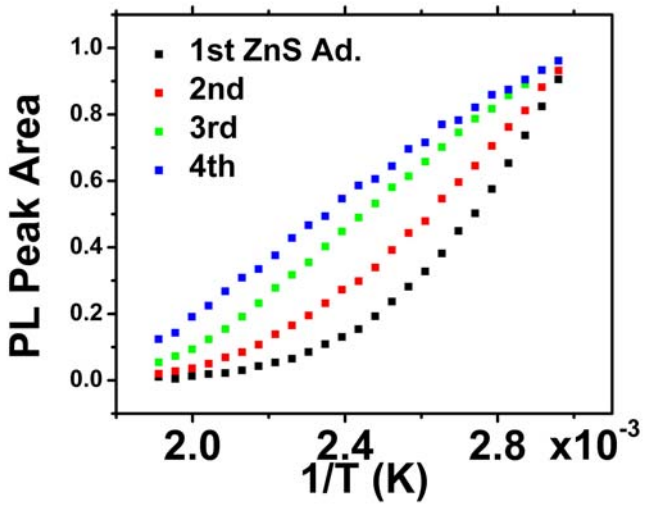

Figure 5-8 Temperature Dependant Photoluminescence of CdSe Quantum Dots from 250 °C to 60 °Cas a Function of ZnS Shell Thickness

Figure 5-8 presents data concerning the effects of ZnS shell thickness on the photoluminescent properties of undoped CdSe@ZnS particles from 250°C down to 60°C. Initially the quantum dots show an exponential relationship between temperature and and-edge emission. This is attributed to surface defects caused by an incomplete ZnS shell. Subsequent injections of Zn/S stock solution complete the ZnS shell and the relationship between temperature and photoluminescence is linear. Once the relationship between temperature and photoluminescence becomes linear the CdSe core has become passivated and any changes in emission properties cannot be the result of surface traps.

Table 5-2 Gallium Content of Quantum Dots Determined from Wide Area EDS

Synthetic Dopant Load (%)	% Ga
2.5	1.7
5.0	6.4
10	4.7

Table 5-2 lists the gallium content of doped quantum dots determined by comparing the ratios of the Cd-L and Ga-L EDS emission peaks taken on a Field-Emission Scanning Electron Microscope (FE-SEM). The heterogeneous growth dynamics of gallium doped quantum dots are dependent on the concentration of dopant in solution. However the electronic properties of doped quantum dots are related to the actual gallium content of the particles. Therefore from this point forward particles will be referred to by their gallium content determined from these ratios instead of the concentration of gallium in solution.

Once the surface of the particles are encased in the thick shell more detailed experiments were carried out in a temperature region were the relationship between temperature and photoluminescence intensity appeared to be linear. From Figure 5-8 the relationship between temperature and photoluminescence appears to be linear below 100°C. 2-amino-propanol (APOL) was selected as the solvent for several reasons: first, APOL has freezing, flash, and boiling points well outside the region of investigation.

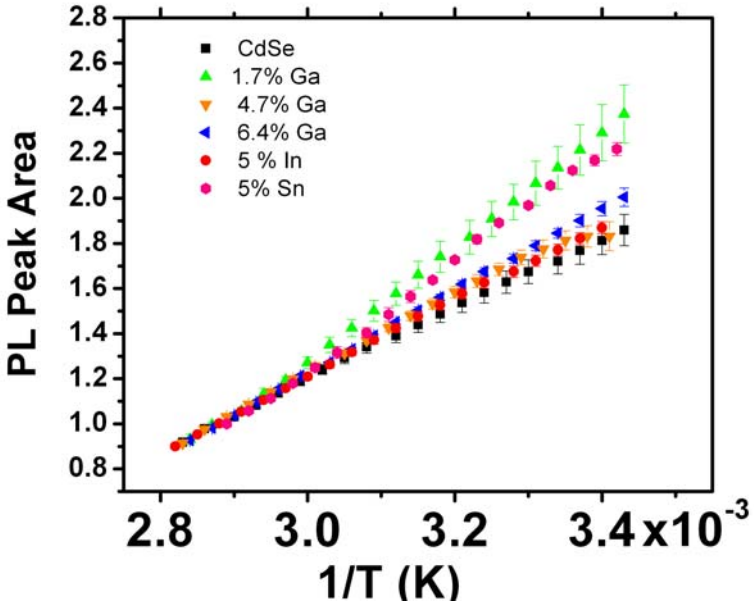

Figure 5-9 Temperature Dependent Fluorescence of Quantum Dots in APOL from 80 °C to 10 °C

Figure 5-9 shows the temperature dependant photoluminescence profile of CdSe@ZnS particles dispersed in 1-amino-2propanol (APOL) between 10°C and 80°C. The 1.7 % gallium doped line show significant departure from the undoped CdSe line beginning at 1/T = ~0.0030

which is ~57 °C. This sudden onset of fluorescence indicates that at 57 °C the gallium atoms in these particles are able to ionize into the conduction band and begin quenching band-edge emission.[90] The 6.4 % and 4.7 % lines deviate slightly from the undoped line indicating that these dopant donor levels are less accessible to the conduction band in this temperature range; or that the particles are saturated with dopant atoms and their donor states have begun to overlap with the conduction band. 5% tin and 5% indium doped (CdSe)ZnS quantum dots were also examined in this temperature region. Tin doped quantum dots show significant deviation from undoped quantum dots while indium doped quantum dots show only a slight deviation. Previous work has determined that indium donor levels lay 280 meV below the conduction band whereas tin donor levels are 100 meV below the conduction band.[71] The 1.7 % gallium line begin to deviate from the undoped line before the tin doped quantum dots, indicating the donor levels are lower in energy.

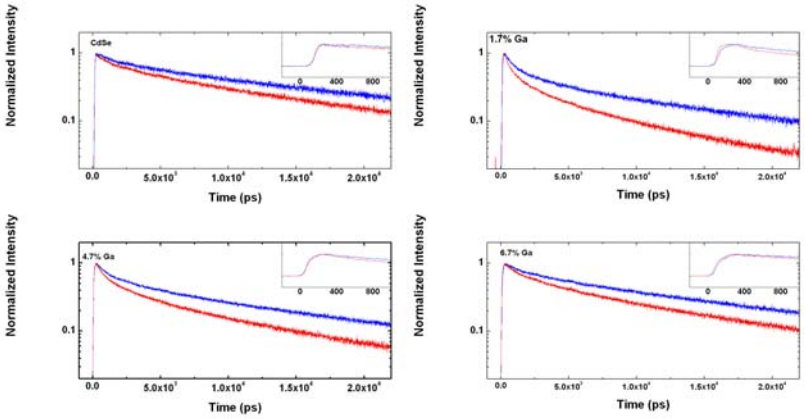

Figure 5-10 Time-Resolved Fluorescence of Gallium Doped Quantum Dots

Time-resolved spectroscopy results at 80 °C and 20 °C are presented in Figure 5-10 and fluorescence decay fitting parameters are listed in Table 5-4. Beginning with undoped (CdSe)ZnS core shell quantum dots at room temperature both the long and short lifetimes (τ_1 and τ_2 respectively) are in line with accepted literature values for core-shell particles.[122] Ideally, core

shell quantum dots should possess only a single decay parameter on the order of 20-30 ns indicative of radiative exciton recombination, however the core-shell interface introduces a defect zone allowing for fast carrier recombination. Increasing the temperature to 80 °C causes a small decrease in both τ_1 and its contribution, which can be explained by increased phonon population. At the same time τ_2 increases both in duration and contribution. The increase in contribution can be explained by increased disorder at the material interface.

Table 5-3 Fluorescence Decay Time Components and Amplitudes for Gallium Doped Quantum Dots

Sample (Temp)	τ_1 (ns) [+/-]	%	τ_2 (ns) [+/-]	%	τ_3 (ns)	%
CdSe (RT)	19.19 [0.42]	92.9	2.54 [0.01]	7.1	-	-
CdSe (80 °C)	18.49 [3.65]	88.2	3.8 [3.2]	11.8	-	-
1.7% (RT)	11.96 [1.2]	87.0	1.16 [0.4]	13.0	-	-
1.7% (80 °C)	9.11 [0.99]	67.9	2.3 [0.11]	22.5	0.47 [0.01]	9.6
4.7% (RT)	8.56 [0.37]	93.0	0.68 [0.27]	7.0		
4.7% (80 °C)	7.38 [0.68]	86.2	0.93 [0.15]	13.8	-	-
6.4% (RT)	8.43 [3.5]	100	-	-	-	-
6.4% (80 °C	7.7 [0.25]	94.6	0.65 [0.42]	5.4	-	-

All gallium doped samples show significantly decreased τ_1 and τ_2 times compared to undoped quantum dots at room temperature. Upon heating τ_1 decreases further but the magnitude of change is on the order of the reduction of τ_1 for undoped particles, and can also be explained by increased phonon population. However, the drastic reduction of τ_1 upon the

incorporation of gallium indicates that the gallium atoms in the CdSe host act as fast recombination centers for the electron-hole pair.

A third decay constant is needed to fit the 1.7% curve at 80 °C and is included as τ_3 in Table 5-4. The presence of this third decay constant is believed to originate from ionized donor electrons introducing an Auger process.[90] An Auger relaxation mechanism is an acceptable framework since by convention ionized donor electrons in bulk n-type semiconductors do not create a positively charged atom behind, rather the dopant atom is now viewed as iso-electronic with the host lattice. The presence of an Auger relaxation is further supported by the data in Figure 5-9, where at ~57 °C the band-edge fluorescence of the 1.7% gallium doped particles begins to "switch on" and the particles become more fluorescent as temperature decreases, indicating that the dopant electron is no longer ionized into the conduction band energy levels and normal electron-hole relaxation dominates. The absence of τ_3 at room temperature also supports this mechanism. The absence of τ_3 in samples of higher gallium content can be explained as deep traps caused by increasing disorder in the lattice.

Discussion

It is clear from the combined microscopy data that CdSe quantum dots have successfully been doped with gallium. The line scan elemental analysis in Figure 5-2 clearly shows that gallium K- and L-line signals correspond to the locations of particles along the line scan. Due to instrumental limitations, only 2D rendering is possible, making impossible at this time to separate gallium atoms located in the core and any that may be incorporated into the ZnS shell material.

In order to explain the different fluorescence quenching behaviors of the gallium doped quantum dots two separate possibilities must be considered: "compensation" and self-purification. The phenomenon of "compensation," where the quantum dot crystal forms defects that counter act the n-type donors to bring the Fermi Energy of the particle back to its natural value,[72] may be occurring in heavily doped quantum dots (4.7 % and 6.4 %) but not in lightly doped (1.7 %). In this process, the quantum dot lattice will form p-type defects to lower the energy of the n-type donors provided by gallium. This could explain why the heavier doped samples do not display the same temperature dependent fluorescence properties, since

compensation would lower the energy level of the donor electrons and previous work has shown that the temperature dependent fluorescence quenching in n-type doped quantum dots is related to the donor level's energetic distance from the 1S conduction band energy level.[71]

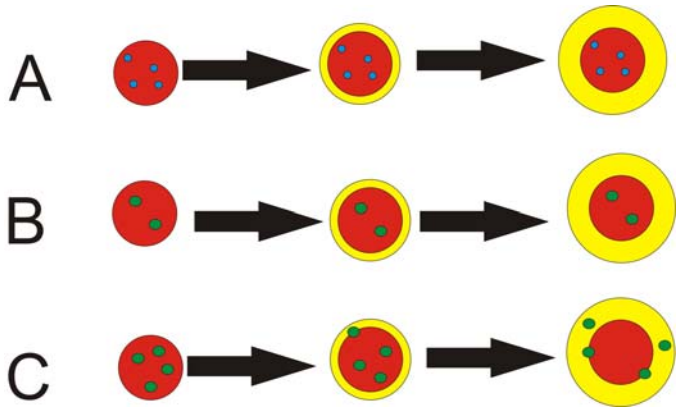

Figure 5-11 Self-Purification Model of Quantum Dot Doping

In Figure 5-11, a self-purification model is proposed based on cation radius mis-match in the CdSe host lattice. Gallium has a cationic radius roughly 20% smaller than cadmium, while dopants like indium and tin are 9% and 5% larger respectively. In Figure 5-11a dopant atoms with small size mismatches such as indium and tin are represented by the blue dots. Due to the small size mismatch, these dopant atoms do not destabilize the CdSe lattice and are not ejected into the ZnS shell material. When the cation mismatch is large, such as in the case of gallium, small numbers of dopant atoms are tolerated inside the CdSe core; they do not destabilize the host lattice and are not ejected into the shell material as shown in Figure 5-11b. Higher loads of dopant atoms destabilize the quantum dot core and as the ZnS shell grows the dopant atoms begin to migrate into the ZnS shell where, in the case of gallium, there is a more favorable cation mismatch (5-11c). .

The heterogeneous growth kinetic data suggests that gallium doping does affect CdSe growth. Because the amount of dopant added to the synthesis has little effect on magic-sized nano-cluster consumption or the size focusing of the larger "classical" quantum dot in solution, it can be concluded that very little dopant is needed to accelerate growth. A very large cation mismatch present in the case of gallium doping will increase the free energy of the quantum dots, and only a small number of dopant atoms are required to activate the particles for growth to a larger size where surface relaxation can stabilize the particles and counter-act the lattice strain.

The temperature dependant photoluminescent properties (Figure 6) also support the self-purification model proposed in Figure 5-9. The 1.7 % doped sample significantly deviates from the pristine (CdSe)ZnS particles. In the 1.7 % sample, the number of dopant atoms is sufficiently low to not induce self-purification. The gallium atoms remain inside the CdSe core and are efficiently ionized into the $1S_e$ energy level in the conduction band. The 4.7 % and 6.4 % samples show less dramatic temperature dependant fluorescence properties because some or all of the dopant atoms have been pushed either into the ZnS shell or to the core-shell interface where dopant atomic orbitals do not overlap as efficiently with the QD's $1S_e$ orbital.

The temperature dependant time-resolved fluorescence data in Figure 5-10 and Table 5-4 provides additional support for this mechanism of self-purification. When the dopant atoms are confined to the core of the particle, as they are in the 1.7 % doped sample, where ionization of donor electrons is more efficient and an Auger process is introduced. Because the ionization is more efficient, this process is observable at lower temperature compared to tin or indium donor ionization and becomes more pronounced at elevated temperatures as more donor electrons are ionized into the conduction band. This accounts for the increased contribution from the fast relaxation component in Figure 5-11c. At higher concentrations (4.7 % and 6.4 %in Figure 5-11c) where some dopant atoms may have migrated to the shell material interface there is still significant fast relaxation at room temperature and less pronounced increase at higher temperature.

Conclusion

CdSe quantum dots have been successfully doped with gallium and several novel analytical techniques have been developed to determine the effects gallium doping has on the electronic properties of doped QD's. Single quantum dot EDS preformed through TEM supports the incorporation of gallium into the particles on a per particle basis. Novel temperature dependant photoluminescence studies support a self-purification mechanism where dopant atoms are ejected from the CdSe core due to a large host cation size mismatch. Low dopant concentrations have pronounced effects on photoluminescent properties due to efficient ionization of donor electrons into the quantum dot conduction band including the introduction of a third charge carrier recombination pathway at elevated temperature. Higher concentrations show less dramatic effects because dopant atoms have migrated to the core-shell interface or into the ZnS

shell. Additional work is needed to determine the exact locations of the dopant atoms inside the core-shell particles. 3D elemental analysis techniques should be applied in the future to solve this problem.

Doped quantum dots will play an important role in the development of future devices. While CdSe possesses several undesirable traits, it remains the most studied 0D-quantum confined system prepared by traditional chemical routes and will continue to play an important role in understanding doped quantum dot properties and applications. The data presented above indicates that gallium doping brings CdSe one step closer to true n-type semiconductor behavior, a necessary property for device construction.

Chapter 6 - Improved Conductivity in Thin Films of Indium and Tin Doped CdSe Quantum Dots

Introduction

The size dependent optical properties,[4] ease of synthesis,[18, 123] bright fluorescence spectra[16, 19] and shape control[23, 37, 39] have made quantum dots a popular research area over the past twenty years. Doping quantum dots by deliberately introducing foreign atoms into the host lattice will introduce novel properties allowing quantum dots technology to be applied to a wide range of devices.[94] However, doping quantum dots has proved difficult[74, 82] and the vast majority of reports of doping quantum dots have focused on incorporation of transition metal dopants for magnetic purposes.[75, 85, 95, 118, 119]

Due to the high absorption cross section of quantum dots[100] and the slow relaxation of carriers in the conduction band[43] CdSe quantum dots have been proposed as light harvesters in the widely popular dye sensitized solar cell (DSSC) pioneered by the Grätzle group.[49] Currently, the reported efficiencies of DSSC's sensitized with quantum dots is below 5%.[8] If quantum dots can be successfully doped with n-type donor atoms that provide extra electrons to the conduction band this efficiency can hypothetically be increased, as the donated electrons will increase the photocurrent in the cell. Recent reports of doping CdSe quantum dots with indium[70, 71] and tin[71] suggest that the introduction of these impurities introduce n-type electron donors as they have in bulk CdSe.[86-88]

In order to determine if indium and tin doped quantum dots could be used to this end, it is necessary to determine if they do in fact have extra electrons that will be donated to the conduction band. This can be accomplished through simple source-drain circuitry. The Guyot-Sionnest group has shown that the conductivity of CdSe quantum dot charged with sodium biphenyl is higher than that of regular CdSe quantum dots.[91] Several other reports indicate that the conductivity of quantum dot thin films is strongly dependent on the inter-particle surface contact, and that conductivity improves as the particles are brought into closer contact with one another.[124, 125]

In the following sections the results of source-drain CdSe quantum dot thin film conductivity will be described and discussed. Indium and tin doped CdSe quantum dots do show

one to two orders of magnitude higher conductivity than undoped quantum dots. Data will also be presented that shows doped quantum dots whose surface ligand chemistry have been changed show higher conductivity.

Experimental

Chemicals: Hexadecylamine is distilled at ~2 torr and stored on the shelf. $Li_4[Cd_{10}Se_4(SPh)_{16}]$ is prepared according to the Dance[29] and Cumberland[28] procedures. Tributylphosphine oxide, pyridine, acetonitrile, and thiolglycolic acid are used as is. Indium and tin chloride are stored in a glovebox under nitrogen atmosphere. Pt interdigitated electrodes are obtained from Synkera Technologies.

Synthesis: CdSe quantum dots and indium or tin doped CdSe quantum dots are synthesized as follows: 25 g of hexadecylamine is loaded into a three neck flask with 0.3 g of $Li_4[Cd_{10}Se_4(SPh)_{16}]$ and then passed into the glovebox where 5 mol % relative to cadmium of metal chloride ($InCl_3$ and $SnCl_2$) is added. The flask is sealed and brought into the lab where it is purged on an Ar line for 10 minutes. The flask is slowly heated to 120 °C and stirred for 18 hours while fluorescence spectra are recorded to monitor heterogeneous growth kinetics. The temperature is then increased to 240 °C for three hours. The reaction is then cooled to room temperature and the crude material is stored and purified immediately before use. Surface ligand exchanges are preformed by dissolving 2 g of crude material in 10 mL of toluene and precipitating with methanol. For tributylphosphine oxide (TBPO) the quantum dots are resuspended in 10 mL of toluene and stirred overnight with 3 g of TBPO. For pyridine ligand exchange the precipitated quantum dot were resuspended in 10 mL of pyridine and stirred over night.

Electrode Preparation: Pt interdigitated electrodes are cleaned in a mixture of H_2SO_4 and hydrogen peroxide overnight. They are then extensively rinsed with ultrapure water to remove residual acid and then rinsed once with acetone. The working face of the electrodes is dipped into a solution of 10% acetonitril/90% thioglycolic acid overnight to functionalize the electrode surface to ensure good quantum dot attachment. The functionalized electrode surface is dipped into a solution of quantum dots in chloroform using a programmable dip coater. Quantum dot coated electrodes are dried for ~30 minutes under nitrogen atmosphere before testing with Dri-Rite in the chamber to absorb water vapor.

Conductivity Measurement: Quantum dots coated electrodes are attached to a gold plated copper clip which is wired into a potentiostat. Five half sweeps between the determined voltages are preformed. For dark measurements, the lights in the room are turned off and the test chamber is covered with dark fabric to shield from other light sources as well. The electrode is left in the dark for fifteen minutes under nitrogen flow before readings are collected. For light measurement the dark fabric is removed and the overhead lights are turned on for five minutes before reading are taken.

Results

Doped and undoped quantum dots are synthesized without a ZnS shell to prevent the ZnS shell from confining the electrons to the core and impeding conductivity. After dip coating the electrode surface is a uniform dark red indicating good particle coverage. As a preliminary check, an electrode covered in undoped quantum dots is tested in air. The same electrode is cleaned and coated in indium doped quantum dots and tested in air. The results are shown in Figure 6-1:

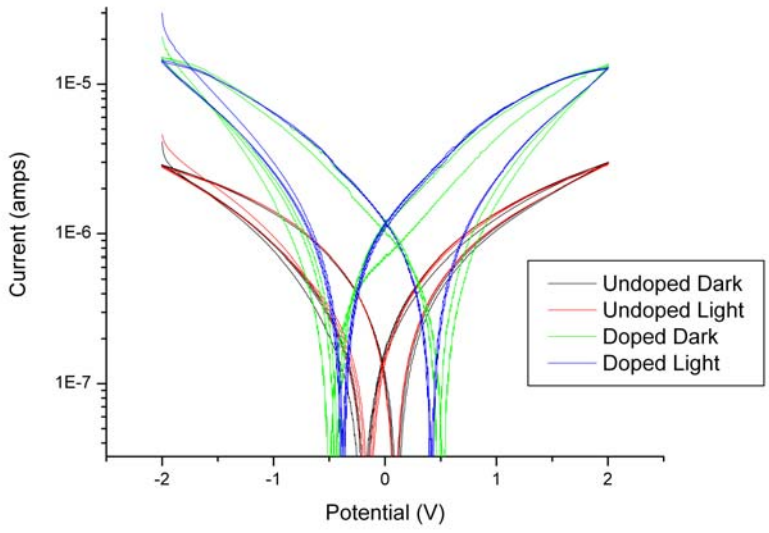

Figure 6-1 Conductivity of Indium Doped and Undoped Quantum Dots

In this case the particles are coated in hexadecylamine and have not had their surfaces altered in anyway save for attachment to the TGA coated electrodes. Under both light and dark

conditions the indium doped CdSe quantum dot film conductivity is roughly an order of magnitude higher than the undoped CdSe quantum dot film.

As mentioned in the introduction, several reports show that the conductivity of CdSe films is strongly dependent on the interparticle contact. To invensitage this, CdSe quantum dots and both indium and tin doped CdSe quantum dots had their hexadecylamine ligands exchanged with pyridine. Pyridine is a much smaller molecule than hexadecylamine and will allow much greater inter-particle contact as the aromatic ring of pyridine is much shorter than the 16 carbon aliphatic chain of hexadecylamine. The results of this experiment are shown in Figure 6-2

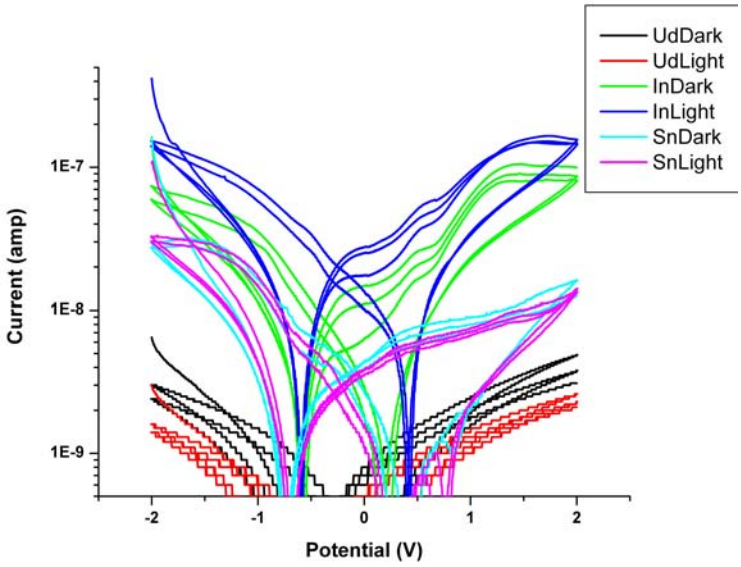

Figure 6-2 Conductivity of Pyridine Capped Quantum Dots

Pyridine capped quantum dots are sensitive to photodegridation over long periods of illumination. Therefore pyridine capped quantum dots had their conductivities measured under nitrogen flow to prevent this. In Figure 6-2 it is clearly seen that both indium and tin quantum dots have higher conductivites than CdSe quantum dots. The step-wise nature of the undoped CdSe quanum dot lines is a result of the sensitivity settings of the potentiostat. Tin doped quantum dots show both dark and light conductivity one order of magnitude higher than undoped quantum dots (light plue and purple lines). Indium doped quantum dots show dark and light conductivity an order of magnitude greater than tin doped quantum dots and two orders of magnitude greater than undoped quantum dots (blue and green lines). Additionally, indium doped quantum dots show increased current under illumination (blue line) consistent with the data in Figure 6-1.

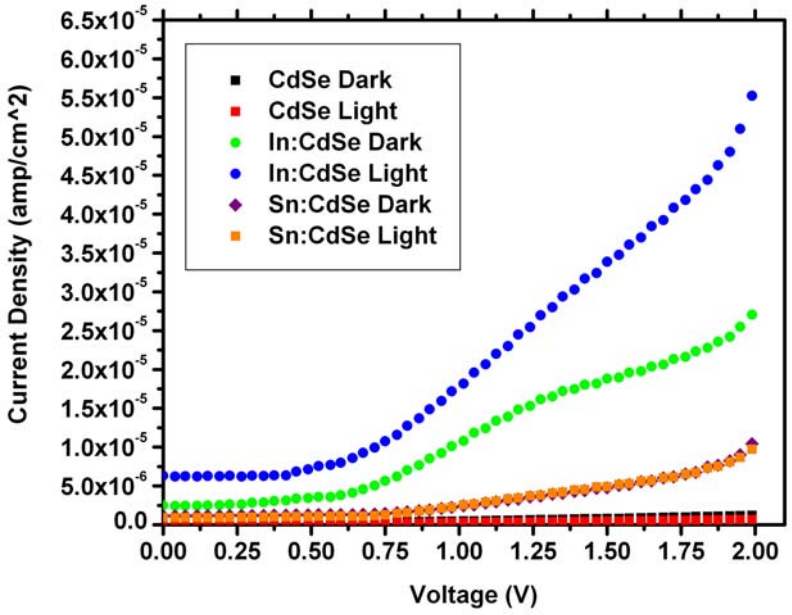

Figure 6-3 Current Densities of Indium, Tin, and Undoped CdSe Quantum Dots Capped with Pyridine

The currents measured n Figure 6-2 were normalized by dividing the current by the electrode area (0.003 cm) and plotted in Figure 6-3. Following this treatment of the data it truly becomes clear that doping quantum dots greatly increases their conducitivty. While tin doped quantum dots show slightly increased current densities and no light response (the purple diamonds are obscured by the orange stars) the indium doped quantum dots show light response even at 0 V applied potential. This indicates that under ambient conditions there are significant numbers of mobile electrons in the conduction band moving from particle to particle and through the closed circuit under illumination. The current densities of indium doped quantum dots remain roughly an order of magnitude higher than tin doped dots, consistent with the simple I-V measurements shown in Figure 6-2. However under illumination the current density of indium doped quantum dots is over twice that of indium doped dots in the dark.

Discussion

It is clear from Figures 6-2 and 6-3 that indium and tin doped CdSe films have higher conductivity than films of undoped CdSe quantum dots. Indium doped quantum dots also show a light response as indicated by higher photocurrents than those produced under dark conditions.

Conductivity measurements reported in the literature are often collected in high vacuum and at low (liquid nitrogen or lower) temperatures to eliminate oxygen and water vapor than could damage the quantum dot film. Our system represents a much milder set of conditions and yields good results.

N-type donors in bulk semiconductors have very weak electron binding energies on the order of tens of millielectron volts. When the thermal energy (k_BT) begins to approach those values the donor electrons begin to ionize into the conduction band. The experimental set-up in Figure 6-1 was modified to allow helium gas to be cooled to liquid nitrogen temperatures by insulating the test chamber an submerging the chamber and zeolite coil in liquid nitrogen. The conductivity of the quantum dot films is measured as the set-up slowly warmed up to room temperature in an effort to determine at what temperature the donor electrons can no longer ionize into the conduction band. No good results were obtained, I-V curves collected in this manner showed immeasurable current or mili-amp current levels from water vapor condensing on the electrode surface.

In an effort to further improve inter-particle contact, quantum dots were subjected to ligand exchange with the $Sn_2Se_6^{2-}$ ligands reported by Kovalenko.[124] The tin selenate ligand was successfully synthesized by dissolving tin and selenium powders in anhydrous hydrazine according the reported color changes. Quantum dots are successfully surface exchanged with the new ligand, as the heptane suspended quantum dots quickly moved into the hydrazine phase leaving a colorless organic layer. However, when trying to attach the tin selenate functionalized quantum dots to the Pt electrode the hydrazine vapors reacted with the copper clips holding the electrodes. The resulting tarry bi-product ruined the electrodes.

Conclusion

Doping CdSe quantum dots with indium and tin does increase the conductivity in thin films composed of quantum dots. Tin doped quantum dots with pyridine surface ligands show a ten fold increase in conductivity over undoped quantum dots. Indium doped quantum dots show a one hundred fold increase over undoped quantum dots. In addition, indium doped quantum dots display light sensitivity with higher current values under overhead illumination than in the dark.

Chapter 7 - Blue Shift in Transient 1S Bleach in Indium Doped CdSe Quantum Dots

Introduction

Quantum dot research has emerged as a dominating field due to the size dependant optical properties[18, 123] bright and narrow fluorescence profiles,[16, 17, 19, 20] and ease of shape control.[23, 37, 126] Doping, intentionally adding small amounts of an impurity atom, provides another route for tailoring the electronic properties of quantum dots[94]. Currently, most research on doping quantum dots has focused on incorporating transition metals such an manganese[75, 95] or cobalt[79, 95] to introduce magnetic responses. CdSe quantum dots have also been electrochemically doped, or charged, by electron injection from a strong reducing agent.[90, 91] Recently the Banin group reported doping III-VI quantum dots with silver, gold, and copper creating n-type and p-type band structures. Very few reports exists concerning doping CdSe quantum dots with elements such as indium[70], tin[71], or gallium[127] which have been shown to improve conductivity in bulk CdSe[84, 89], CdSe thin films[86, 88], and CdSe nanowires.[72]

Doping CdSe quantum dots with indium, tin, and gallium significantly alters the growth dynamics in the "heterogeneous growth regime."[70, 71, 127] Gallium and tin doped quantum dots also showed strongly temperature dependent fluorescence quenching due to partial ionization of n-type donor electrons.[127] However the intraband electronics of doped CdSe quantum dots remains a mystery. Of particular interest are the intraband relaxation dynamics in the conduction band and how the donated electron alters them. Transient Absorption (TA) spectroscopy has proven a valuable tool for exploring the electron relaxation dynamics in the conduction band of CdSe quantum dots.[43, 46, 128] Klimov and co-workers have identified both Photoinduced Absorption and Photobleaches corresponding to the 1S, 2S, and 1P electron levels in CdSe quantum dots; and were able to determine the relaxation times for electron dropping from the 2S and 1P levels down to the 1S are 300 fs.

Quantum dots have been proposed as substitutes for the ruthenium dyes in TiO_2 sensitized solar cells.[49] In-depth work by the Kamat group has shown through TA spectroscopy that CdSe quantum dots show rapid electron injection into TiO_2 structures[8] and carbon nano-cups.[48] Tvrdy et. al showed that the rate of electron injection from the quantum dots is strongly

dependant on the energy off-set between the conduction bands of the quantum dot and the transparent conducting oxide material.[51] N-type doped quantum dots have the potential to increase the efficiency of Quantum Dot Sensitized Solar Cells (QDSSC) through ionization of donor electrons into the conduction band. TA spectroscopy is a powerful tool to examine the electron dynamics of n-type doped systems. The data presented shows that CdSe/ZnS quantum dots doped with indium show an ~70 meV blue shift in the transient bleach of the 1S absorption feature compared to undoped CdSe/ZnS quantum dots.

Experimental

Chemicals: Hexadecylamine (HDA) and tri-n-octylphosphine (TOP) are distilled at ~2 torr. All other chemicals are used as is. $Li_4[Cd_{10}Se_4(SPh)_{16}]$ is synthesized according to literature procedures.[28, 29] A Zn/S stock solution is made according to the method reported by Hines by mixing 7 ml of diethyl zinc with 1 mL of hexamethyldisilithiane and 32 mL of distilled TOP.

Synthesis: Indium doped CdSe quantum dots were synthesized according to a modified synthesis reported by Magana[80] with $InCl_3$ used as dopant source. Briefly, 50 g of distilled HDA, 0.6 g of $Li_4[Cd_{10}Se_4(SPh)_{16}]$ and 5 mol % $InCl_3$ with respect to cadmium are loaded into a three neck flask and purged under Ar flow for 10 minutes. The flask is slowly heated to 120 °C and then stirred for 18 hours. The temperature is increased to 240 °C for three hours after which the temperature is again increased to 250 °C while 2 mL of Zn/S stock solution diluted with 8 mL of distilled TOP is added dropwise via automated syringe pump. The ZnS shell is grown for one hour. After ZnS shell growth is complete the core shell particles are subjected to annealing cycles as described previously.[127] After annealing is complete another Zn/S injection is preformed at 250 °C followed by annealing. This process is repeated for a total of 4 Zn/S injections. Undoped CdSe particles are grown according to this process with the $InCl_3$ being omitted. Particles are purified via suspension of crude product in toluene and precipitation with methanol.

Transient Spectroscopy: Transient absorption data is collected with specific hardware/software designed by Ultrafast Systems (Helios) which is coupled to a Clark•MXR 2010 (775 nm, 1 mJ/pulse, fwhm = 130 fs, 1 kHz repetition) laser system. The pump and probe are incident on a quartz 2 mm path length sample holder at an angle <10˚, and the probe is spatially filtered between the sample and collection optics to minimize collected signal from

emissive samples. The pump is operated at 95% of fundamental with frequency doubled to 387 nm, and the probe at 5% of fundamental to generate a white light continuum. Typically 1000 excitation pulses are averaged to obtain a transient spectrum at a set delay time. All experiments are performed at room temperature.

Results

The absorbance spectrum of undoped and 5 mol % indium doped CdSe/ZnS core-shell quantum dots are shown as solid blue lines in Figure 7-1 and 7-2 below. Both doped and undoped core-shell particles display good peak-to-valley structure at the 1S band-edge, indicating a narrow size distribution. Indium doped quantum dots have an absorbance peak red shifted from undoped dots (548 nm vs 532 nm), indicating a slightly larger core radius which is consistent with previous results.[70]

Fluorescence spectroscopy of the same samples support CdSe cores well passivated with ZnS. Neither sample shows weak emission red shifted from the band-edge peak, supporting a well passivated core with no dangling bonds or surface defects. The undoped quantum dots show a Stokes shift of 12 nm while the indium doped particles have a 9 nm Stokes Shift. Previous studies have showed that doped quantum dots display smaller Stokes Shift due to back-filling of electron levels.[71] The quantum yield of the undoped quantum dots is calculated to be 17% while the indium doped quantum dots have a quantum yield of 36%.

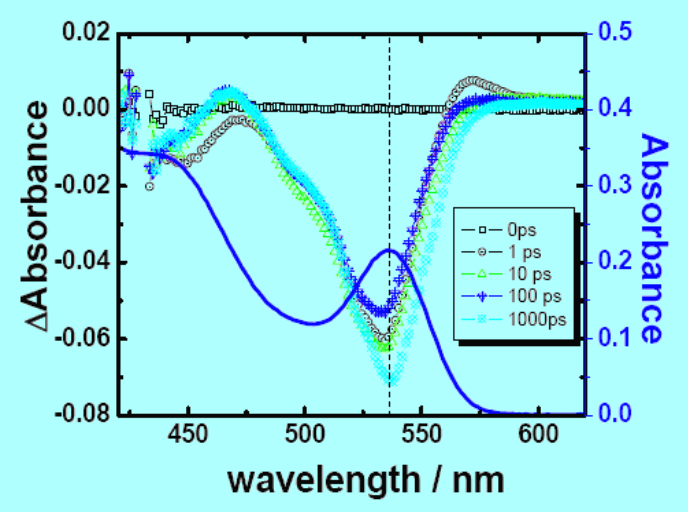

Figure 7-1 Transient Absorption Spectrum of CdSe-ZnS Core-Shell Quantum Dots

The Transient Absorption spectrum of undoped CdSe-ZnS quantum dots in Figure 7-1 display all of the peak signatures common to CdSe quantum dots according to work by the

Klimov group.[43, 44] The Photoinduced Absorption (PA) feature red shifted from the band-edge absorption caused by Coulombic interactions is clearly visible along with the 1S bleach a 532 nm. The shoulder representing the $1S_e$-$2S_{(3/2)h}$ energy level is also visible at ~520 nm along with the 1P bleach at ~450 nm and its associated PA.

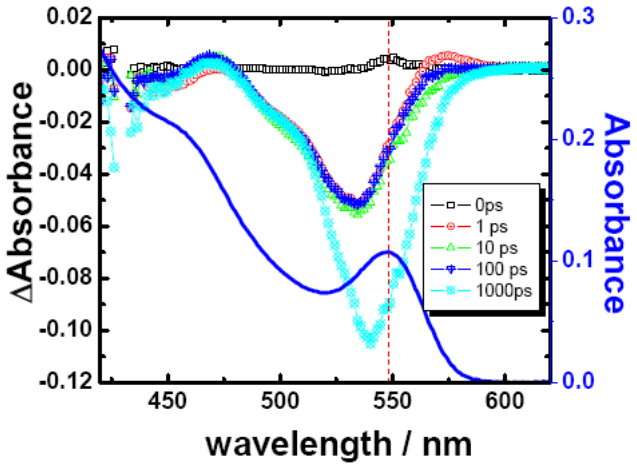

Figure 7-2 Transient Absorption Spectrum of 5 mol% Indium Doped CdSe-ZnS Core-Shell Quantum Dots

The TA spectrum of 5 mol % indium doped quantum dots in Figure 7-2 is startlingly different. While the traditional PA features and higher order electron levels are visible and in similar position to their undoped counterparts, the 1S bleach shows slightly positive absorption at delay t = 0 ps. At delay t = 1 ps the 1S TA peak has blue shifted to ~ 535 nm (~70 meV) and remains 70 meV behind the static absorption peak until some time after 100 ps. By 1000 ps the TA peak has moved to 545 nm. The magnitude of the band-edge TA bleach is also much larger in the indium doped sample than in the undoped sample relative to the static absorbance value. Undoped particles show a 1S ΔA = -0.06 at 1 ps that grows to ~-0.085 by 1000 ps with a static absorption value of 0.2. Indium doped quantum dots show a 1S ΔA = -0.06 at 1 ps as well, however for times up to 100 ps the 1S ΔA remains constant at -0.06 before increasing to~-0.1 at 1000 ps. While these numbers seem similar, it is important to note that the indium doped sample has a static absorbance of 0.1. This difference in optical density between samples indicates that the indium doped samples are almost completely bleached at 1000 ps.

Discussion

The results from Figures 7-1 and 7-2 clearly indicate that a significant change has occurred in the conduction band structure of indium doped CdSe quantum dots. In order to explain the emergence of this new electronic state that couples to the 1S TA peak it is necessary to attempt to rule out plausible explanations. First, this new state cannot arise from alloying of the core and shell as such alloying would manifest itself in the undoped sample as well. Second, transition metal doping of CdSe has been shown to induce Zeeman Splitting in the 1S conduction band level.[95] Following calculations by Archer *et. al*[95] and using a g-factor of 2 for n-type CdSe based on Schrier and Whaley's calculations[129] in order to generate a 70 meV energy difference a magnetic field of over 400 Tesla would be required, which is quite unreasonable. Therefore it can be concluded that this new electron energy level is a direct result of indium incorporation into the quantum dots.

A recent report by the Banin group on doping InAs quantum dots shows that instead of creating donor levels below the conduction band as previously thought, dopant atoms introduce electron levels *inside* the conduction band.[130] In the case of copper doping in InAs, Mocatta *et. al*'s results show that a donor level or band appears *above* the $1S_e$ energy level. If a similar phenomenon is occurring in the indium doped quantum dots studied in this report then the blue shift in the TA spectrum can be explained by a donor level or band that rests 70 meV above the $1S_e$ level and is illustrated in Figure 7-4.

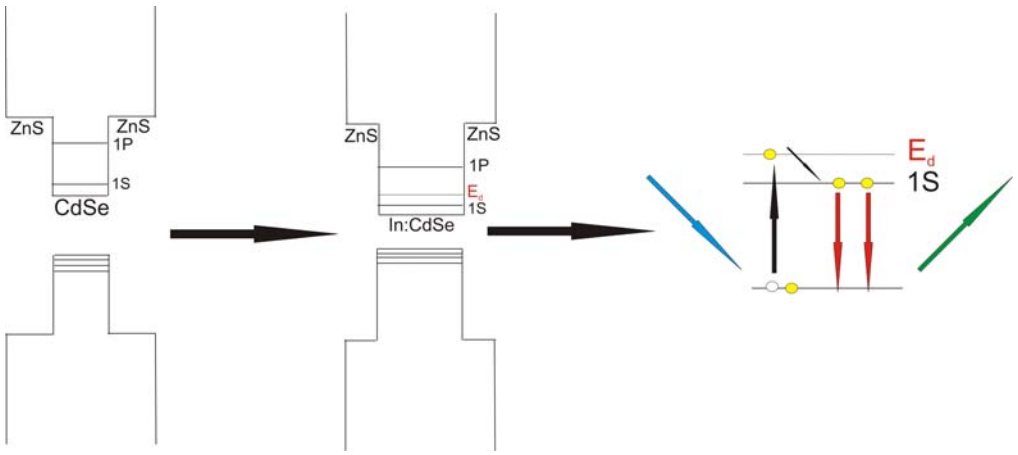

Figure 7-3 Electron Donor Level Located Above 1S Conduction Band State in Indium Doped Quantum Dots and the Resulting Lasing Behavior

The formation of this donor level above the $1S_e$ can also explain the much larger degree of 1S bleaching in the TA spectrum at the same excitation power. In a classical two level system only half of the energy levels are allowed to be populated by optical excitation. This is consistent with the undoped quantum dots where the TA bleach is less than half of the static absorbance. In order to induce TA bleach greater than 50% of the static absorbance a third energy level must be introduced. With this third energy level present, doped quantum dots can be optically excited followed by relaxation down to the 1S state for band-edge fluorescence. This effectively creates a population inversion necessary for lasing. This conclusion is supported by the fact that the indium doped quantum dots studied here have a much higher quantum yield than undoped quantum dots (36% vs 17% respectively) and indium doped quantum dots in previous studies maintain a reasonable quantum yield instead of completely quenching fluorescence (see Table 2 in Chapter 3).

Conclusion

CdSe quantum dots have been successfully doped with indium resulting in high quality core shell particles with narrow absorbance and fluorescence spectrum. Transient Absorption spectroscopy shows that indium doped quantum dots have a unique energy level 70 meV above the $1S_e$ energy level. The presence of this energy state creates a three-level optical excitation system that results in population inversion and indium doped quantum dots having higher quantum yields than undoped quantum dots.

The ability for indium doped quantum dots to generate a population inversion indicates that indium doping creates a high population of conduction band electrons. If this high population of electrons can be quickly removed from the quantum dot conduction band then a new possibility for more efficient quantum dot based solar cells has been found. Certainly these newly found electronic properties will generate applications for quantum dots.

References Or Bibliography

1. Juodkazis, S.; Mizeikis, V.; Misawa, H. *J. Appl. Phys.* **2009,** 106.
2. Prasad, P. N., *Nanophotonics*. Wiley Interscience: New York, 2004.
3. Kittel, C., *Introduction to Solid State Physics*. 8th ed.; John Wiley & Sons, Inc: 2005.
4. Brus, L. E. *J. Chem. Phys.* **1984,** 80, 4403-4409.
5. Wise, F. W. *Accounts Chem. Res.* **2000,** 33, 773-780.
6. Murray, C. B.; Kagan, C. R.; Bawendi, M. G. *Annu. Rev. Mater. Sci.* **2000,** 30, 545-610.
7. Medintz, I. L.; Uyeda, H. T.; Goldman, E. R.; Mattoussi, H. *Nat. Mater.* **2005,** 4, 435-446.
8. Kongkanand, A.; Tvrdy, K.; Takechi, K.; Kuno, M.; Kamat, P. V. *J. Am. Chem. Soc.* **2008,** 130, 4007-4015.
9. Nozik, A. J.; Beard, M. C.; Luther, J. M.; Law, M.; Ellingson, R. J.; Johnson, J. C. *Chem. Rev.* 110, 6873-6890.
10. Steigerwald, M. L.; Alivisatos, A. P.; Gibson, J. M.; Harris, T. D.; Kortan, R.; Muller, A. J.; Thayer, A. M.; Duncan, T. M.; Douglass, D. C.; Brus, L. E. *J. Am. Chem. Soc.* **1988,** 110, 3046-3050.
11. Steigerwald, M. L.; Sprinkle, C. R. *J. Am. Chem. Soc.* **1987,** 109, 7200-7201.
12. Kortan, A. R.; Hull, R.; Opila, R. L.; Bawendi, M. G.; Steigerwald, M. L.; Carroll, P. J.; Brus, L. E. *J. Am. Chem. Soc.* **1990,** 112, 1327-1332.
13. Avitabile, G. C., Ugo; Maglio, Giovanni; Merlino, Antonello; and Picone, Delia, Micelles. In *What Is Chemistry*.
14. Yu, K.; Zaman, B.; Ripmeester, J. A. *J. Nanosci. Nanotechnol.* **2005,** 5, 669-681.
15. Dagtepe, P.; Chikan, V.; Jasinski, J.; Leppert, V. J. *Journal of Physical Chemistry C* **2007,** 111, 14977-14983.
16. Hines, M. A.; Guyot-Sionnest, P. *J Phys. Chem.* **1996,** 100, 468-471.
17. Dabbousi, B. O.; RodriguezViejo, J.; Mikulec, F. V.; Heine, J. R.; Mattoussi, H.; Ober, R.; Jensen, K. F.; Bawendi, M. G. *J. Phys. Chem. B* **1997,** 101, 9463-9475.
18. Murray, C. B.; Norris, D. J.; Bawendi, M. G. *J. Am. Chem. Soc.* **1993,** 115, 8706-8715.
19. Peng, X. G.; Schlamp, M. C.; Kadavanich, A. V.; Alivisatos, A. P. *J. Am. Chem. Soc.* **1997,** 119, 7019-7029.
20. Talapin, D. V.; Rogach, A. L.; Kornowski, A.; Haase, M.; Weller, H. *Nano Lett.* **2001,** 1, 207-211.
21. Park, J.; Joo, J.; Kwon, S. G.; Jang, Y.; Hyeon, T. *Angew. Chem.-Int. Edit.* **2007,** 46, 4630-4660.
22. Peng, Z. A.; Peng, X. G. *J. Am. Chem. Soc.* **2002,** 124, 3343-3353.
23. Peng, X. G.; Manna, L.; Yang, W. D.; Wickham, J.; Scher, E.; Kadavanich, A.; Alivisatos, A. P. *Nature* **2000,** 404, 59-61.
24. Foos, E. E.; Wilkinson, J.; Makinen, A. J.; Watkins, N. J.; Kafafi, Z. H.; Long, J. P. *Chem. Mater.* **2006,** 18, 2886-2894.
25. Bullen, C. R.; Mulvaney, P. *Nano Lett.* **2004,** 4, 2303-2307.

26. Jasieniak, J.; Bullen, C.; van Embden, J.; Mulvaney, P. *J. Phys. Chem. B* **2005,** 109, 20665-20668.
27. Yang, Y. A.; Wu, H. M.; Williams, K. R.; Cao, Y. C. *Angew. Chem.-Int. Edit.* **2005,** 44, 6712-6715.
28. Cumberland, S. L.; Hanif, K. M.; Javier, A.; Khitrov, G. A.; Strouse, G. F.; Woessner, S. M.; Yun, C. S. *Chem. Mater.* **2002,** 14, 1576-1584.
29. Dance, I. G.; Choy, A.; Scudder, M. L. *J. Am. Chem. Soc.* **1984,** 106, 6285-6295.
30. Talapin, D. V.; Rogach, A. L.; Haase, M.; Weller, H. *J. Phys. Chem. B* **2001,** 105, 12278-12285.
31. Talapin, D. V.; Rogach, A. L.; Shevchenko, E. V.; Kornowski, A.; Haase, M.; Weller, H. *J. Am. Chem. Soc.* **2002,** 124, 5782-5790.
32. Donega, C. D.; Liljeroth, P.; Vanmaekelbergh, D. *Small* **2005,** 1, 1152-1162.
33. van Embden, J.; Mulvaney, P. *Langmuir* **2005,** 21, 10226-10233.
34. Peng, X. G. *Adv. Mater.* **2003,** 15, 459-463.
35. Milliron, D. J.; Hughes, S. M.; Cui, Y.; Manna, L.; Li, J. B.; Wang, L. W.; Alivisatos, A. P. *Nature* **2004,** 430, 190-195.
36. Kudera, S.; Zanella, M.; Giannini, C.; Rizzo, A.; Li, Y. Q.; Gigli, G.; Cingolani, R.; Ciccarella, G.; Spahl, W.; Parak, W. J.; Manna, L. *Adv. Mater.* **2007,** 19, 548-+.
37. Manna, L.; Milliron, D. J.; Meisel, A.; Scher, E. C.; Alivisatos, A. P. *Nat. Mater.* **2003,** 2, 382-385.
38. Dagtepe, P.; Chikan, V.; Jasinski, J.; Leppert, V. J. *J Chem Phys C* **2007,** 111, 14977-14983.
39. Peng, Z. A.; Peng, X. G. *J. Am. Chem. Soc.* **2001,** 123, 1389-1395.
40. Soloviev, V. N.; Eichhofer, A.; Fenske, D.; Banin, U. *J. Am. Chem. Soc.* **2000,** 122, 2673-2674.
41. Klimov, V. I. *Annu. Rev. Phys. Chem.* **2007,** 58, 635-673.
42. Efros, A. L.; Rosen, M.; Kuno, M.; Nirmal, M.; Norris, D. J.; Bawendi, M. *Phys. Rev. B* **1996,** 54, 4843-4856.
43. Klimov, V. I.; McBranch, D. W. *Phys. Rev. Lett.* **1998,** 80, 4028-4031.
44. Klimov, V. I.; McBranch, D. W.; Leatherdale, C. A.; Bawendi, M. G. *Phys. Rev. B* **1999,** 60, 13740-13749.
45. Schaller, R. D.; Petruska, M. A.; Klimov, V. I. *Appl. Phys. Lett.* **2005,** 87.
46. Klimov, V. I.; Mikhailovsky, A. A.; McBranch, D. W.; Leatherdale, C. A.; Bawendi, M. G. *Phys. Rev. B* **2000,** 61, 13349-13352.
47. Klimov, V. I.; Mikhailovsky, A. A.; McBranch, D. W.; Leatherdale, C. A.; Bawendi, M. G. *Science* **2000,** 287, 1011-1013.
48. Farrow, B.; Kamat, P. V. *J. Am. Chem. Soc.* **2009,** 131, 11124-11131.
49. Kamat, P. V. *Journal of Physical Chemistry C* **2008,** 112, 18737-18753.
50. Robel, I.; Subramanian, V.; Kuno, M.; Kamat, P. V. *J. Am. Chem. Soc.* **2006,** 128, 2385-2393.
51. Tvrdy, K.; Frantsuzov, P. A.; Kamat, P. V. *Proc. Natl. Acad. Sci. U. S. A.* 108, 29-34.
52. Lomascolo, M.; Creti, A.; Leo, G.; Vasanelli, L.; Manna, L. *Appl. Phys. Lett.* **2003,** 82, 418-420.
53. Jiang, H.; Ju, H. X. *Anal. Chem.* **2007,** 79, 6690-6696.
54. Chan, W. C. W.; Nie, S. M. *Science* **1998,** 281, 2016-2018.

55. Parak, W. J.; Boudreau, R.; Le Gros, M.; Gerion, D.; Zanchet, D.; Micheel, C. M.; Williams, S. C.; Alivisatos, A. P.; Larabell, C. *Adv. Mater.* **2002,** 14, 882-885.
56. Zhang, T. R.; Ge, J. P.; Hu, Y. P.; Yin, Y. D. *Nano Lett.* **2007,** 7, 3203-3207.
57. Gerion, D.; Pinaud, F.; Williams, S. C.; Parak, W. J.; Zanchet, D.; Weiss, S.; Alivisatos, A. P. *J. Phys. Chem. B* **2001,** 105, 8861-8871.
58. McGuire, J. A.; Joo, J.; Pietryga, J. M.; Schaller, R. D.; Klimov, V. I. *Accounts Chem. Res.* **2008,** 41, 1810-1819.
59. Nozik, A. J. *Physica E* **2002,** 14, 115-120.
60. Schaller, R. D.; Sykora, M.; Jeong, S.; Klimov, V. I. *J. Phys. Chem. B* **2006,** 110, 25332-25338.
61. Nozik, A. J. *Nano Lett.* 10, 2735-2741.
62. Gratzel, M. *Nature* **2001,** 414, 338-344.
63. Gratzel, M. *Accounts Chem. Res.* **2009,** 42, 1788-1798.
64. Adler, R. B. S., A.C. and Longini, R.L., *Introduction to Semiconductor Physics*. John Wiley & Sons, Inc: New York, 1964; Vol. 1.
65. Queisser, H. J.; Haller, E. E. *Science* **1998,** 281, 945-950.
66. Stolk, P. A.; Gossmann, H. J.; Eaglesham, D. J.; Jacobson, D. C.; Rafferty, C. S.; Gilmer, G. H.; Jaraiz, M.; Poate, J. M.; Luftman, H. S.; Haynes, T. E. *J. Appl. Phys.* **1997,** 81, 6031-6050.
67. Hersam, M. M., Tobin, and Cortes, Norma, Rie Doping Scheme. In 2011.
68. Galli, G. *Nature* **2005,** 436, 32-33.
69. Knox, C. K.; Fillmore, S. D.; Call, D. M.; Allen, D. G.; Hess, B. C.; Davis, R. C.; Evenson, W. E.; Harrison, R. G. *J. Colloid Interf. Sci.* **2006,** 300, 591-596.
70. Tuinenga, C.; Jasinski, J.; Iwamoto, T.; Chikan, V. *ACS Nano* **2008,** 2, 1411-1421.
71. Roy, S.; Tuinenga, C.; Fungura, F.; Dagtepe, P.; Chikan, V.; Jasinski, J. *Journal of Physical Chemistry C* **2009,** 113, 13008-13015.
72. He, Z. B.; Jie, J. S.; Zhang, W. J.; Zhang, W. F.; Luo, L. B.; Fan, X.; Yuan, G. D.; Bello, I.; Lee, S. T. *Small* **2009,** 5, 345-350.
73. Bryan, J. D.; Schwartz, D. A.; Gamelin, D. R. *J. Nanosci. Nanotechnol.* **2005,** 5, 1472-1479.
74. Chadi, D. J. *Annu. Rev. Mater. Sci.* **1994,** 24, 45-62.
75. Erwin, S. C.; Zu, L. J.; Haftel, M. I.; Efros, A. L.; Kennedy, T. A.; Norris, D. J. *Nature* **2005,** 436, 91-94.
76. Du, M. H.; Erwin, S. C.; Efros, A. L. *Nano Lett.* **2008,** 8, 2878-2882.
77. Andersen, K. E.; Fong, C. Y.; Pickett, W. E. *Journal of Non-Crystalline Solids* **2002,** 299, 1105-1110.
78. Khanal, D. R.; Yim, J. W. L.; Walukiewicz, W.; Wu, J. *Nano Lett.* **2007,** 7, 1186-1190.
79. Radovanovic, P. V.; Gamelin, D. R. *J. Am. Chem. Soc.* **2001,** 123, 12207-12214.
80. Magana, D.; Perera, S. C.; Harter, A. G.; Dalal, N. S.; Strouse, G. F. *J. Am. Chem. Soc.* **2006,** 128, 2931-2939.
81. Dalpian, G. M.; Chelikowsky, J. R. *Phys. Rev. Lett.* **2006,** 96.
82. Chelikowsky, J. R. *Phase Transit.* **2006,** 79, 739-753.
83. Leitsmann, R.; Panse, C.; Kuwen, F.; Bechstedt, F. *Phys. Rev. B* **2009,** 80.
84. Lott, K.; Shinkarenko, S.; Volobujeva, O.; Turn, L.; Nirk, T.; Opik, A.; Nisumaa, R.; Kallavus, U.; Noges, M.; Mikli, V.; Viljus, M.; Gorokhova, E.; Anan'eva, G.; Grebennik, A.; Vishnjakov, A. *Phys. Status Solidi B-Basic Solid State Phys.* **2007,** 244, 1623-1626.

85. Pradhan N, G. D., Thessing J, Peng XG *J. Am. Chem. Soc.* **2005,** 127, 17586-17587.
86. Levy, M.; Lee, W. K.; Sarachik, M. P.; Geschwind, S. *Phys. Rev. B* **1992,** 45, 11685-11692.
87. Rouleau, C. M.; Lowndes, D. H. *Applied Surface Science* **1998,** 129, 418-424.
88. Perna, G.; Capozzi, V.; Minafra, A.; Pallara, M.; Ambrico, M. *European Physical Journal B* **2003,** 32, 339-344.
89. Lott, K.; Nirk, T.; Volobujeva, O.; Shinkarenko, S.; Turn, L.; Kallavus, U.; Grebennik, A.; Vishnjakov, A. *Physica B* **2006,** 376, 764-766.
90. Shim, M.; Guyot-Sionnest, P. *Nature* **2000,** 407, 981-983.
91. Yu, D.; Wang, C. J.; Guyot-Sionnest, P. *Science* **2003,** 300, 1277-1280.
92. Shim, M.; Wang, C. J.; Guyot-Sionnest, P. *J. Phys. Chem. B* **2001,** 105, 2369-2373.
93. Bawendi, M. G.; Carroll, P. J.; Wilson, W. L.; Brus, L. E. *J. Chem. Phys.* **1992,** 96, 946-954.
94. Norris, D. J.; Efros, A. L.; Erwin, S. C. *Science* **2008,** 319, 1776-1779.
95. Archer, P. I.; Santangelo, S. A.; Gamelin, D. R. *Nano Lett.* **2007,** 7, 1037-1043.
96. Hanif, K. M.; Meulenberg, R. W.; Strouse, G. F. *J. Am. Chem. Soc.* **2002,** 124, 11495-11502.
97. Chikan, V.; Kelley, D. F. *J. Phys. Chem. B* **2002,** 106, 3794-3804.
98. Leff, D. V.; Ohara, P. C.; Heath, J. R.; Gelbart, W. M. *J Phys. Chem.* **1995,** 99, 7036-7041.
99. Qu, L. H.; Peng, X. G. *J. Am. Chem. Soc.* **2002,** 124, 2049-2055.
100. Yu, W. W.; Qu, L. H.; Guo, W. Z.; Peng, X. G. *Chem. Mater.* **2003,** 15, 2854-2860.
101. Mikulec, F. V.; Kuno, M.; Bennati, M.; Hall, D. A.; Griffin, R. G.; Bawendi, M. G. *J. Am. Chem. Soc.* **2000,** 122, 2532-2540.
102. Trindade, T.; O'Brien, P.; Pickett, N. L. *Chem. Mat.* **2001,** 13, 3843-3858.
103. Veinot, J. G. C.; Ginzburg, M.; Pietro, W. J. *Chem. Mat.* **1997,** 9, 2117-2122.
104. Eychmuller, A.; Hasselbarth, A.; Katsikas, L.; Weller, H. *Berichte Der Bunsen-Gesellschaft-Physical Chemistry Chemical Physics* **1991,** 95, 79-84.
105. Pileni, M. P. *Langmuir* **1997,** 13, 3266-3276.
106. Michalet, X.; Pinaud, F.; Lacoste, T. D.; Dahan, M.; Bruchez, M. P.; Alivisatos, A. P.; Weiss, S. *Single Mol.* **2001,** 2, 261-276.
107. Turnbull, D. *J. Appl. Phys.* **1950,** 21, 1022-1028.
108. Mandal, P. K.; Chikan, V. *Nano Lett.* **2007,** 7, 2521-2528.
109. Dagtepe, P.; Chikan, V.; Jasinski, J.; Leppert, V. J. *The Journal of Physical Chemistry C* **2007,** 111, 14977-14983.
110. Tchebotareva, A. L.; de Dood, M. J. A.; Biteen, J. S.; Atwater, H. A.; Polman, A. *J. Lumines.* **2005,** 114, 137-144.
111. Vasilevskiy, M. I.; Rolo, A. G.; Artemyev, M. V.; Filonovich, S. A.; Gomes, M. J. M.; Rakovich, Y. P. *Phys. Status Solidi B-Basic Res.* **2001,** 224, 599-604.
112. Zhubing He, J. J. W. Z. W. Z. L. L. X. F. G. Y. I. B. S.-T. L. *Small* **2009,** 5, 345-350.
113. Gonzalez, A. M. P.; Arreola, I. V. *Rev. Mex. Fis.* **2009,** 55, 51-54.
114. Murphy, C. J. *J. Mater. Chem.* **2008,** 18, 2173-2176.
115. Hillhouse, H. W.; Beard, M. C. *Curr. Opin. Colloid Interface Sci.* **2009,** 14, 245-259.
116. Werlin, R.; Priester, J. H.; Mielke, R. E.; Kramer, S.; Jackson, S.; Stoimenov, P. K.; Stucky, G. D.; Cherr, G. N.; Orias, E.; Holden, P. A. *Nat. Nanotechnol.* **2011,** 6, 65-71.
117. Reiss, P.; Protiere, M.; Li, L. *Small* **2009,** 5, 154-168.

118. Norris, D. J.; Yao, N.; Charnock, F. T.; Kennedy, T. A. *Nano Lett.* **2001,** 1, 3-7.
119. Sorokina, I. T. *Opt. Mater.* **2004,** 26, 395-412.
120. Ladizhansky, V.; Lyahovitskaya, V.; Vega, S. *Phys. Rev. B* **1999,** 60, 8097-8104.
121. Meulenberg, R. W.; van Buuren, T.; Hanif, K. M.; Willey, T. M.; Strouse, G. F.; Terminello, L. J. *Nano Lett.* **2004,** 4, 2277-2285.
122. Javier, A.; Magana, D.; Jennings, T.; Strouse, G. F. *Appl. Phys. Lett.* **2003,** 83, 1423-1425.
123. Peng, Z. A.; Peng, X. G. *J. Am. Chem. Soc.* **2001,** 123, 183-184.
124. Kovalenko, M. V.; Scheele, M.; Talapin, D. V. *Science* **2009,** 324, 1417-1420.
125. Ginger, D. S.; Greenham, N. C. *J. Appl. Phys.* **2000,** 87, 1361-1368.
126. Manna, L.; Scher, E. C.; Alivisatos, A. P. *Journal of Cluster Science* **2002,** 13, 521-532.
127. Tuinenga, C. R., S. Moore, D. and Chikan, V. *Manuscript in Progress* **2011**.
128. Klimov, V. I. *J. Phys. Chem. B* **2000,** 104, 6112-6123.
129. Schrier, J.; Whaley, K. B. *Phys. Rev. B* **2003,** 67.
130. Mocatta, D.; Cohen, G.; Schattner, J.; Millo, O.; Rabani, E.; Banin, U. *Science* 332, 77-81.